Journal Pre-Proof

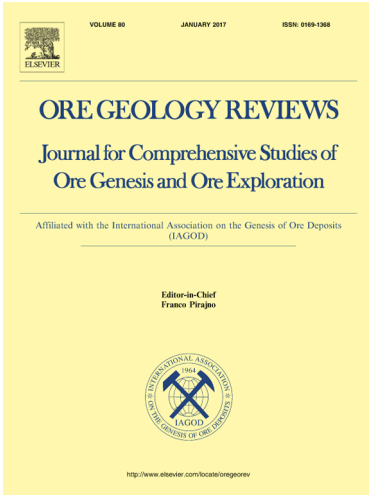

Fluid inclusion and stable isotope constraints on the heavy rare earth element mineralisation in the Browns Range Dome, Tanami Region, Western Australia

Teimoor Nazari-Dehkordi, Jan Marten Huizenga, Carl Spandler, Nicholas H.S. Oliver

PII: S0169-1368(18)31059-X
DOI: https://doi.org/10.1016/j.oregeorev.2019.103068
Reference: OREGEO 103068

To appear in: *Ore Geology Reviews*

Received Date: 23 December 2018
Revised Date: 13 May 2019
Accepted Date: 6 August 2019

Please cite this article as: T. Nazari-Dehkordi, J. Marten Huizenga, C. Spandler, N.H.S. Oliver, Fluid inclusion and stable isotope constraints on the heavy rare earth element mineralisation in the Browns Range Dome, Tanami Region, Western Australia, *Ore Geology Reviews* (2019), doi: https://doi.org/10.1016/j.oregeorev.2019.103068

Fluid inclusion and stable isotope constraints on the heavy rare earth element mineralisation in the Browns Range Dome, Tanami Region, Western Australia

Teimoor Nazari-Dehkordi[1], Jan Marten Huizenga[1,2], Carl Spandler[1*], Nicholas H.S. Oliver[1, 3]

[1]Economic Geology Research Centre, Department of Geoscience, James Cook University, Townsville, QLD 4811, Australia

[2]Department of Geology, University of Johannesburg, PO Box 524, Auckland Park 2006, South Africa

[3]HCOVGlobal Consultants, PO Box 3533, Hermit Park, QLD 4812, Australia

Abstract

This study reports on fluid inclusion and oxygen isotope compositions of mineralised and barren hydrothermal quartz veins and hosting metasedimentary rocks associated with the heavy rare earth element (HREE) mineralisation in the Browns Range Dome of the Tanami Region, Western Australia. The HREE mineralisation consists of quartz and xenotime-bearing hydrothermal veins and breccias that occurs along sub-vertical faults within Archean to Paleoproterozoic metasedimentary rocks. Based on analysis of nearly 550 quartz-hosted primary fluid inclusions, three fluid inclusion types were identified in the mineralised samples: type I low-salinity H_2O-NaCl (largely <5 wt.% NaCl; consistent with meteoric water), type II medium-salinity H_2O-NaCl (12-18 wt.% NaCl), and type III low- to high-salinity H_2O-$CaCl_2$-NaCl (1 to ca. 24 wt.% NaCl+$CaCl_2$). Homogenisation temperatures of all fluid inclusion types vary over a relatively wide range from 100 to 250 °C. Barren quartz veins contain only type I low-salinity H_2O-NaCl fluid inclusions, with homogenisation temperatures extending from 170 to 350 °C. Raman analyses of all three fluid inclusion types confirmed their aqueous nature with no carbon-bearing fluid species identified. The three fluid inclusion types indicate mixing of three hydrothermal fluids: a low-salinity H_2O-NaCl meteoric fluid (< 5 wt.% NaCl), a medium-salinity H_2O-NaCl (12-18 wt.% NaCl) fluid, and a high-salinity H_2O-$CaCl_2$-NaCl (ca. 24 wt.% NaCl+$CaCl_2$) fluid.

Limited LA-ICP-MS analysis found detectable Y, Ce, U and Cl only in the type III fluid inclusions, which indicates that transport of ore metals was (at least partly) by Cl complexes in the type III fluid. The $\delta^{18}O_{fluid}$ values calculated from quartz from mineralised samples are in the range defined by the Archean metasedimentary host rocks of the Browns Range Metamorphics ($\delta^{18}O_{fluid}$ = +1.8 to +5.2‰) and the unconformably-overlying Paleoproterozoic Birrindudu Group sandstones ($\delta^{18}O_{fluid}$ = +8‰). Collectively, our fluid inclusion and oxygen isotope data, together with other field, mineralogical and geochemical data, support an ore genesis model involving mixing of the three hydrothermal fluids in fault zones and along unconformity surfaces in, and around, the Browns Range Dome. The meteoric low-salinity H_2O-NaCl fluid potentially carried P from the Birrindudu Group sandstones, and the high-salinity H_2O-$CaCl_2$-NaCl fluid leached HREE+Y from metasedimentary rocks of the Browns Range Metamorphics. Ore deposition occurred following mixing of the P-bearing and HREE+Y-bearing fluids, and was associated with a widespread white mica alteration. The temperature and pressure during the fluid-fluid mixing and mineralisation was between 100 and 250 °C, and 0.4 and 1.6 kbar, respectively.

Keywords: Fluid inclusions; Oxygen isotopes; Hydrothermal; Xenotime; Unconformity

1. Introduction

The rare earth elements (REE) have been traditionally considered to be relatively immobile in hydrothermal fluids. However, recent studies have determined a hybrid magmatic-hydrothermal origin for a number of deposits that were originally regarded to be solely of magmatic origin (Salvi and Williams-Jones, 1996; Sheard et al., 2012; Liu and Hou, 2017; Liu et al., 2018). Experimental work has also demonstrated that solubilities of REE can be relatively high in certain hydrothermal environments, which raises the possibility of formation of REE deposits via purely hydrothermal processes (Migdisov et al., 2009; Williams-Jones et al., 2012; Loges et al., 2013; Migdisov and Williams-Jones, 2014; Timofeev et al., 2015, 2017). Nonetheless, the mechanisms whereby the REE - particularly the highly-sought after heavy (H)REE - are mobilised and precipitated by hydrothermal fluids, remain poorly understood. Available data on natural samples of REE-bearing hydrothermal fluids are restricted mostly to high temperature magmatic systems (e.g., Campbell et al., 1995; Williams-Jones et al., 2000), with only few recently-published studies on REE transport in low temperature environments (Richard et al., 2013; Rabiei et al., 2017;

Richter et al., 2018). A detailed understanding of hydrothermally-formed REE deposits can, therefore, enhance our knowledge of hydrothermal REE mobility and deposition.

Recently-discovered HREE mineralisation in north-western Australia defines a rather poorly understood hydrothermal vein and breccia ore system with ore metals contained predominantly in xenotime [(Y,HREE)PO_4] and minor florencite [LREE$Al_3(PO_4)_2(OH)_6$] (Cook et al., 2013; Nazari-Dehkordi et al., 2018, 2019). The orebodies are hosted by Archean metasedimentary rocks of the Browns Range Metamorphics (BRM) and the Paleoproterozoic Birrindudu Group sandstones of the Tanami Region, and also Red Rock Basin of the Halls Creek Orogen, in an area known as the "North Australian HREE+Y" (NAHREY) mineral field (Nazari-Dehkordi et al., 2019) (Fig. 1). The bulk of the mineralisation appears in close proximity to a regional unconformity between the BRM and overlying Birrindudu Group (Richter et al., 2018; Nazari-Dehkordi et al., 2018, 2019), so this mineralisation style has been labelled unconformity-related REE deposits (Nazari-Dehkordi et al., 2018). Of these deposits, Wolverine is the largest with a total mineral resource of 4.97 Mt at 0.86% total rare earth oxides. These deposits/prospects are unusually enriched in HREE and show no apparent link to magmatic sources (Nazari-Dehkordi et al., 2018), and therefore provide a unique opportunity to study aqueous transport and deposition of HREE.

Studies of fluid inclusion and oxygen isotope compositions place valuable constraints on hydrothermal fluids and associated mineralisation (e.g., Wilkinson, 2001). Here, we present a detailed fluid inclusion study incorporating fluid inclusion petrography, microthermometry, laser Raman spectroscopy analysis, and trace element microanalysis by laser ablation inductively coupled plasma mass spectrometry (LA-ICP-MS). We complement these data with oxygen isotope analysis of hydrothermally-formed xenotime and quartz from ore veins, as well as the metasedimentary host rocks, to allow inferences on the nature, composition and evolution of the ore-forming fluids.

2. Geological setting

All of the HREE deposits/prospects studied here occur near, or within, the Browns Range Dome of the Tanami Region (Fig. 1A), and in particular, near a regional unconformity that separates the underlying Archean metasedimentary rocks of the BRM from the overlying Birrindudu Group sandstones (Fig. 1B). Geological aspects of the Tanami Region are

published in detail elsewhere (e.g., Crispe et al., 2007; Bagas et al., 2008; Nazari-Dehkordi et al., 2017), so only a brief review of the Browns Range Dome is presented here.

Located in the northwest of the Tanami Region (Fig. 1C), the Browns Range Dome (BRD) is an east-west trending ovoid-shaped structure measuring ca. 60 km by ca. 30 km, cored by a 1-3 km thick ca. 1.87 Ga Browns Range Dome Granite (Page et al., 1995; Hendrickx et al., 2000; Cross and Crispe, 2007). Archean metasedimentary rocks of the BRM and minor mafic-ultramafic rocks occupy the western section of the Dome (Nazari-Dehkordi et al., 2017). The BRM comprises mainly meta-arkose locally containing interbedded medium- to coarse-grained conglomerates and semi-pelitic schists that experienced regional metamorphism, mostly of greenschist facies, but locally up to amphibolite grade. The BRM were derived from a Mesoarchean granitic source, and were deposited between ca. 3.1 Ga (age of the detrital zircons in the BRM) and ca. 2.5 Ga (emplacement timing of the cross-cutting granitic, syenitic and pegmatitic intrusions; Nazari-Dehkordi et al., 2017).

The BRM are unconformably overlain by a thick sequence of low-grade Paleoproterozoic sedimentary rocks with rare volcanic units (Fig. 1D), the characteristics of which are presented in detail by Bagas et al. (2008) and Crispe et al. (2007). These include the ca. 1.78 to ca. 1.64 Ga Pargee Sandstone and Birrindudu Group (Crispe et al., 2007; Vallini et al., 2007), and the Tanami and Ware Groups, both of which were intruded by ca. 1.8 Ga granites (Smith, 2001). The ca. 3.5 to 6 km thick Birrindudu Group consists of three conformable units including the basal Gardiner Sandstone, the fine-grained and calcareous Talbot Well Formation, and the Coomarie Sandstone (Blake et al., 1975). The Gardiner Sandstone is slightly metamorphosed and deformed, and unconformably overlies deeply weathered and metamorphosed rocks of the BRM, Tanami Group, Ware Group and Pargee Sandstone (Crispe and Vandenberg, 2005). The Gardiner Sandstone forms the outer margins of the BRD and dips gently (5 to 25º) to the west near the HREE mineralisation in the western part of the dome, and dips to the east in the eastern part of the dome (Fig. 1C).

3. HREE mineralisation

3.1. Mineralisation and ore geometry

Mineralisation throughout the NAHREY mineral field displays a spatial relationship with faults and some lithological boundaries (e.g., Wolverine; Fig. 1E). All of the mineralisation is strongly structurally-controlled and is characterised by a simple ore mineralogy of xenotime and subordinate florencite (Fig. 2). Other REE minerals, such as REE carbonates (e.g., bastnaesite) or monazite are absent, which is unusual for a REE ore deposit (e.g., Weng et al., 2015). The HREE mineralisation consists primarily of quartz-xenotime veins and breccias accommodated in sub-vertical faults, surrounded by a halo of low-grade ore extended into the host rock. This study focuses on two of the larger deposits, namely Wolverine and Area 5, from which fluid inclusion samples and the bulk of the oxygen isotope separates were collected. Detailed characteristics of the major HREE deposits/prospects within and around the BRD are provided in Nazari-Dehkordi et al. (2019), and hence only a brief summary is presented here.

The largest deposit, Wolverine, is a steeply (ca. 75° to the north) dipping planar orebody, up to 5 m wide, that extends over 400 m in strike length and from the surface to at least ca. 550 m in depth. The orebody lies within a WNW-striking fault in association with an intersecting W-E trending fault (Fig. 1E). Similarly, the Area 5 orebody occurs at an intersection of sub-vertical fault zones with prominent WNW and W strikes, alongside which the orebody appears as discontinuous pods. Area 5 is compositionally distinct, as it is dominated by florencite with only minor amounts of xenotime. Most other deposits/prospects hosted within the BRM, occur near, or on, the unconformity with the overlying Gardiner Sandstone, and are dominated by hydrothermal ore-bearing veins and breccias developed along steeply dipping W- to SW-striking structures, or along the unconformity surface itself (e.g., Cyclops, Dazzler and Iceman). Prospects hosted within the Gardiner Sandstone similarly show genetic association with major faults and unconformities. These include the Boulder Ridge prospect, 40 km south of the BRD (see Fig. 1B), which is characterised by quartz-xenotime veins near the unconformity with underlying sedimentary rocks of the Tanami Group.

3.2. Ore mineral paragenesis

There are three major mineral assemblages associated with the mineralisation and the metasedimentary host rocks across the NAHREY mineral field. A detailed ore mineral paragenesis is reported in Nazari-Dehkordi et al. (2019).

(1) A pre-ore detrital and metamorphic assemblage, including quartz (several generations), alkali feldspar, hematite and coarse-grained muscovite aligned in pre-mineralisation foliation. The pre-ore assemblage chiefly reflects a greenschist-facies metamorphic overprint on the predominantly arkosic host rocks, resulting in locally well-developed schistosity in the metasedimentary rocks, which potentially formed during the widespread ca. 1830 Ma Tanami Event (Crispe et al., 2007).

(2) A syn-ore hydrothermal mineral assemblage consisting predominantly of the ore minerals (xenotime, florencite), quartz and fine-grained muscovite (Fig. 3A). The syn-ore quartz-muscovite alteration consists dominantly of coarse- to fine-grained, cavity-filled and/or cemented, quartz and muscovite-sericite-illite assemblages, entirely enclosing the ore minerals. The main stage of the HREE mineralisation is characterised by fine-grained xenotime occurring in quartz + F-rich muscovite alteration assemblage within highly brecciated zones and coarse-grained quartz-xenotime veins (Figs. 3B-C).

(3) A post-ore mineral assemblage consisting mainly of multiple generations of quartz, hematite, barite and anhydrite within veins of up to 5 cm width, that cross-cut the early stages of the paragenetic sequence.

Previous U-Pb age dating of xenotime from a number of deposits/prospects from across the NAHREY mineral field has yielded mineralisation ages of between ca. 1.65 and ca. 1.60 Ga (Vallini et al., 2007; Morin-Ka et al., 2016; Nazari-Dehkordi et al., 2018, 2019). Therefore, the mineralisation across the NAHREY mineral field occurred within a relatively narrow 50 m.y. timeframe.

4. Sampling for fluid inclusion analysis

Localities of the samples for fluid inclusion analyses are listed in Table 1. The opaque nature and relatively fine grainsize of the REE-bearing ore minerals hindered direct study of the fluid inclusions trapped within these phases. Therefore, hydrothermal quartz that displays a paragenetic association with the mineralisation was targeted for analysis. The investigated samples include two mineralised hydrothermal vein quartz samples from drill cores of the Area 5 (sample A2-14, see Fig. 1C for sample locality) and Wolverine (sample W7-3, see Fig. 1C for sample locality) deposits (Figs. 4A-B) and one non-mineralised hydrothermal

vein quartz (sample W8; Fig. 4C) collected from an outcrop about 500 m east of the Wolverine orebody (see Fig. 1E). None of these samples were affected by post-depositional veining or fracturing. The barren quartz sample W8 shares a similar host structure and hydrothermal texture with the mineralised sample W7-3 from Wolverine. However, the precise timing of formation of the barren quartz vein is not known, leaving the possibility that this quartz could be syn-ore, or pre-/post-date the mineralisation. In either case, a comparison between the fluid inclusion assemblages present in the mineralised and barren samples can provide important constraints on the hydrothermal fluids involved in mineralisation.

Doubly-polished ca. 0.2 mm thick sections of the three samples were prepared. After initial microscopic evaluation of the sections, cathodoluminescence (CL) imaging of several quartz grains containing abundant and representative fluid inclusions was conducted. These CL images were used to identify internal textures, and potential multi-stage growth zones in quartz that are not evident from standard optical microscope petrography. Association of these CL zones with the ore minerals was used to infer ore-related quartz-hosted fluid inclusions. Initial fluid inclusion analysis involved thorough fluid inclusion petrography including documentation of the fluid inclusion shapes, spatial distribution, fluid composition types, and vapour/liquid ratios. Detailed grain-scale maps showing all fluid inclusions as a function of depth within the section were prepared for each quartz grain (see Appendix A).

5. Sampling for oxygen isotope analysis

Thirty-four samples, including four xenotime, 24 quartz and six bulk-rock powders, were selected for oxygen isotope analysis. These samples are divided into three groups based on association with the mineralisation and sample type:

(1) Ore-related samples (12 quartz and four xenotime) derived from ore-bearing veins and/or breccias of several HREE deposits/prospects (Wolverine, Boulder Ridge, Cyclops, Dazzler, and Iceman; see Fig. 1). Coexisting quartz and xenotime were sampled from four mineralised veins from Wolverine.

(2) Seven quartz samples collected from outcrops as a ca. 500 m sampling traverse along the prominent WNW striking fault structure that hosts the Wolverine orebody (Figs. 1E, 2A). The sub-vertical structure cuts the BRM and consists largely of a zone of breccias and vein

networks up to 5 metres wide with numerous splays and vein offshoots that extend into the BRM. The vein and breccia infill is predominantly coarse-grained hydrothermal quartz with occasional hematite. The Wolverine orebody lies at the western-most extent of the sampling traverse at the conjunction of the WNW and W-E faults. Here the brecciated ore samples are highly complex, containing high-grade ore, rounded to sub-rounded clasts of the BRM, and interrelated hydrothermal quartz in the matrix (Fig. 2B). Further to the east away from the ore zone, the breccias consist principally of large (30 cm wide) angular clasts of the BRM enclosed within hydrothermal quartz. These large clasts occasionally contain traces of ore minerals, particularly florencite. Examination of the hand specimens revealed multiple generations of hydrothermal quartz veins of variable width, which can be generally classified as transparent and milky-coloured (Fig. 2C). Microprobe examination identified minor occurrences of ore minerals only in the transparent quartz vein. The structure terminates to the east with a poorly exposed silicified zone composed largely of hydrothermal quartz veins without ore minerals. Based on the distribution of the ore minerals, the outcrops along the structure are variably mineralised, from the surface exposure of the Wolverine orebody through a weakly mineralised zone to a silicified zone entirely barren of the mineralisation. All of the outcrops are overprinted by the late quartz and hematite. We sampled along the structure, selected the hydrothermal quartz samples that showed no sign of fracturing or interruption by late veins, (Fig. 1E) to investigate possible lateral variations in oxygen isotope composition along the structure, with one sample collected from surface exposures of the Wolverine orebody and one sample with no traces of mineralisation collected from the silicified zone furthest from Wolverine. Five other samples represent slightly mineralised transparent quartz veins.

(3) Four detrital quartz and five bulk-rock samples from the BRM, and one bulk-rock sample from the Birrindudu Group sandstones lying above the unconformity with the BRM.

The samples were carefully washed in an ultrasonic bath to ensure complete removal of dust and associated contaminants, and then dried in an oven for 24 hours at 100 °C. Quartz and xenotime samples were subsequently lightly ground in a small mortar, and then a minimum of 50 mg of the target mineral was manually handpicked under a binocular microscope. Whole-rock samples were dried, crushed, split and then finely-milled using a ring mill. A minimum 20 mg of the milled powder was used for analysis.

6. Analytical Methods

6.1. Cathodoluminescence (CL) imaging

Cathodoluminescence images of the representative quartz grains from the fluid inclusion samples were obtained by a JEOL-JSM5410LV scanning electron microprobe equipped with a Robinson CL detector and photomultiplier at the Advanced Analytical Centre (AAC), James Cook University (JCU), Australia. Instrument operating conditions were set to 20 kV accelerating voltage, a 10 nA beam current and an acquisition time of 200 s. Samples were uncoated and the chamber was flushed with Ar.

6.2. Fluid inclusion microthermometry

Fluid inclusion microthermometry was carried out using a Linkam-MDS600 heating-freezing stage attached to an Olympus-BX51 microscope, located at the Department of Geoscience, JCU. The sample was located within an insulated stage on a 10 mm diameter quartz lens, housed in a stainless steel ring, all of which was placed on a thick silver block that serves as a thermal resister for sample heating. Caution was taken to avoid any contact between the sample and the steel ring to prevent uneven heating. The temperature within the stage was controlled through interaction between a heating element and gaseous nitrogen within the silver block. The temperature range of the instrument is –190 °C to +600 °C, and the precision and accuracy of the microthermometry measurements, based on standard calibration procedures, were estimated to be ±2 °C for homogenization temperatures and ±0.1 °C for final ice melting temperatures. The stage was calibrated using quartz-hosted synthetic CO_2-H_2O and H_2O fluid inclusions at the triple points of CO_2 (–56.6 °C) and H_2O (0.0 °C), and the critical point of H_2O (374 °C). Calibration samples were commercially obtained from FluidInc. The following phase transitions were measured systematically during heating:

(1a) Initial melting (H_2O-$CaCl_2$-NaCl): T_{mi} (antarcticite (aa) + hydrohalite (hh) + ice + vapour (vap) = liquid (liq) + hh + ice + vap).
(1b) Initial melting (H_2O-NaCl): T_{mi} (hydrohalite (hh) + ice + vapour (vap) = liquid (liq) + ice + vap).
(2) Final melting of ice: T_m (ice + liq + vap = liq + vap).

(3) Homogenisation by the disappearance of the vapour bubble into the liquid phase: T_h (liq + vap = liq).

Initial melting (T_{mi}) and final ice melting measurements (T_m) were carried out on all fluid inclusions examined. The temperature was decreased to –100 °C at a rate of ca. 20 °C/min to assure complete freezing. Freezing was usually marked by a sudden contraction of the vapour bubble that occasionally turned a brown-orange colour during cooling, which is typical for the H_2O-$CaCl_2$-NaCl system (Zwart and Touret, 1994). Initial melting temperatures (T_{mi}) measured in very small fluid inclusions (< 5 μm) and in fluid inclusions with a relatively low salinity are generally too high as a result of observation difficulties and the very small amount of hydrated salt present when frozen, respectively (e.g., Goldstein and Reynolds, 1994). Final melting of ice was measured with a heating rate of 0.2 °C/min. For homogenization experiments (T_h), the temperature was initially increased at a rate of 20 °C/min until the shrinking vapour bubble started to move rapidly. Thereafter, the heating rate was reduced to 0.5 °C/min to ensure accurate measurement of the homogenization temperature. Salinities and densities of the fluid inclusions were calculated using the Microsoft Excel-based program of Steele-MacInnis et al. (2012) developed for the H_2O-NaCl fluid system. For H_2O-$CaCl_2$-NaCl, the total salinity (wt.% NaCl and $CaCl_2$) was visually determined using the H_2O-$CaCl_2$-NaCl ternary phase diagram from Hurai et al. (2015).

6.3. Raman spectroscopy analysis

Raman analyses of vapour, solid and liquid compositions of individual fluid inclusions (n = 40), with size and liquid/vapour ratios representative of each fluid type, were conducted at the AAC, JCU using a WITec Alpha Access 300 instrument connected to a modified Zeiss microscope with a 100 times objective. The Raman was equipped with a diode-generated 532 nm green laser. The focus diameter of the laser beam was ca. 2 μm and the measurement time was 30 s with three accumulations. To correct for any influence from the matrix, analyses of the host mineral were performed under identical conditions and orientation. Data processing was done with WITec Project Data Analysis Software 4.1. The Raman database for different fluid species of Frezzotti et al. (2012) was used for fluid species identification.

6.4. Fluid inclusion element analysis

Elemental microanalysis of individual fluid inclusions was conducted at AAC, JCU, using a GeoLas 193-nm ArF Excimer laser ablation system coupled with a Bruker (formally Varian) 820-MS ICP-MS. Ablation was conducted in a custom-build large volume cell as described by Fricker et al. (2011) using high-purity He as the carrier gas, which was subsequently mixed with Ar prior to introduction into the ICP-MS. Analysis was carried out with a beam diameter of between 20 µm and 35 µm (depending on the inclusion size) and beam energy density on the sample of 10 J/cm^2. The following analytes were collected: ^{23}Na, ^{29}Si, ^{31}P, ^{35}Cl, ^{39}K, ^{44}Ca, ^{57}Fe, ^{89}Y, ^{140}Ce and ^{238}U. NIST-SRM-610 glass was used as the bracketing external standard, using the reference values of Spandler et al. (2011), and MPI-DING glass T1-G and GSD-1G glass were used as secondary check standards for all elements. Analysis of the secondary standards compare well with the published values (see Appendix B), demonstrating the accuracy of the analyses. Fluid inclusion element concentrations were quantified from raw signals using the software SILLS (Guillong et al., 2008), and involved deconvolution for fluid inclusion + host and host-only signals after calculation of background-corrected count rates for each isotope. Element concentrations in the H_2O-NaCl fluid inclusions were calculated using the NaCl concentration determined from the T_m (e.g., Heinrich et al., 2003; Pettke, 2008). For the highest salinity H_2O-$CaCl_2$-NaCl fluid inclusions, it was possible to determine the maximum NaCl concentration for the H_2O-$CaCl_2$-NaCl fluid inclusions. This maximum NaCl value was adopted as the internal standard to quantify element concentrations in these inclusions. This approach, however, was not possible for the low- and medium-salinity H_2O-$CaCl_2$-NaCl fluid inclusions, as proportions of Na^+ and Ca^{++} are not known; therefore, in these cases it was assumed that all the salt is NaCl for data reduction purposes. Owing to the small size, large salinity range, and analytical challenges of measuring quartz-hosted fluid inclusions by LA-ICP-MS (e.g., Audetat and Pettke, 2003), trace element concentrations carry relative uncertainties of at least 50%. Despite the large uncertainty in absolute concentration, the relative concentrations of elements in each analysis are much better constrained, so that elemental ratios can be compared with greater confidence.

6.5. Oxygen isotope analysis

Oxygen isotope analysis of quartz and xenotime was carried out at the Department of Geological Sciences, University of Cape Town, South Africa, using the laser fluorination

methods described in Harris and Vogeli (2010). The purified O_2, formed from each sample reaction with 10 kPa BrF_5, was collected onto a 5 Å molecular sieve contained in a stoppered glass storage bottle. Isotope ratios were measured using a Finnegan Mat Delta XP mass spectrometer in dual-inlet mode. All data are reported in the standard δ-notation relative to Standard Mean Ocean Water (SMOW), where δ (‰) = $((R_{sample}/R_{standard}) - 1) \times 1000$, with R being the measured ratio (e.g., $^{18}O/^{16}O$). Raw data were converted to the SMOW scale using the ratios obtained for duplicates of the internal standard MON GT ($\delta^{18}O$ = 5.38 ‰) run with each batch of 10 samples. The long-term average difference in $\delta^{18}O$ values of the two internal MONT-GT standards in each run is 0.11‰ (n = 216), corresponding to a 2σ uncertainty value of 0.15‰.

7. Results

7.1. Fluid inclusion petrography

An important aspect of fluid inclusion studies on hydrothermal ore deposits is interpreting the relationship between the fluid inclusions and the mineralisation event (e.g., Roedder and Bodnar, 1997). This requires a careful sample selection and detailed petrographic study in order to identify fluid inclusion assemblages of primary origin representing the ore-forming hydrothermal fluid (e.g., Goldstein, 2003).

A large number of primary and secondary fluid inclusions were identified in the studied quartz grains. These quartz grains derive from hydrothermal veins that are devoid of any other minerals (except xenotime and florencite in the mineralised samples), and show no evidence of later alteration. The quartz grains have oscillatory zonation in CL with variable luminescence intensity (Fig. 4D), which is commonly reported from hydrothermal quartz grains from a range of geological settings (e.g., Muller et al., 2010). The well-preserved oscillatory zonation also demonstrates the undeformed nature of the studied quartz samples (e.g., Muller et al., 2010; Fig. 4D). In some cases, a CL dark quartz generation occupying the interstices between these euhedral quartz grains was observed. Associated ore minerals are of variable size and are distributed randomly throughout the host quartz grains with no preferential association with any of the CL zones (Fig. 4). Therefore, the isolated fluid inclusions and irregularly distributed clusters of fluid inclusions hosted in intra-granular

quartz (Figs. 4E-F) are interpreted to be primary in origin and related directly to ore mineral formation. These primary inclusions are the focus of this study. Fluid inclusions in trans-granular trails were considered as secondary inclusions (e.g., Roedder, 1984), and were not further studied here. A summary of the characteristics of the fluid inclusion types present in each grain is listed in Appendix C; details of 542 fluid inclusions analysed in this study are available in Appendix D.

7.2. Fluid inclusion types in the mineralised samples

On the basis of fluid inclusion petrography, microthermometry and Raman analysis, three types of primary aqueous fluid inclusions were identified in the two mineralised samples (samples W7-3 and A2-14); (1) type I low-salinity H_2O-NaCl; (2) type II medium-salinity H_2O-NaCl, and; (3) type III low- to high-salinity H_2O-$CaCl_2$-NaCl. Raman spectroscopy analyses indicated that all inclusions are H_2O rich, with no detectable CO_2, CH_4, or any other C-bearing fluid species (Figs. 5A-D). The non-mineralised sample only comprises type I fluid inclusions. A summary of the main characteristics and compositional features of the different fluid inclusion types are provided in Table 2, and Figs. 6 and 7.

7.2.1. Type I low-salinity H_2O-NaCl fluid inclusions

The type I fluid inclusions consist primarily of H_2O-bearing liquid + vapour phases, and account for nearly 70% of the total fluid inclusion population. These fluid inclusions vary in size from 5 to 20 μm, and show variable liquid/vapour ratios, which allow further subdivision into inclusions with small (ca. 5 to ca. 10 vol.% of the inclusion) and large (ca. 50 vol.% of the inclusion) vapour phases. The fluid inclusions usually occur either in clusters, or locally as isolated inclusions and display negative-crystal, elliptical, and occasionally irregular morphologies (Figs. 4E-F). Only one of the type I fluid inclusions contained a tiny (ca. 1 μm) solid phase. Solid phases are comparatively more common in the type III fluid inclusions (n = 5), as will be discussed below. Additionally, about 20 mono-phase liquid H_2O-rich fluid inclusions were identified. These mono-phase fluid inclusions vary from 5 to 20 μm in size and have dominantly elliptical and minor irregular shapes, and share similar petrographic features with the two-phase fluid inclusions. However, these fluid inclusions were not used for microthermometry as melting temperatures measured in absence of a vapour phase cannot be used (e.g., Goldstein and Reynolds, 1994).

Initial melting temperatures (T_{mi}) of around −20 °C were observed in relatively large type I fluid inclusions (Fig. 8A), whereas initial melting could only be observed at around −5 °C for small fluid inclusions with very low salinities. Final ice melting temperatures (Fig. 6) range between −0.1 °C to −7 °C, with most fluid inclusions melting at temperatures greater than −3 °C. These final ice melting temperatures correspond to salinities of less than 10 wt.% NaCl and for most of the type I fluid inclusions less than 5 wt.% NaCl. Type I low-salinity H_2O-NaCl fluid inclusions have variable homogenisation temperatures (T_h) of between 100 °C and 250 °C, largely clustering around 200 °C (Fig. 8).

7.2.2. Type II medium-salinity H_2O-NaCl fluid inclusions

The type II fluid inclusions (medium-salinity H_2O-NaCl) are composed of two phases (liquid + vapour), both of which consist largely of H_2O. These fluid inclusions are relatively rare, with only 10 fluid inclusions (i.e., less than 2% of the total fluid inclusion population) analysed in this study. The type II fluid inclusions vary in size from 5 to 20 μm, and contain a vapour phase that comprises 30-35% of the inclusion volume. These fluid inclusions occur individually as isolated inclusions, and have negative-crystal and elliptical shapes. They are petrographically indistinguishable from the type I low-salinity H_2O-NaCl fluid inclusions (Figs. 4E-F). Nonetheless, distinction between the types I and II fluid inclusions can be made based on microthermometry measurements.

Initial melting and final ice melting for type II fluid inclusions vary within a relatively narrow range from ca. −20 °C to ca. −15 °C, and from −8 °C to ca. −15 °C (Figs. 6A-B, 8), respectively, and hence are characteristically lower than those of the type I fluid inclusions. These final ice melting temperatures correspond to a range of salinities from ca. 12 to ca. 18 wt.% NaCl, which are significantly greater than those of the type I fluid inclusions. The type II fluid inclusions are defined by a rather variable T_h range between 150 °C and 220 °C (Figs. 7A-B, 8B).

7.2.3. Type III low- to high-salinity H_2O-$CaCl_2$-NaCl fluid inclusions

These liquid-vapour±solid (florencite) fluid inclusions account for about 15% of the total fluid inclusion population and are exclusively present within the mineralised samples (samples A2-14 and W7-3). The type III fluid inclusions vary in size from 10 to 30 μm and generally have negative-crystal or rounded shapes. As with the type I fluid inclusions, the volume of the vapour phase in these fluid inclusions varies between ca. 10 to ca. 40 vol.%. The fluid inclusions generally appear as two-phase (liquid + vapour) fluid inclusions. However, five fluid inclusions (with 10 and 20 vol.% vapour phase) also contained a tiny solid phase (occupying about 5 to 10 vol.%) with a significant Raman peak at a wavenumber of ca. 1090 cm^{-1} (Fig. 5E). The two-phase fluid inclusions randomly occur throughout the host quartz either in clusters or as isolated individual inclusions. The solid bearing fluid inclusions only occur as isolated inclusions.

The type III fluid inclusions characteristically display a brown-orange colour at freezing temperatures, which is typical for the H_2O-$CaCl_2$-NaCl system (Goldstein and Reynolds, 1994; Zwart and Touret, 1994). The fluid inclusions show a T_{mi} ranging from ca. –25 °C to ca. –52 °C. As expected (Goldstein and Reynolds, 1994), the T_{mi} shows a positive correlation with T_m (Fig. 8A), confirming that the relatively high T_{mi} is associated with a low salinity NaCl dominated aqueous fluid, i.e. only a very small amount of antarcticite is present when frozen. The type III fluid inclusions have a T_m ranging between –0.5 °C to –25 °C, corresponding to total salinity from ca. 1 up to 24 wt.% NaCl+$CaCl_2$ (determined using the H_2O-$CaCl_2$-NaCl phase diagram by Hurai et al., 2015; Fig. 9). Further division based on salinity can divide type III fluid inclusions into “low” (<5 wt.% NaCl+$CaCl_2$), “medium” (6-19 wt.% NaCl+$CaCl_2$) and “high” (>19 wt.% NaCl+$CaCl_2$) salinity fluid inclusions. It is impossible to determine the NaCl/(NaCl+$CaCl_2$) mass fraction owing to the difficulty associated with observing the melting of the second-to-last solid phase (e.g., hydrohalite) in the fluid inclusions. However, the maximum NaCl concentration could be determined for the high-salinity fluid inclusions (T_m = –25 °C, see Fig. 9), i.e. ca. 17 wt.% NaCl for the fluid inclusions with a total salinity of ca. 24 wt.% NaCl+$CaCl_2$. Type III fluid inclusions yielded T_h values varying between 100 °C and 250 °C, somewhat similar to those documented for the types I and II fluid inclusions occurring in the same mineralised samples.

7.3. Fluid inclusions in the non-mineralised sample

Petrographic examinations combined with the microthermometry and Raman analyses, identified a different assemblage of primary fluid inclusions in the sample barren of mineralisation (sample W8). Fluid inclusions in this sample are composed of only two phases (liquid + vapour) with no trace of any solid phase. Raman spectroscopy analyses indicated no traces of any other component other than H_2O and NaCl in these fluid inclusions. These inclusions are usually small, rarely exceeding 10 μm in size, and contain a vapour phase of ca. 25% of the inclusion volume. They typically have negative-crystal, elliptical, and rarely irregular shapes, and occur as both clusters and isolated inclusions in quartz (Fig. 4G). All of the primary fluid inclusions in this sample yielded microthermometry measurements rather comparable to those of the type I low-salinity H_2O-NaCl documented in the mineralised samples (Table 2; Figs. 6, 8 and 9). Initial and final melting temperatures of these inclusions vary from around –20 °C to –10 °C, and –0.1 °C to ca. –7 °C, respectively (Figs. 6C, 8A), which corresponds to a narrow range of relatively low salinity from 0.2 to 5 wt.% NaCl. The fluid inclusions in the non-mineralised sample are distinguished by their highly variable T_h temperatures between ca. 170 °C and ca. 350 °C (Fig. 7C).

7.4. Fluid inclusion elemental composition

The elemental composition of 15 fluid inclusions covering all of the inclusion types from the mineralised and barren samples are presented in Table 3. Detection limits by the LA-ICP-MS technique tend to be high due to the small size of most of the inclusions; therefore many elements were not measured above their detection limits. Nonetheless, the data demonstrate that the major cations in the fluid inclusions are Na and K, with Na/K ratio varying within a relatively narrow range from 4.1 to 6.7. Potassium and Na contents respectively range from ca. 0.15 wt.% and ca. 0.8 wt.% in the type I low-salinity fluid inclusions, to nearly 1.4 wt.% and 6.6 wt.% in the type III high-salinity fluid inclusions (Fig. 10). No other elements were above the detection limits in the types I and II fluid inclusions. Some of the type III fluid inclusions were found to contain appreciable levels of Cl (2.1 to 6.4 wt.%), Ca (0.6 to 1.4 wt.%), Fe (0.05 to 0.6 wt.%), U (0.2 to 120 ppm) and REE (Y+Ce = 0.8 to 1.7 ppm), with the highest REE (and U) content recorded from the most saline fluid inclusions.

7.5. Oxygen isotope results

Oxygen isotope data are presented in Table 4 and Figure 11. The $\delta^{18}O$ values of ore-related quartz from Wolverine and several other HREE deposits/prospects range from +11.3 to +20.2‰. Quartz samples collected from the outcrops of the structure that hosts the Wolverine orebody have variable $\delta^{18}O_{quartz}$ values ranging from +20.2‰ near to the orebody, to +10.3‰ for the non-mineralised quartz sample furthest from Wolverine (Fig. 1E).

The $\delta^{18}O$ values obtained for detrital quartz samples and bulk rock samples from the BRM (host rocks) display a limited variation in the range from +10.7 to +13.3‰, and +12.4 to +14.1‰, respectively. One sample of the Birrindudu Group sandstones returned a distinctively higher $\delta^{18}O$ value of +16.9‰ (Fig. 11).

The $\delta^{18}O$ values of four quartz-xenotime pairs from Wolverine show a relatively limited variation from +14.6 to +17.2‰ for quartz, and from +6.3 to +7.3‰ for xenotime, which corresponds to a difference in $\delta^{18}O$ between quartz and xenotime of +7.7 to +9.8‰.

8. Discussion

8.1. Characteristics of the ore-forming hydrothermal fluids

The microthermometry dataset (Fig. 8) yielded comparable results for the mineralised samples derived from Wolverine (sample W7-3) and Area 5 (sample A2-14) deposits, despite the fact that Wolverine is xenotime rich whereas the Area 5 deposit is dominated by florencite. We consider, therefore, that the microthermometry dataset presented here is generally representative of the hydrothermal fluids involved in the HREE ore formation across the Browns Range Dome.

All of the fluid types are H_2O dominant without carbon-bearing fluid species as confirmed by Raman spectroscopy, showing only evidence for H_2O in the liquid and vapour phases of various fluid inclusions. The mineralised samples have fluid inclusions characterised with variable T_{mi}, T_m and T_h, consistent with the occurrence of multiple distinct hydrothermal fluids of varying salinity, composition and temperature. In particular, T_{mi} values define two arrays of fluid inclusions, one of which is characterised by T_{mi} values greater than ca. –20 °C, and one of which has T_{mi} in the range of –25 °C to –52 °C (Fig. 8A).

The first array represents type I fluid inclusions, characterised by relatively high T_{mi} values that are consistent with having H_2O-NaCl compositions (eutectic melting at −21.1 °C) with a T_m higher than −7 °C (Fig. 8). Many of these inclusions have a T_m greater than −3 °C, indicating low salinities (<5 wt.% NaCl), referred to here as a low-salinity H_2O-NaCl fluid. Fluid inclusions representing this low-salinity H_2O-NaCl fluid are abundant in the mineralised samples and are the only fluid inclusion type identified in the non-mineralised sample. This fluid potentially records the circulation of meteoric water in the hydrothermal system, which is known to be of low salinity in nature and the most common type of fluid in most sedimentary basins (e.g., Seward and Barnes, 1997; Kharaka and Hanor, 2007).

Meteoric water alone is unlikely to explain the presence of the medium-salinity H_2O-NaCl type II fluid inclusions (12-18 wt.% NaCl) from the same array ($T_{mi} \geq -20$ °C, Fig. 8A) in the mineralised samples. Although relatively rare, these fluid inclusions provide evidence of a distinct medium-salinity H_2O-NaCl hydrothermal fluid. The relatively wide range of T_m, and hence salinity, observed in the type II fluid inclusions is due potentially to a variable mixing with meteoric water causing dilution and subsequently reduction in the salinity (e.g., Seward and Barnes, 1997).

The second array of fluid inclusions with T_{mi} values that are distinctively lower than −21.1 °C (Fig. 8A) is inconsistent with the H_2O-NaCl system. Such low T_{mi} values are commonly reported from H_2O-$CaCl_2$-NaCl (−52 °C), H_2O-$FeCl_2$-NaCl (−37 °C), and H_2O-$MgCl_2$-NaCl (−35 °C) systems (e.g., Crawford, 1981; Bodnar, 2003). Based on our elemental compositional dataset (Table 3), the large proportion of fluid inclusions with $T_{mi,} < -40$ °C and the brown-orange colour visible during freezing (Zwart and Touret, 1994), we favour the H_2O-$CaCl_2$-NaCl compositional system for all of the fluid inclusions that have T_{mi} lower than −25 °C, here classified as the type III low- to high-salinity H_2O-$CaCl_2$-NaCl fluid inclusions. Type III fluid inclusions show a variable T_m (Fig. 8) corresponding to a wide range of salinities from very saline (up to ca. 24 wt.% NaCl+$CaCl_2$) to very low (<5 wt.% NaCl+$CaCl_2$). The salinity conforms well to varying degrees of mixing between the end-member high salinity H_2O-$CaCl_2$-NaCl fluid and the low salinity H_2O-NaCl meteoric water, resulting in formation of the type III fluid inclusions that have a broad range of salinity.

Collectively, the microthermometry dataset was used to identify three distinct types of hydrothermal fluids including a low-salinity H_2O-NaCl fluid (meteoric water) which underwent various degrees of mixing with a medium-salinity H_2O-NaCl fluid, and a high-salinity H_2O-$CaCl_2$-NaCl fluid. The estimated composition of the three hydrothermal fluid types recognised in both the mineralised and barren samples can be expressed on the H_2O-$CaCl_2$-NaCl ternary diagram (Fig. 9). Accordingly, the low-salinity H_2O-NaCl fluid, represented by type I fluid inclusions, are located near the H_2O apex. The medium-salinity H_2O-NaCl fluid, represented by the type II fluid inclusions, and present only in the mineralised samples, sit on the H_2O-NaCl binary near the hydrohalite field. The medium-salinity Type II fluid inclusions are comparatively rare, including only 10 out of ca. 550 fluid inclusions analysed here, so this fluid is not considered to have had a significant role in HREE ore formation. The high-salinity H_2O-$CaCl_2$-NaCl fluid, represented by the type III fluid inclusions found only in the mineralised samples, fall within the ice stability field. Compositionally-defined hydrothermal fluid types are also supported by our limited elemental analysis of a number of representative fluid inclusions (Table 3). Principally, the H_2O-NaCl fluid inclusions (type I low-salinity and type II medium-salinity) have a fairly simple cation constitution, composed largely of Na and K. In contrast, the high salinity type III fluid inclusions contain, in addition to elevated Na and K, appreciable quantities of Cl (up to 6.4 wt.%) and also occasionally detectable Ca (up to 1.4 wt.%) and Fe (up to 0.6 wt.%).

Petrographic investigations identified tiny solid phases only in one type I and in several type III fluid inclusions within the mineralised samples. These solid phases have a distinct peak in the Raman spectra at wavenumbers of ca. 1090 cm^{-1} (Fig. 5E). This peak position is characteristics of carbonate minerals (see Frezzotti et al., 2012), although the fluid inclusions do not contain CO_2, as shown by the Raman analyses, and carbonate minerals are entirely absent from the ore assemblage (see Nazari-Dehkordi et al., 2019). Therefore, a carbonate composition for the solid phases is deemed unlikely. Instead, we attribute these phases to be florencite, as the major Raman peaks for florencite also occur between 1000 and 1100 cm^{-1} (Fig. 5F; Frost et al., 2013). The occurrence of florencite in only a few fluid inclusions indicates that it was accidently trapped as a solid phase during fluid inclusion formation and is, therefore, cogenetic with ore formation. This premise is consistent with their most common occurrence in the type III fluid inclusions.

8.2. Trapping conditions of the hydrothermal fluids

Microthermometry data can be used to constrain physical conditions during fluid entrapment (e.g., Dubessy et al., 2003; Boiron et al., 2010; Bons et al., 2014), although direct determination of the pressure-temperature conditions of the fluid entrapments from fluid inclusion data requires an independent estimate of either pressure or temperature. Widely used are geothermometers that employ temperature sensitive oxygen isotope exchange between coexisting minerals, such as quartz-monazite, quartz-magnetite, and quartz-apatite. Xenotime and quartz crystallized together in the studied mineralised samples, so their oxygen isotope compositions have the potential to provide an estimate for the trapping temperature, provided isotope fractionation factors are known. However, as discussed below, oxygen isotope fractionation factors for this mineral pair are unconstrained, so this approach could not be applied here. In the case of boiling, the homogenisation temperature would indicate the true trapping temperature (e.g., Bodnar et al., 1985; Wilkinson, 2001; Moncada et al., 2012). However, the fluid inclusion assemblages consist mainly of a mono-modal group of liquid-rich fluid inclusions without coexisting vapour-rich fluid inclusions. The observed variation in the liquid/vapour ratios (10-40 vol.%) is, in part, expected to be an artefact of estimating phase proportions from two dimensional views of inclusions. Indeed, the largest variations in liquid/vapour ratios is observed in the most irregular-shaped inclusions, where estimates of the volumes of phases of the inclusion are most uncertain (e.g., Fig. 4E). Nevertheless, the liquid/vapour ratio is directly related to the density of the fluid inclusion, and, therefore, trapping P-T conditions. These features are clearly inconsistent with boiling.

As an alternative, we investigated mineral assemblages associated with the HREE mineralisation and the metasedimentary rocks of the BRM that host the orebodies. A significant feature of the pre-ore mineral paragenesis is the occurrence of a coarse-grained muscovite aligned in the pre-mineralisation foliation (Fig. 3A) that has been dated (Ar-Ar) to ca. 1720 Ma (Nazari-Dehkordi et al., 2019). This significantly predates the timing of the HREE ore formation (ca. 1.65 to ca. 1.60 Ga, Vallini et al., 2007; Morin-Ka et al. 2016; Nazari-Dehkordi et al., 2018, 2019). Consequently, the pre-ore muscovite has remained a closed system for Ar through the hydrothermal activity associated with the HREE mineralisation. Harrison et al. (2009) experimentally calculated an Ar closure temperature of 420 °C for muscovite, so this temperature represents the maximum possible fluid trapping temperature. Furthermore, based on the ca. 3.5 to 6 km thick Birrindudu Group sandstones that unconformably overly the metasedimentary rocks of the BRM (host rocks) and using the

equations detailed in Bjørlykke et al. (2010), we calculated a lithostatic fluid pressure of 0.9 to 1.6 kbar, and a corresponding hydrostatic fluid pressure of 0.4 to 0.6 kbar, constraining the fluid pressure to between 0.4 to 1.6 kbar (Fig. 12).

The mineralised samples contain all three types of fluid inclusions, which collectively have a range of T_h values of between ca. 100 and ca. 250 °C (Figs. 7A-B). Such a wide variation in T_h values is not expected of an isothermal fluid mixing process (e.g., Lecuyer et al., 1999; Derome et al., 2003; Dubessy et al., 2003). Instead, the mineralised samples appear to record circulation of fluids of varying temperature, including probably two hot (ca. 250 °C) medium-salinity and high-salinity fluids (types II and III) and one cold low-salinity fluid (ca. 100 °C; type I), which subsequently mixed to form fluid inclusions with a wide range of T_h values. A geothermal gradient of ca. 35 °C/km, suggested by Lambert (1983) for Proterozoic continental crust, corresponds to a temperature range of between 120 °C (3.5 km-thick Birrindudu Group) and 210 °C (6 km-thick Birrindudu Group), which is entirely consistent with P-T constraints provided here (Fig. 12).

The trapping temperatures of the type I low-salinity H_2O-NaCl fluid inclusions in the barren sample (with higher T_h values), are between 350 °C (highest T_h value) and 170 °C (lowest T_h value). In regard to the trapping pressure, a hydrostatic pressure between 0.4 to 0.6 kbar is plausible for reasonable geothermal gradients, whereas the higher lithostatic pressures are inconsistent with the 420 °C temperature limit defined by the pre-ore muscovite (Fig. 12). We speculate that the barren sample may indeed post-date the ore formation, and so formed under lower pressure conditions likely following the partial removal (by erosion or tectonics) of the overlying Birrindudu Group sandstones. Indeed, the wide range of T_h values (170-350 °C) combined with very limited variation in T_m and hence salinity, are inconsistent with occurrence of multiple fluids with distinct temperatures in the barren sample, but may record circulation and gradual cooling of a hot fluid (ca. 350 °C) in relatively shallow and cold crustal environments which also resulted in formation of fluid inclusions with very low T_h.

8.3. Origin of the hydrothermal fluids

The formation of the HREE deposits/prospects of the NAHREY mineral field was associated with mixing of hydrothermal fluids that carried the required components for ore mineral (xenotime and florencite) formation (Nazari-Dehkordi et al., 2018). Considering the

extremely low solubility of REE-P complexes in hydrothermal systems (Williams-Jones et al., 2012; Migdisov et al., 2016; Zhou et al., 2016), REE+Y and P were most likely transported by different hydrothermal fluids from different sources.

The association of Ce, Y and U exclusively with the type III fluid inclusions illustrates that transport of the ore metals and U was by saline H_2O-$CaCl_2$-NaCl hydrothermal fluid. This interpretation is consistent with current understanding that hydrothermal transport of REE is greatly enhanced in Cl-bearing saline fluids (e.g., Williams-Jones et al., 2012; Shu and Liu, 2019; Zheng and Liu, 2019). The relatively low REE content of these fluids (only ppm to 10s of ppm total REE) means that relatively high fluid volumes would have been required to produce the volume of ore in Wolverine and other deposits/prospects. Such high fluid fluxes are consistent with the observed metasomatic mineral assemblages of the ore zones (Nazari-Dehkordi et al., 2018).

The geochemical and isotopic datasets of Nazari-Dehkordi et al. (2018) demonstrate that the ore metals for the Browns Range mineralisation were leached from the BRM, so it is likely that the type III fluids also have a deep basinal origin. Indeed, the high salinity type III fluid is similar in composition to saline brines found in many sedimentary basins across the globe (Hanor, 1994). The required salinity (up to ca. 24 wt.% NaCl+$CaCl_2$) for the type III fluid may have been supplied by as yet unrecognised evaporitic horizons within the BRM, or may come from known evaporite components of surrounding Proterozoic sedimentary sequences (Dunster and Ahmad, 2013), via descending or laterally-migrating basinal fluids.

The hydrothermal source of P for ore formation is not so clear. None of the measured fluid inclusions contained detectable P content, although P has a very high detection limit (ca. 1 wt.%) in these analyses, and it is expected that the P content of the fluid would have been relatively low at these conditions (<1000 ppm, based on extrapolation of the results of Antignano and Manning, 2008). As discussed above, the fluid inclusions in the mineralised samples record the mixing between hydrothermal fluids that carried required components for ore formation (REE and P) from different sources. Accordingly, the high-salinity H_2O-$CaCl_2$-NaCl fluid and potentially the medium-salinity H_2O-NaCl fluid represent relatively hot, REE-bearing fluids, whereas the low-salinity H_2O-NaCl fluid represents cold meteoric water originated from shallower levels of the Birrindudu Group. Therefore, although precise determination of the P-bearing fluid is not possible at present, we assume that P was most

likely transported by the low-salinity meteoric fluid. A rather comparable ore formation mechanism has also been proposed for the Maw Zone prospect, Athabasca Basin, Canada, where hydrothermal xenotime occurs within brecciated sandstones close to the Archean–Proterozoic unconformity (Rabiei et al., 2017).

To place further constraints on the possible origin of these ore-forming hydrothermal fluids, we also compared oxygen isotope composition of the ore-related quartz samples with that of the BRM (host rocks) and overlying Birrindudu Group sandstones. Using the quartz-fluid isotope fractionation factors of Clayton et al. (1972) and the oxygen isotope compositions of our samples (Table 4), and assuming a temperature of 250 °C for ore-bearing hydrothermal fluids (Fig. 12; see also Nazari-Dehkordi et al., 2018), we calculated that the hydrothermal fluids that leached the BRM (host rock) had $\delta^{18}O_{fluid}$ values ranging from +1.8 to +5.2‰ (Fig. 11). These values are distinctly lower than the calculated $\delta^{18}O_{fluid}$ of putative hydrothermal fluid derived from the Birrindudu Group sandstones (sample C1; $\delta^{18}O_{fluid}$ = +8‰), but partially overlap with the $\delta^{18}O_{fluid}$ value ($\delta^{18}O_{fluid}$ = +5‰) calculated for the barren sample (sample W8; assuming a T of 350 °C according to the microthermometry measurements). The $\delta^{18}O_{fluid}$ values derived from the ore-related quartz separates vary from +2.4‰ to +11.3‰, with the great majority overlapping with the $\delta^{18}O_{fluid}$ range defined by both the BRM and the Birrindudu Group sandstones (Fig. 11), further supporting the premise that mineralisation involved contributions from fluids derived from, and interacted with, both the BRM and the Birrindudu Group sandstones.

8.4. The role of fluid-fluid mixing in ore formation

The microthermometry measurements demonstrated that the non-mineralised quartz only contained a single fluid inclusion type (type I fluid inclusions) highlighting the significant role of fluid mixing in ore formation. Further support for fluid mixing is provided by the occurrence of florencite solid phases, identified in a limited number of types I and III fluid inclusions from only the mineralised samples.

Fluid-fluid mixing and boiling are considered to be important physical processes affecting ore deposition (e.g., Wilkinson, 2001; Zheng and Liu, 2019). As mentioned previously, we did not find any evidence for fluid boiling, which is contrary to the findings of Richter et al. (2018) who suggested that fluid boiling promoted ore formation at Wolverine. A boiling

mechanism is typically associated with a drop in fluid pressure (e.g., fluid pressure release as a result of dilatancy of faults within the BRM, or exposure of the ore-bearing fluids to near surface environments). However, field interpretations and age data on the mineralisation and the host rocks do not appear to support a low pressure environment for the ore formation. The BRM is overlain by a thick sedimentary sequence of the Birrindudu Group sandstones, with the mineralisation extending from within the BRM and the overlying Birrindudu Group sandstones (Fig. 1). These observations, combined with the timing of the ore deposition across the NAHREY mineral field (ca. 1.65-1.60 Ga; Vallini et al., 2007; Morin-Ka et al., 2016; Nazari-Dehkordi et al., 2018, 2019) that partially coincided with the formation of the Birrindudu Group sandstones (ca. 1.78-1.64 Ga, Crispe et al., 2007; Vallini et al., 2007), indicate that ore formation occurred under a thick sedimentary sequence of ca. 3.5 to 6 km (Blake et al., 1975). Collectively, our fluid inclusion dataset combined with the age dataset reported from the NAHREY mineral field and also field observations support fluid mixing (rather than boiling) as the main trigger for ore formation.

Fluid-fluid mixing usually causes a change in temperature, acidity and redox properties (e.g., Wilkinson, 2001). Experimental work has shown that REE form trivalent cations in both solid and aqueous states (Migdisov et al., 2016), so redox variations were unlikely to influence ore deposition. Mixing of hydrothermal fluids of contrasting temperature, as well as the association of the ore minerals with a widespread fine-grained muscovite crystallisation suggesting of an increase in pH, as described by Nazari-Dehkordi et al. (2018) (Fig. 3A), potentially contributed to the ore formation. Indeed, variable U concentrations (0.2-120 ppm), reported from the type III fluid inclusions, in absence of any traces of U-bearing solid phases, potentially record an effective fractionation of U as a result of a rising pH during fluid mixing (e.g., Richard et al., 2010, 2012). More significantly though, we regard the confluence of discrete P-bearing and REE-bearing fluids as the major driver of REE phosphate precipitation, due to the extremely low solubility of REE phosphate complexes in aqueous fluids (Williams-Jones et al., 2012; Migdisov et al., 2016; Zhou et al., 2016).

8.5. Comparison with fluids associated with unconformity-related U deposits

The mineralisation setting of the NAHREY mineral field shares similar features with that of the world-class Proterozoic unconformity-related U deposits of northern Australia (Pine Creek Orogen) and Canada (Athabasca Basin). A detailed comparison is outlined in Nazari-

Dehkordi et al. (2019). In brief, these similarities include an association with regional unconformities and major faults between Paleoproterozoic sedimentary sequences and underlying Archean basement, along with a structurally-controlled geometry, occurrence of an ore-related white mica alteration and partial mineralisation age overlap. The fluid inclusion results reported here now allow comparison of the fluids involved in the formation of these two ore styles.

Studies of fluid inclusions associated with the unconformity-related U orebodies reveal a non-isothermal mixing of acidic and oxidising NaCl- and $CaCl_2$-rich end-member fluids, with reported homogenisation temperatures between ca. 100-200 °C (Derome et al., 2005) and trapping pressures between 0.5-1.5 kbar (Richard et al., 2016 and references therein). These fluids also contain variable concentrations of REE and U (Richard et al., 2010, 2013). These observations are very similar to our results for NAHREY mineral field, and suggest a rather similar mineralising fluid system for both U and HREE ore styles. In particular, high-salinity Cl-rich fluids of basinal origin appear to be an essential component for effective transportation of ore metals, and fluid-fluid mixing near unconformity structures promotes ore deposition (e.g., Richard et al., 2010). Multiple features of the fluid regimes associated with the U and HREE orebodies, including the fluid chemistry, fluid-fluid mixing, and large fluid fluxes near regional unconformities, are also reported to be important for formation of sedimentary-hosted Mesozoic Pb-Zn-F-Ba deposits located in the vicinity of unconformities in western Europe (see Boiron et al., 2010 and references therein).

8.6. Oxygen isotope fractionation between quartz and xenotime

The oxygen isotope composition of coexisting minerals with well-known fractionation factors (e.g., quartz-monazite, Breecker and Sharp, 2007; quartz-tourmaline, Slack and Trumbull, 2011, quartz-garnet, Quinn et al., 2017) is particularly useful for geothermometry of metamorphic and hydrothermal systems. Although commonly reported from a variety of geological environment (e.g., sedimentary, diagenetic, magmatic, metamorphic), little effort has been made to calculate and employ the oxygen isotope composition of xenotime. Currently, the available data of quartz-xenotime oxygen isotope fractionations are limited only to the theoretical dataset reported by Zheng (1996).

Employing the data derived from this study, we examine oxygen isotope fractionation between coexisting xenotime and quartz as a potential geothermometer. Using the formulation of Zheng (1996), and assuming an ore formation temperature of 250 °C, as discussed above, the oxygen isotope fractionation factor ($\Delta_{(1000\ \ln\ \alpha)}$) between quartz and xenotime would be around –1 ‰. The oxygen isotope fractionation factor of Zheng (1996) is rather insensitive to temperature, being only $\Delta_{(1000\ \ln\ \alpha)}$ = –1.7 ‰, at a temperature of 100 °C. In contrast, the $\Delta_{(1000\ \ln\ \alpha)}$ values calculated based on the $\delta^{18}O$ values of xenotime (+6.3 to +7.3‰) and coexisting quartz (+14.6 to +17.2‰) separates, using the fractionation factor formula of $\alpha_{qtz\text{-}xnt} = 1000 \ln [(1000 + \delta^{18}O_{qtz}) / (1000 + \delta^{18}O_{xnt})]$, are between +7.7 and +9.8 ‰. These values are very different from those calculated using the isotope fractionation parameterisation of Zheng (1996) and indicate that the oxygen isotope fractionations factors of Zheng (1996) cannot be used to calculate reliable temperatures from natural quartz-xenotime pairs. Nevertheless, the relatively large values of $\alpha_{qtz\text{-}xnt}$ found here provide encouragement that oxygen isotope analysis of quartz-xenotime pairs may serve as an effective geothermometer, provided future experimental and empirical studies are conducted to establish the systematics of oxygen isotope exchange between xenotime and quartz over a range of temperatures.

9. Conclusions

The major findings of this study include:

(1) Fluid inclusion data from the NAHREY mineral field provide evidence for the presence of three hydrothermal fluids, including a low-salinity H_2O-NaCl (meteoric) fluid, a medium-salinity H_2O-NaCl fluid, and a low- to high-salinity H_2O-$CaCl_2$-NaCl fluid in the mineralised samples. The non-mineralised sample only contains fluid inclusions comprising a low-salinity meteoric H_2O-NaCl fluid.

(2) Fluid inclusion data provide clear evidence for fluid-fluid mixing; this is in particular reflected in the wide salinity range of type III H_2O-NaCl-$CaCl_2$ fluid inclusions (1-24 wt.% NaCl+$CaCl_2$).

(3) Ore metals were transported, at least partially, as Cl complexes by the high-salinity H_2O-$CaCl_2$-NaCl fluid.

(4) Mineralisation occurred following mixing of hydrothermal fluids of variable salinity and temperature including a colder meteoric H_2O-NaCl water and hotter high-salinity

H_2O-$CaCl_2$-NaCl fluids. The pressure-temperature conditions of fluid-fluid mixing and mineralisation are 0.4-1.6 kbar, and 100-250 °C, respectively.

(5) The $\delta^{18}O_{fluid}$ values of the ore-related quartz separates suggest contribution from the Archean metasedimentary rocks of the BRM (host rocks) and the unconformably-overlying Birrindudu Group sandstones.

Acknowledgments

This work was financially and logistically supported by Northern Minerals Ltd., and by an ARC Future Fellowship (FT 120100198) to CS. Special thanks to Robin Wilson from Northern Minerals Ltd., for helping with the fieldwork and sampling, and to Chris Harris from University of Cape Town for conducting the oxygen isotope analyses. We also thank Antonin Richard and an anonymous reviewer for their constructive comments.

Appendices

Appendix A: Grain scale map of the quartz grains analysed for fluid inclusion

Appendix B: Composition of the standards for LA-ICP-MS analysis of fluid inclusions

Appendix C: Microthermometry data of primary fluid inclusions in different quartz grains

Appendix D: Fluid inclusion microthermometry dataset

References

Antignano, A., Manning, C.E., 2008. Rutile solubility in H_2O, H_2O–SiO_2, and H_2O–$NaAlSi_3O_8$ fluids at 0.7–2.0 GPa and 700–1000 °C: implications for mobility of nominally insoluble elements. Chem. Geol. 255, 283–293.

Audetat, A., Pettke, T., 2003. The magmatic-hydrothermal evolution of two barren granites: A melt and fluid inclusion study of the Rito del Medio and Canada Pinabete plutons in northern New Mexico (USA). Geochim. Cosmochim. Acta 67, 97–121.

Bagas, L., Bierlein, F.P., English, L., Anderson, J., Maidment, D., Huston, D.L., 2008. An example of a Palaeoproteozoic back-arc basin: petrology and geochemistry of the ca.

1864 Ma Stubbins Formation as an aid towards an improved understanding of the Granites-Tanami Orogen, Western Australia. Precambrian Res. 166, 168–184.

Blake, D.H, Hodgson, I.M., Smith, P.A., 1975. Geology of the Birrindudu and Tanami 1:2500000 Sheet Areas, Northern Territory. Canberra ACT. Bureau of Mineral Resources, Australia, Report 174.

Bodnar, R.J., 2003. Introduction to fluid inclusions, in: Samson, I., Anderson, A., Marshall, D. (Eds.), Fluid Inclusions: Analysis and Interpretation. Mineral. Assoc. Canada, Short Course 32, p. 1–8.

Bodnar, R.J., Reynolds, T.J., Kuehn, C.A., 1985. Fluid inclusion systematics in epithermal systems, in: Berger, B.R., Bethke, P.M. (Eds.), Geology and Geochemistry of Epithermal Systems. Rev. Econ. Geol. 2, 73–98.

Boiron, M.C., Cathelineau, M., Richard, A., 2010. Fluid flows and metal deposition near basement/cover unconformity: lessons and analogies from Pb-Zn-F-Ba systems for the understanding of Proterozoic U deposits. Geofluids 10, 270–292.

Bjørlykke, K., Høeg, K., Mondol, N.H., 2010. Introduction to Geomechanics: Stress and Strain in Sedimentary Basins, in: Bjørlykke, K. (Ed.), Petroleum Geoscience: From Sedimentary Environments to Rock Physics. Springer, Berlin, Heidelberg. 507 pp.

Bons, P.D., Fusswinkel, T., Gomez-Rivas, E., Markl, G., Wagner, T., Walter, B., 2014. Fluid mixing from below in unconformity-related ore deposits. Geology 42, 1035–1038.

Breecker, D.O., Sharp, Z.D., 2007. A monazite oxygen isotope thermometer. Am. Mineral. 92, 1561–1572.

Campbell, A.R., Banks, D.A., Phillips, R.S., Yardley, B.W.D., 1995. Geochemistry of Th-U-REE mineralizing magmatic fluids, Captain Mountains, New Mexico. Econ. Geol. 90, 1271–1287.

Clayton, R.N., O'Neil, J.R., Mayeda, T.K., 1972. Oxygen isotope exchange between quartz and water. J. Geophys. Res. B77, 3057–3067.

Cook, N.J., Ciobanu, C.L., O'Rielly, D., Wilson, R., Das, K., Wade, B., 2013. Mineral chemistry of Rare Earth Element (REE) mineralization, Browns Ranges, Western Australia. Lithos 172-173, 192–213.

Crawford, M.L., 1981. Phase equilibria in aqueous fluid inclusions, in: Hollister, L.S., Crawford, M.L. (Eds.), Applications to Petrology. Mineral. Assoc. Canada 6, 75–100.

Crispe, A., Vandenberg, L., 2005. Geology of the Tanami Region, Northern Territory. Northern Territory Geol. Surv. Bull.

Crispe, A.J., Vandenberg, L.C., Scrimgeour, I., 2007. Geological framework of the Archaean and Palaeoproterozoic Tanami Region, Northern Territory. Miner. Depos. 42, 1–26.

Cross, A., Crispe, A., 2007. SHRIMP U-Pb analyses of detrital zircon: a window to understanding the Paleoproterozoic development of the Tanami Region, northern Australia. Miner. Depos. 42, 27–50.

Derome, D., Cathelineau, M., Cuney, M., Fabre, C., Lhomme, T., Banks, D.A., 2005. Mixing of sodic and calcic brines and uranium deposition at the McArthur River, Saskatchewan, Canada. A Raman and laser induced breakdown spectroscopic study of fluid inclusions. Econ. Geol. 100, 1529–1545.

Derome, D., Cuney, M., Cathelineau, C., Fabre, M., Dubessy, J., Bruneton, P., Hubert, A., 2003. A detailed fluid inclusion study in silicified breccias from the Kombolgie sandstones (Northern Territory, Australia): inferences for the genesis of middle-Proterozoic unconformity-type uranium deposits. J. Geochem. Explor. 80, 259–275.

Dubessy, J., Derome, D., Sausse, J., 2003. Numerical modelling of fluid mixings in the H_2O-NaCl system. Applications to the North Caramal uranium prospect (Australia). Chem. Geol. 194, 25–39.

Dunster, J.N., Ahmad, M., 2013. Birrindudu Basin, in: Ahmad, M., Munson, T.J., (Eds.), Geology and Mineral Resources of the Northern Territory. Northern Territory Geol. Surv. Bull. 5, 17:1–17:17.

Frezzotti, M.L., Tecce, F., Casagli, A., 2012. Raman spectroscopy for fluid inclusion analysis. J. Geochem. Explor. 112, 1–20.

Fricker, M.B., Kutscher, D., Aeschlimann, B., Frommer, J., Dietiker, R., Bettmer, J., Günther, D., 2011. High spatial resolution trace element analysis by LA-ICP-MS using a novel ablation cell for multiple or large samples. Int. J. Mass Spectrom. 307, 39–45.

Frost, R.L., Xi, Y., Scholz, R., Tazava, E., 2013. Spectroscopic characterization of the phosphate mineral florencite-La $–LaAl_3(PO_4)_2(OH, H_2O)_6$, a potential tool in the REE mineral prospection. J. Mol. Struct. 1037, 148–153.

Goldstein, R.H., 2003. Petrographic analysis of fluid inclusions studies, in: Samson, I., Anderson, A., Marshall, D. (Eds.), Fluid Inclusions: Analysis and Interpretation. Mineral. Assoc. Canada, Short Course 32, 9–53.

Goldstein, R.H., Reynolds, T.J., 1994. Systematics of fluid inclusions in diagenetic minerals. Society for Sedimentary Geology, Short Course 31, 1–199.

Guillong, M., Meier, D.L., Allan, M.M., Heinrich, C.A., Yardley, B.W.D., 2008. SILLS: A MATLAB-based program for the reduction of laser ablation ICP-MS data of homogeneous materials and inclusions, in: Sylvester, P., (Ed.), Laser Ablation ICP-MS in the Earth Sciences: Current Practices and Outstanding Issues. Mineral. Assoc. Canada, Short Course 40, 328–333.

Hanor, J.S., 1994. Origin of saline fluids in sedimentary basins, in: Parnell, J., (Ed.), Geofluids: Origin, migration and evolution of fluids in sedimentary basins. J. Geol. Soc. 78, 151–174.

Harris, C., Vogeli, J., 2010. Oxygen isotope composition of garnet in the Peninsula Granite, Cape Granite Suite, South Africa: constraints on melting and emplacement mechanisms. South Afr. J. Geol. 113, 401–412.

Harrison, T.M., Celerier, J., Aikman, A.B., Hermann, J., Heizler, M.T., 2009. Diffusion of ^{40}Ar in muscovite. Geochim. Cosmochim. Acta 73, 1039–1051.

Heinrich, C.A., Pettke, T., Halter, W.E., Aigner-Torres, M., Audétat, A., Günther, D., Hattendorf, B., Bleiner, D., Guillong, M., Horn, I., 2003. Quantitative multi-element analysis of minerals, fluid and melt inclusions by laser-ablation inductively-coupled-plasma mass-spectrometry. Geochim. Cosmochim. Acta 67, 3473–3497.

Hendrickx, M.A., Slater, K., Crispe, A.J., Dean, A.A., Vandenberg, L.C., Smith, J.B., 2000. Paleoproterozoic stratigraphy of the Tanami Region: regional correlations realisation preliminary results. Northern Territory Geol. Surv. 71 pp.

Hurai, V., Huraiová, M., Slobodník, M., Thomas, R., 2015. Geofluids: developments in microthermometry, spectroscopy, thermodynamics, and stable isotopes. Elsevier. 472 pp.

Kharaka, Y.K., Hanor, J.S., 2007. Deep fluids in the continents: I. Sedimentary basins, in: Drever, J.I., (Ed.), Surface and Ground Water, Weathering and Soils. Treatise on Geochemistry 5, 48 pp.

Lambert, R.S.J., 1983. Metamorphism and thermal gradients in the Proterozoic continental crust. Geol. Soc. Am. Memoir. 161, 155–166.

Lecuyer, C., Dubois, M., Marignac, C., Gruau, G., Fouquet, Y., Ramboz, C., 1999. Phase separation and fluid mixing in subseafloor back arc hydrothermal systems: A microthermometric and oxygen isotope study of fluid inclusions in barite-sulfide chimneys of the Lau basin. J. Geophys. Res. 104, B17911–B17927.

Liu, Y., Chakhmouradian, A.R., Hou, Z.Q., Song, W.L., Kynicky, J., 2018. Development of REE mineralization in the giant Maoniuping deposit (Sichuan, China): insights from

mineralogy, fluid inclusions, and trace element geochemistry. Miner. Depos. http://doi.org/10.1007/s00126-018-0836-y.

Liu Y., Hou Z.Q., 2017. A synthesis of mineralization styles with an integrated genetic model of carbonatite-syenite-hosted REE deposits in the Cenozoic Mianning-Dechang REE metallogenic belt, the eastern Tibetan Plateau, south western China. J. Asian Earth Sci. 137, 35–79.

Loges, A., Migdisov, A.A., Wagner, T., Williams-Jones, A.E., Markl, G., 2013. An experimental study of the aqueous solubility and speciation of Y(III) fluoride at temperatures up to 250 °C. Geochim. Cosmochim. Acta 123, 403–415.

Migdisov A.A., Williams-Jones A.E., Wagner T., 2009. An experimental study of the solubility and speciation of the Rare Earth Elements (III) in fluoride- and chloride-bearing aqueous solutions at temperatures up to 300 C. Geochim. Cosmochim. Acta 73, 7087–7109.

Migdisov, A., Williams-Jones, A.E., Brugger, J., Caporuscio, F., 2016. Hydrothermal transport, deposition, and fractionation of REE: experimental data and thermodynamic calculations. Chem. Geol. 439, 13–42.

Migdisov, A.A., Williams-Jones, A.E., 2014. Hydrothermal transport and deposition of the rare earth elements by fluorine-bearing aqueous liquids. Miner. Depos. 49, 987–997.

Moncada, D., Mutchler, S., Nieto, A., Reynolds, T.J., Rimstidt, J.D., Bodnar, R.J., 2012. Mineral textures and fluid inclusion petrography of the epithermal Ag-Au deposits at Guanajuato, Mexico: Application to exploration. J. Geochem. Explor. 114, 20–35.

Morin-Ka, S., Beardsmore, T.J., Hancock, E.A., Rasmussen, B., Dunkley, D., Muhling, J., Zi, J., Wilson, R., Champion, J., 2016. Alteration and Age of the Browns Range Rare Earth Element Deposits. Western Australian Department of Mines and Petroleum.

Muller, A., Herrington, R., Armstrong, R., Seltmann, R., Kirwin, D.J., Stenina, N.J., Kronz, A., 2010. Trace elements and cathodoluminescence of quartz in stockwork veins of Mongolian porphyry-style deposits. Miner. Depos. 45, 707–727.

Nazari-Dehkordi, T., Spandler C., Oliver N.H.S., Wilson R., 2019. Age, geological setting and paragenesis of heavy rare earth element mineralization of the Tanami Region, Western Australia. Miner. Depos. https://doi.org/10.1007/s00126-019-00878-4.

Nazari-Dehkordi, T., Spandler, C., Oliver, N.H.S., Wilson, R., 2018. Unconformity-Related Rare Earth Element deposits: A regional-scale hydrothermal mineralization type of northern Australia. Econ. Geol. 113, 1297–1305.

Nazari-Dehkordi, T., Spandler, C., Oliver, N.H.S., Chapman, J., Wilson, R., 2017. Provenance, tectonic setting and source of Archean metasedimentary rocks of the Browns Range Metamorphics, Tanami Region, Western Australia. Aust. J. Earth Sci. 64, 723–741.

Page, R., Sun, S.S., Blake, D., Edgecombe, D., Pearcey, D., 1995. Geochronology of an exposed late Archean basement terrane in the Granites-Tanami region. Aust. Geol. Surv. Org. Res. Newsletter 22, 21–22.

Pettke, T., 2008. Analytical protocols for element concentration and isotope ratio measurements in fluid inclusions by LA-(MC)-ICP-MS. Laser Ablation ICP-MS in the Earth Sciences: Current Practices and Outstanding Issues. Mineral. Assoc. Canada, Short Course, 40, 189–218.

Quinn, R.J., Kitajima, K., Nakashima, D., Spicuzza, M.J., Valley, J.W., 2017. Oxygen isotope thermometry using quartz inclusions in garnet. J. Metamorph. Geol. 35, 231–252.

Rabiei, M., Chi, G., Normand, C., Davis, D.J., Fayek, M., Blamey, N.F.J., 2017. Hydrothermal Rare Earth Element (Xenotime) Mineralization at Maw Zone, Athabasca Basin, Canada, and Its Relationship to Unconformity-Related Uranium Deposits. Econ. Geol. 112, 1483–1507.

Richard, A., Cauzid, J., Cathelineau, M., Boiron, M.C., Mercadier, J., Cuney, M., 2013. Synchrotron XRF and XANES investigation of uranium speciation and element distribution in fluid inclusions from unconformity- related uranium deposits. Geofluids 13, 101–111.

Richard, A., Cathelineau, M., Boiron, M.C., Mercadier, J., Banks, D.A., Cuney, M., 2016. Metal-rich fluid inclusions provide new insights into unconformity-related U deposits (Athabasca Basin and Basement, Canada). Miner. Depos. 51, 249–270.

Richard, A., Pettke, T., Cathelineau, M., Boiron, M.C., Mercadier, J., Cuney, M., Derome, D., 2010. Brine-rock interaction in the Athabasca basement (McArthur River U deposit, Canada): Consequences for fluid chemistry and uranium uptake. Terra Nova 22, 303–308.

Richard, A., Rozsypal, C., Mercadier, J., Banks, D.A., Cuney, M., Boiron, M.C., Cathelineau, M., 2012. Giant uranium deposits formed from exceptionally uranium-rich acidic brines. Nat. Geosci. 5, 142–46.

Richter, L., Diamond, L.W., Atanasova, P., Banks, D.A., Gutzmer, J., 2018. Hydrothermal formation of heavy rare earth element (HREE)-xenotime deposits at 100 °C in a sedimentary basin. Geology https://doi.org/10.1130/G39871.1.

Roedder, E., 1984. Fluid inclusions. Rev. Mineral. 12, 644 pp.

Roedder, E., Bodnar, R.J., 1997. Fluid inclusion studies of hydrothermal ore deposits, in: Barnes, H.L. (Ed.), Geochemistry of hydrothermal ore deposits. John Wiley & Sons, Inc. New York, p. 657–698.

Salvi, S., Williams-Jones, A.E., 1996. The role of hydrothermal processes in concentrating high-field strength elements in the Strange Lake peralkaline complex, northeastern Canada. Geochim. Cosmochim. Acta 60, 1917–1932.

Seward, T.M., Barnes, H.L., 1997. Metal transport by hydrothermal ore fluids, in: Barnes, H.L., (Ed.), Geochemistry of hydrothermal ore deposits. John Wiley and Sons, New York, p. 435–486.

Sheard, E.R., Williams-Jones, A.E., Heiligmann, M., Pederson, C., Trueman, D.L., 2012. Controls on the concentration of zirconium, niobium, and the rare earth elements in the Thor Lake Rare Metal Deposit, Northwest Territories, Canada. Econ. Geol. 107, 81–104.

Shu, X.C., Liu, Y., 2019. Fluid inclusion constraints on the hydrothermal evolution of the Dalucao Carbonatite-related REE deposit, Sichuan Province, China. Ore Geol. Rev. 107, 218–238.

Slack, J.F., Trumbull, R.B., 2011. Tourmaline as a recorder of ore-forming processes. Elements 7, 321–326.

Smith, J.B., 2001. Summary of results, joint NTGS-AGSO age determination program 1999-2001. Northern Territory Geol. Surv. 2001–007.

Spandler, C., Pettke, T., Rubatto, D., 2011. Internal and external fluid sources for eclogite-facies veins in the Monviso meta-ophiolite, Western Alps: Implications for fluid flow in subduction zones. J. Petrol. 52, 1207–1236.

Steele-MacInnis M., Lecumberri-Sanchez P., Bodnar R.J., 2012. HOKIEFLINCS_H_2ONACL: A Microsoft Excel spreadsheet for interpreting microthermometric data from fluid inclusions based on the PVTX properties of H_2O-NaCl. Comput. Geosci. 49, 334–337.

Timofeev, A., Migdisov, A.A., Williams-Jones, A.E., 2015. An experimental study of the solubility and speciation of niobium in fluoride-bearing aqueous solutions at elevated temperature. Geochim. Cosmochim. Acta 158, 103–111.

Timofeev, A., Migdisov, A.A., Williams-Jones, A.E., 2017. An experimental study of the solubility and speciation of tantalum in fluoride-bearing aqueous solutions at elevated temperature. Geochim. Cosmochim. Acta 197, 294–304.

Vallini, D.A., Groves, D.I., McNaughton, N.J., Fletcher, I.R., 2007. Uraniferous diagenetic xenotime in northern Australia and its relationship to unconformity-associated uranium mineralisation. Miner. Depos. 42, 51–64.

Weng, Z, Jowitt S.M., Mudd, G.M., Nawshad, H.A., 2015. A detailed assessment of global rare earth element resources: Opportunities and challenges. Econ. Geol. 110, 1925–1952.

Wilkinson, J.J., 2001. Fluid inclusions in hydrothermal ore deposits. Lithos 55, 229–272.

Williams-Jones, A.E., Migdisov, A.A., Samson, I.M., 2012. Hydrothermal mobilisation of the rare earth elements: A tale of "Ceria" and "Yttria". Elements 8, 355–360.

Williams-Jones, A.E., Samson, I.M., Olivo, G.R., 2000. The genesis of hydrothermal fluorite-REE deposits in the Gallinas Mountains, New Mexico. Econ. Geol. 95, 327–342.

Zheng, X., Liu, Y., 2019. Mechanisms of element precipitation in carbonatite-related rare-earth element deposits: evidence from fluid inclusions in the Maoniuping deposit, Sichuan Province, south western China. Ore Geol. Rev. 107, 218–238.

Zheng, Y.F., 1996. Oxygen isotope fractionations involving apatites: Application to paleotemperature determination. Chem. Geol. 127, 177–178.

Zhou, L., Mavrogenes, J., Spandler, C., Li, H., 2016. A synthetic fluid inclusion study of the solubility of monazite-(La) and xenotime-(Y) in H_2O-Na-K-Cl-F-CO_2 fluids at 800 °C and 0.5 GPa. Chem. Geol. 442, 121–129.

Zwart, E.W., Touret, L.R., 1994. Melting behaviour and composition of aqueous fluid inclusions in fluorite and calcite: applications within the system H_2O-$CaCl_2$-NaCl. Eur. J. Mineral. 6, 773–786.

Table captions

Table 1: Location details and fluid inclusion types within the studied samples from the Browns Range.

Table 2: Microthermometric data, salinity and density of the fluid inclusion types from the Browns Range.

Table 3: Elemental composition of the primary fluid inclusions.

Table 4: Oxygen isotope composition of quartz and xenotime separates and whole-rock samples of metasedimentary rocks.

Figure captions

Fig. 1: (A) Distribution of the HREE mineralisation in the NAHREY mineral field; (B) simplified geological map of the Tanami Region; (C) Simplified geological map of the Browns Range area; (D) Major rock units in the Tanami Region; (E) Sample locality and local geology along the structure that hosts the Wolverine orebody.

Fig. 2: Field photos from Wolverine; (A) Breccia outcrop along the structure; (B) Orebody outcrop; (C) Multiple generations of quartz (milky-coloured and ore-bearing transparent). Qtz = quartz; Xnt = xenotime.

Fig. 3: Mineral assemblage associated with the HREE mineralisation and metasedimentary rocks. (A) Pre-ore coarse-grained muscovite (CG Mus) and a syn-ore assembly of fine-grained muscovite (FG Mus) and xenotime (Xnt); (B) Hydrothermal quartz (Qtz) + xenotime vein with coarse-grained (1 mm) xenotime; (C) Dissemination of xenotime and atoll-like florencite (Flr) in a hydrothermal quartz vein.

Fig. 4: Photographs of the hydrothermal quartz samples selected for fluid inclusion studies. (A) Mineralised sample A2-14 from Area 5 deposit; (B) Mineralised sample W7-3 from Wolverine deposit; (C) Barren sample W8 from Wolverine deposit; (D) Cathodoluminescence image of a mineralised quartz vein showing oscillatory zoned quartz with ore minerals distributed throughout; (E) Assembly of primary fluid inclusions from sample W7-3; (F) Distribution of individual isolated fluid inclusions from sample A2-14; (G) Distribution of primary fluid inclusions from sample W8. Note that the fluid inclusions are at different depths. Qtz = quartz; Xnt = xenotime; Flr = florencite.

Fig. 5: Representative laser Raman spectra of fluid inclusions. (A) Spectrum for liquid phase of type I fluid inclusion (low-salinity H_2O-NaCl); (B) Spectrum for vapour phase of type I

fluid inclusion; (C) Spectrum for liquid phase of type III fluid inclusion (low- to high-salinity H_2O-$CaCl_2$-NaCl); (D) Spectrum for vapour phase of type III fluid inclusion; (E) Spectrum for solid (florencite) phase of type III fluid inclusion; (F) Spectrum for ore-related florencite. Note that the solid phase in the type III fluid inclusion and florencite ore have comparable vibrational regions.

Fig. 6: Histogram of the final ice melting temperatures (T_m) of the fluid inclusion types in the mineralised and barren samples.

Fig. 7: Histogram of the homogenization temperatures (T_h) of the fluid inclusion types in the mineralised and barren samples.

Fig. 8: (A) T_m-T_{mi} and (B) T_m-T_h relationships of the three fluid inclusion types in the mineralised and barren samples.

Fig. 9: Composition (in wt.%) of the three fluid inclusion types in the ternary H_2O-$CaCl_2$-NaCl diagram (after Hurai et al., 2015). Note that the NaCl/(NaCl+$CaCl_2$) mass fraction could not be determined for low- and medium-salinity type III fluid inclusions. The maximum NaCl/(NaCl+$CaCl_2$) mass fraction for the high salinity type III fluid inclusions can be determined from the intersection of the −25 °C ice-melting isotherm with the hydrohalite liquidus.

Fig. 10: Na versus K (in wt.%) plot for the three types of fluid inclusions.

Fig. 11: Oxygen isotope composition of the ore-related and barren quartz separates and the metasedimentary/sedimentary rocks of the BRM and the Birrindudu Group sandstones. Note that the ore-related quartz separates are characterised by $\delta^{18}O_{fluid}$ largely in the range defined by the BRM and the Birrindudu Group sandstones. The $\delta^{18}O_{fluid}$ bars include 2σ uncertainties. Qtz = quartz; BG = Birrindudu Group; BRM = Browns Range Metamorphics; WV = Wolverine.

Fig. 12: The estimated pressure-temperature conditions of entrapment of the three types of fluid inclusions. Note that the type I fluid inclusions in the barren quartz may have formed at lower pressures following the erosion of the Birrindudu Group sandstones.

Appendix A: Grain scale map of the quartz grains analysed for fluid inclusion

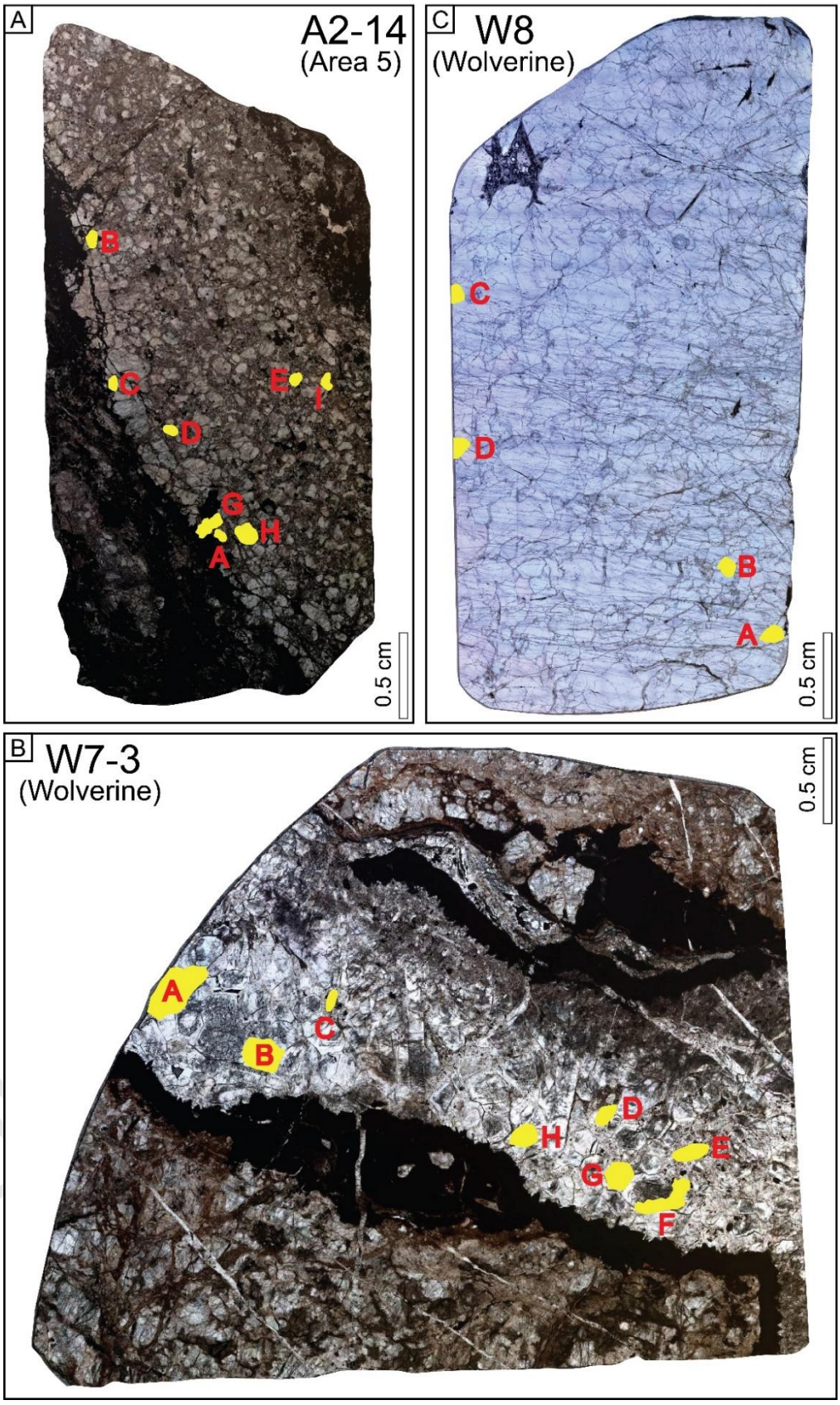

Fig. A1.1: Location of the quartz grains selected for fluid inclusion studies

*Note: Measured fluid inclusions from each grain are listed in Appendix D (FI No. column).

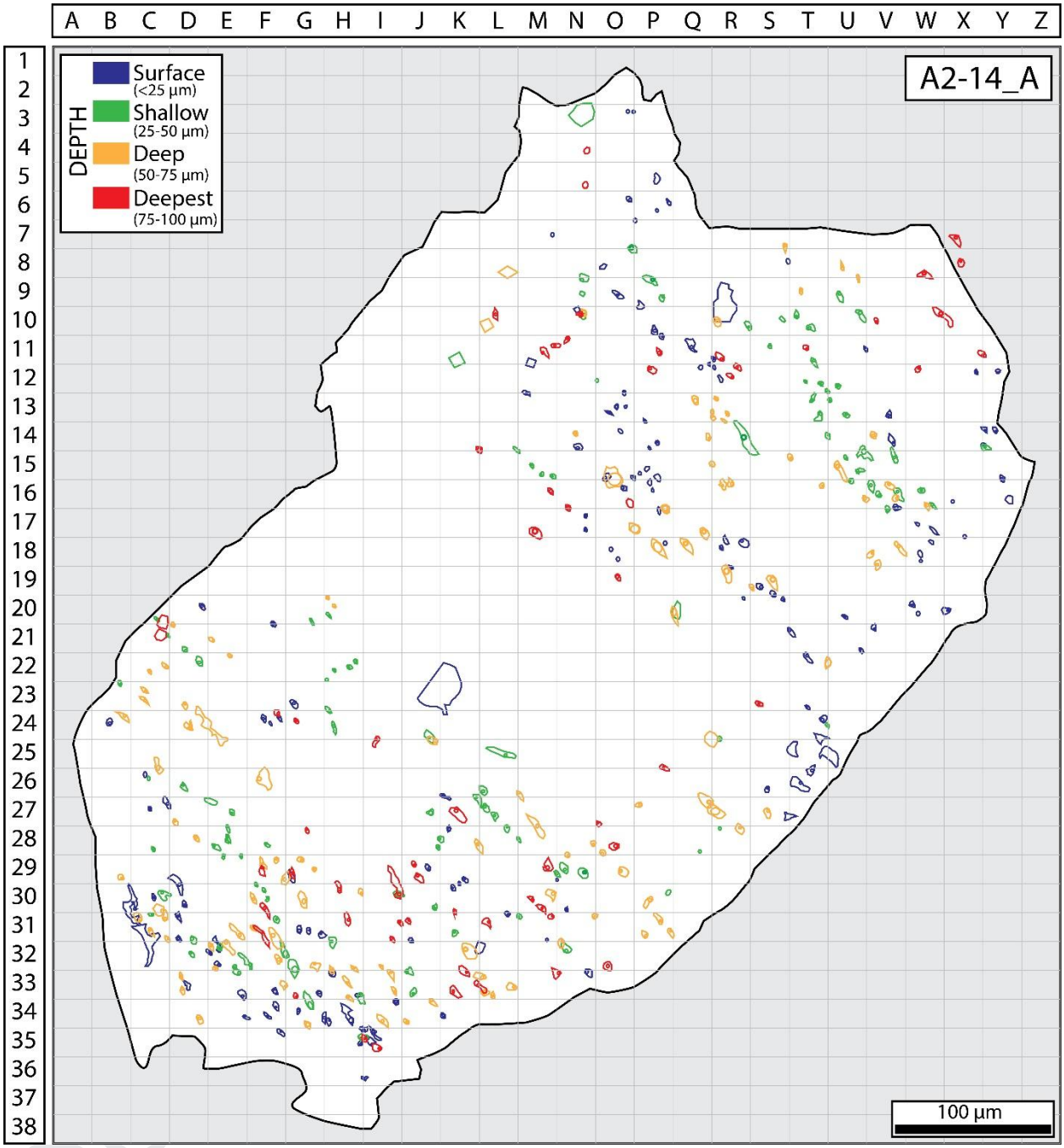

Fig. A1.2: Sample A2-14 (Area 5 Deposit, mineralised), Grain A

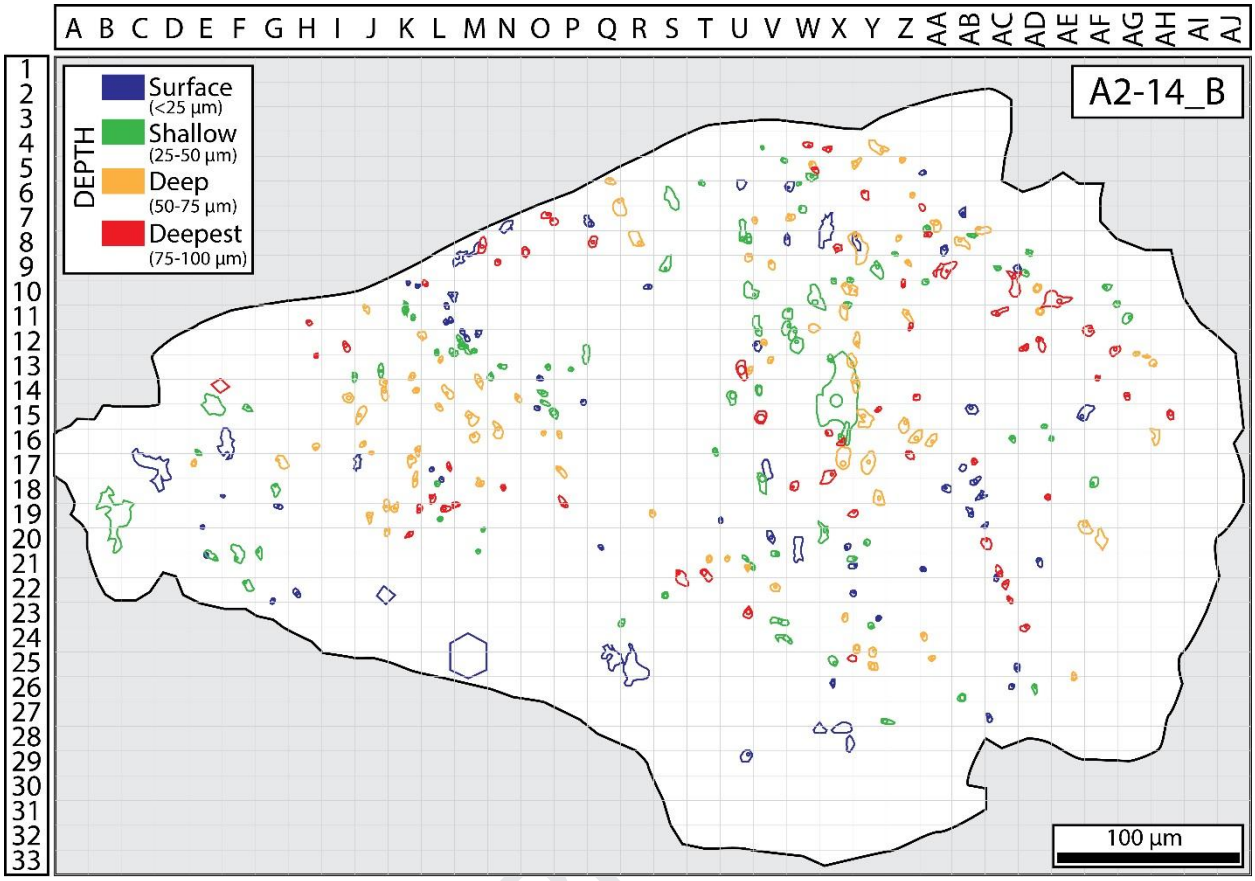

Fig. A1.3: Sample A2-14 (Area 5 Deposit, mineralised), Grain B

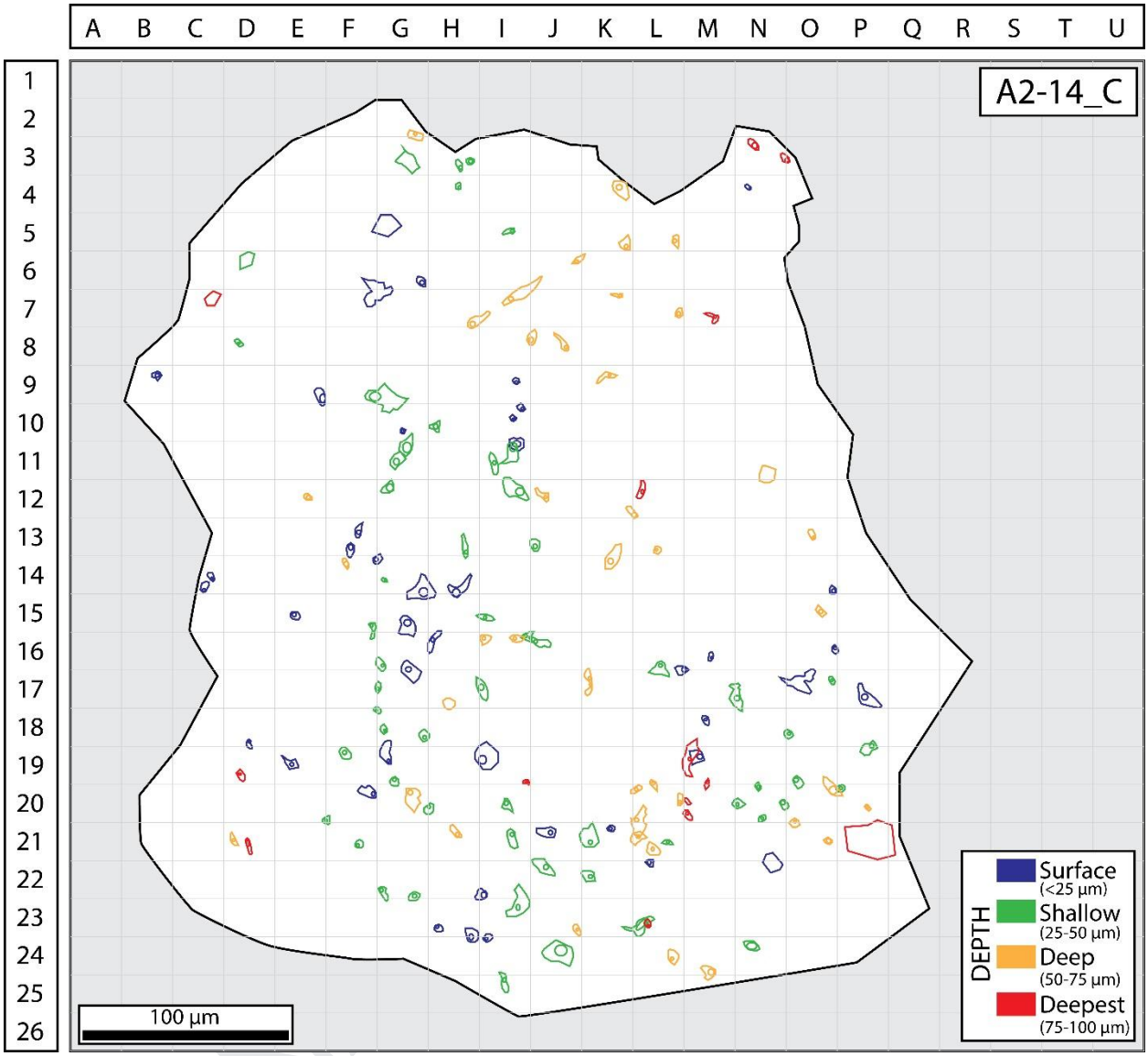

Fig. A1.4: Sample A2-14 (Area 5 Deposit, mineralised), Grain C

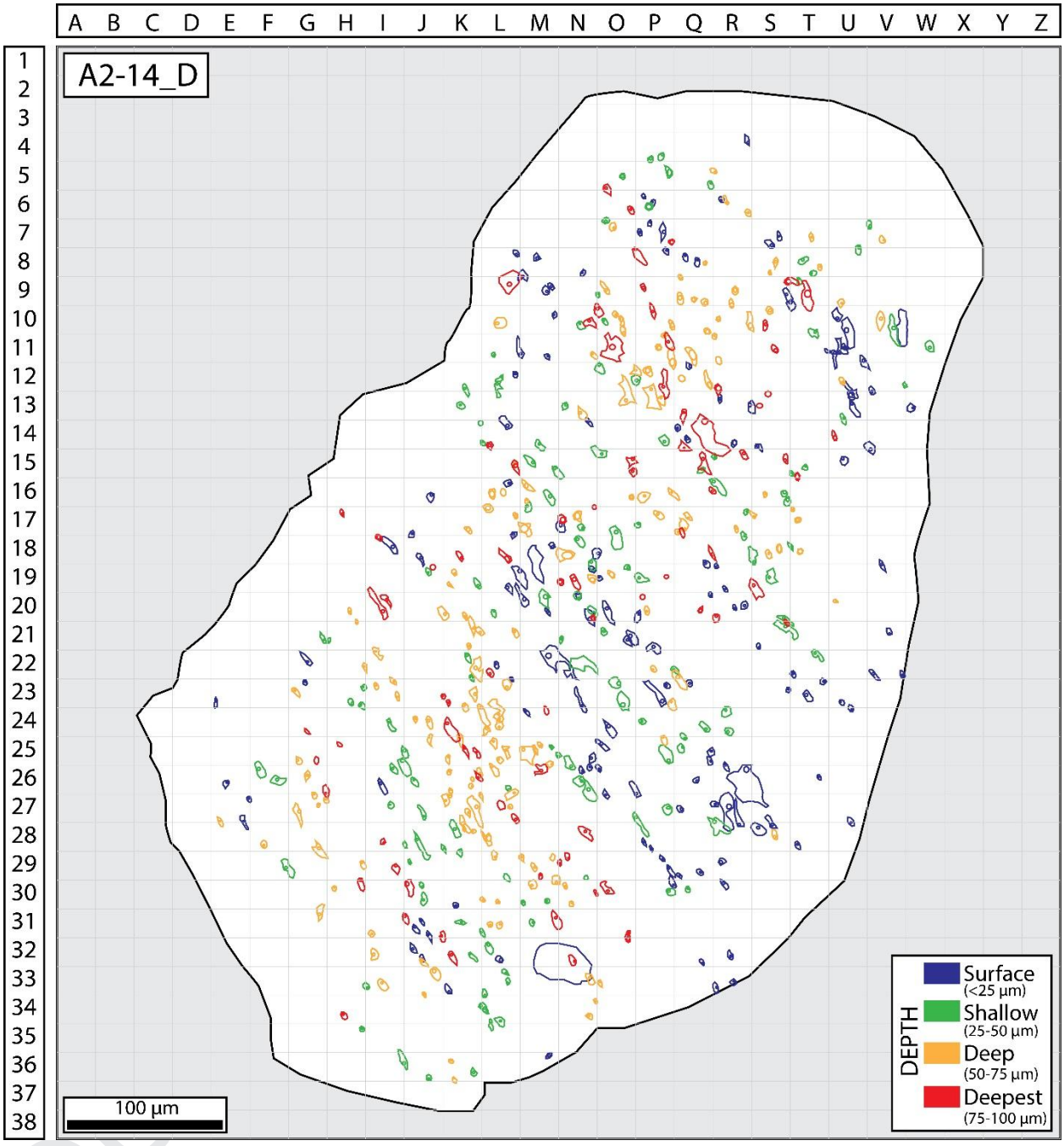

Fig. A1.5: Sample A2-14 (Area 5 Deposit, mineralised), Grain D

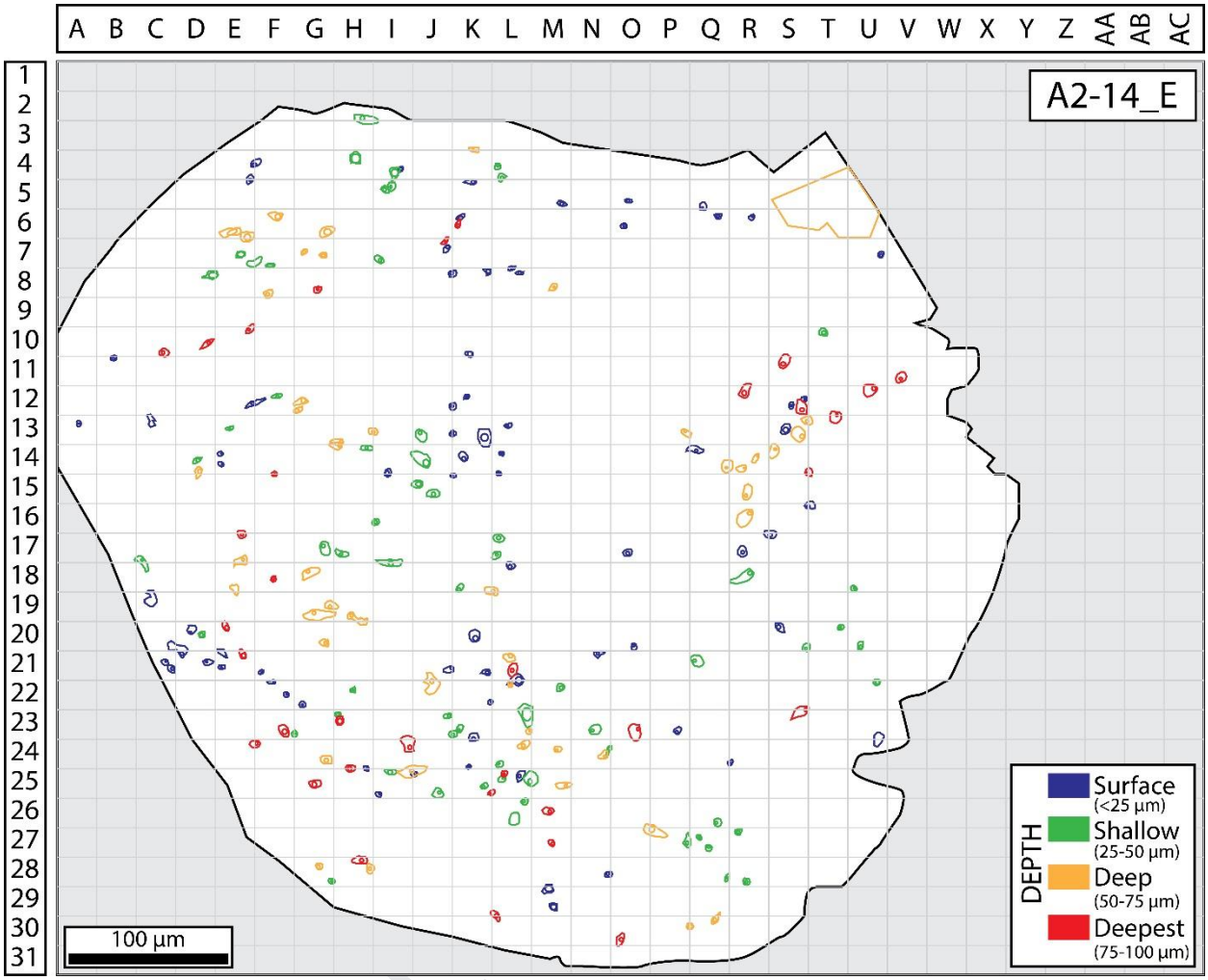

Fig. A1.6: Sample A2-14 (Area 5 Deposit, mineralised), Grain E

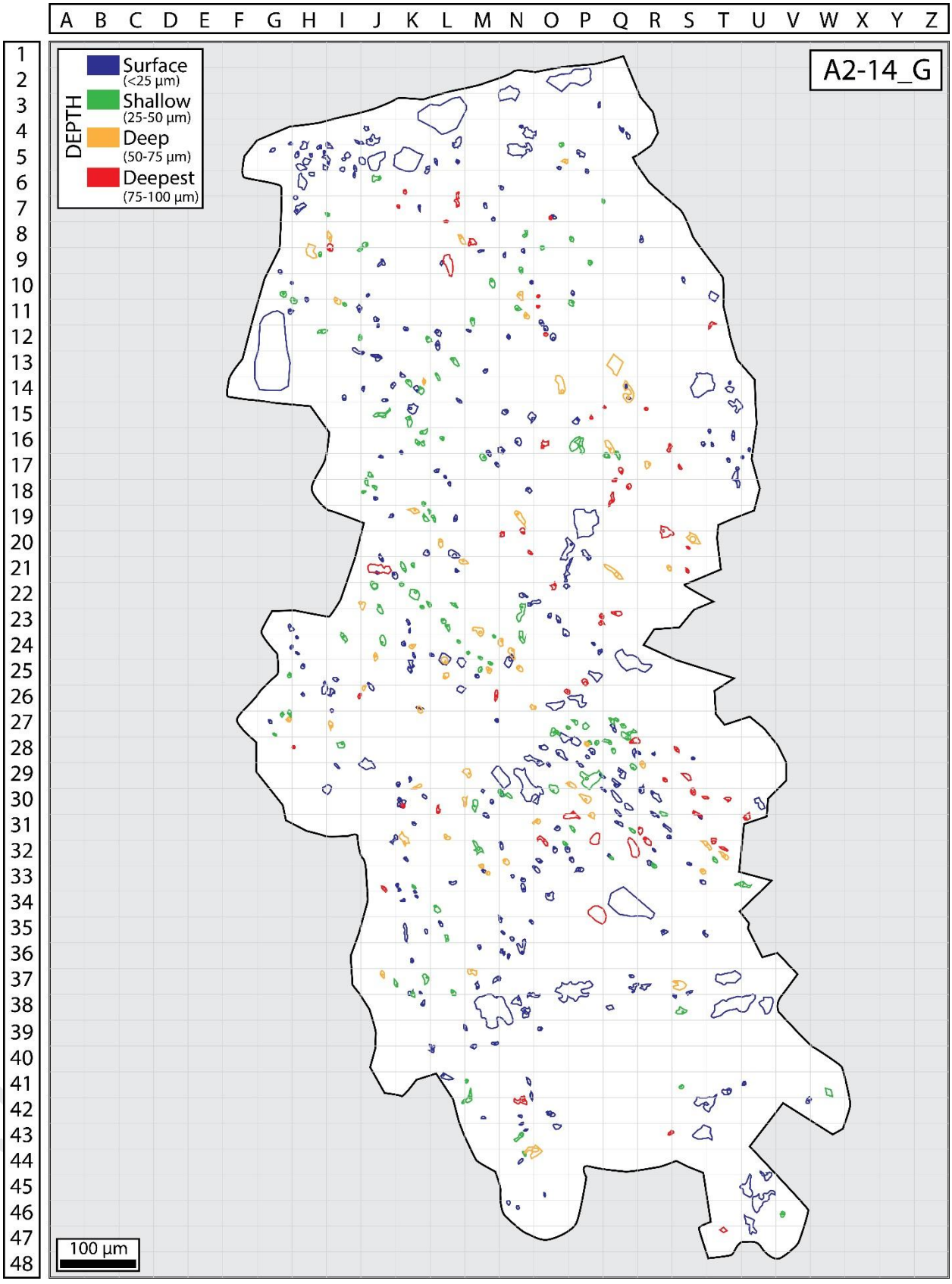

Fig. A1.7: Sample A2-14 (Area 5 Deposit, mineralised), Grain G

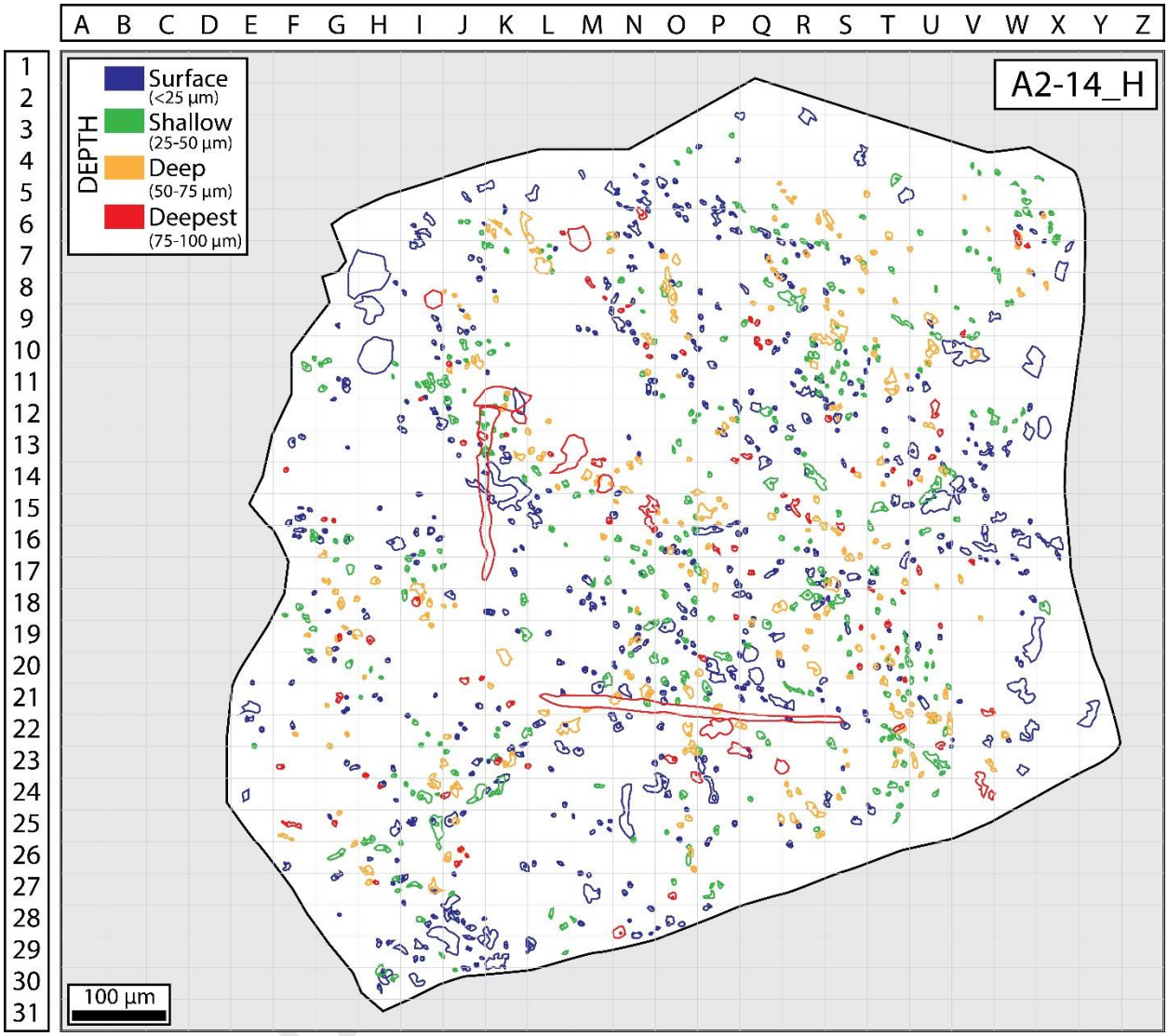

Fig. A1.8: Sample A2-14 (Area 5 Deposit, mineralised), Grain H

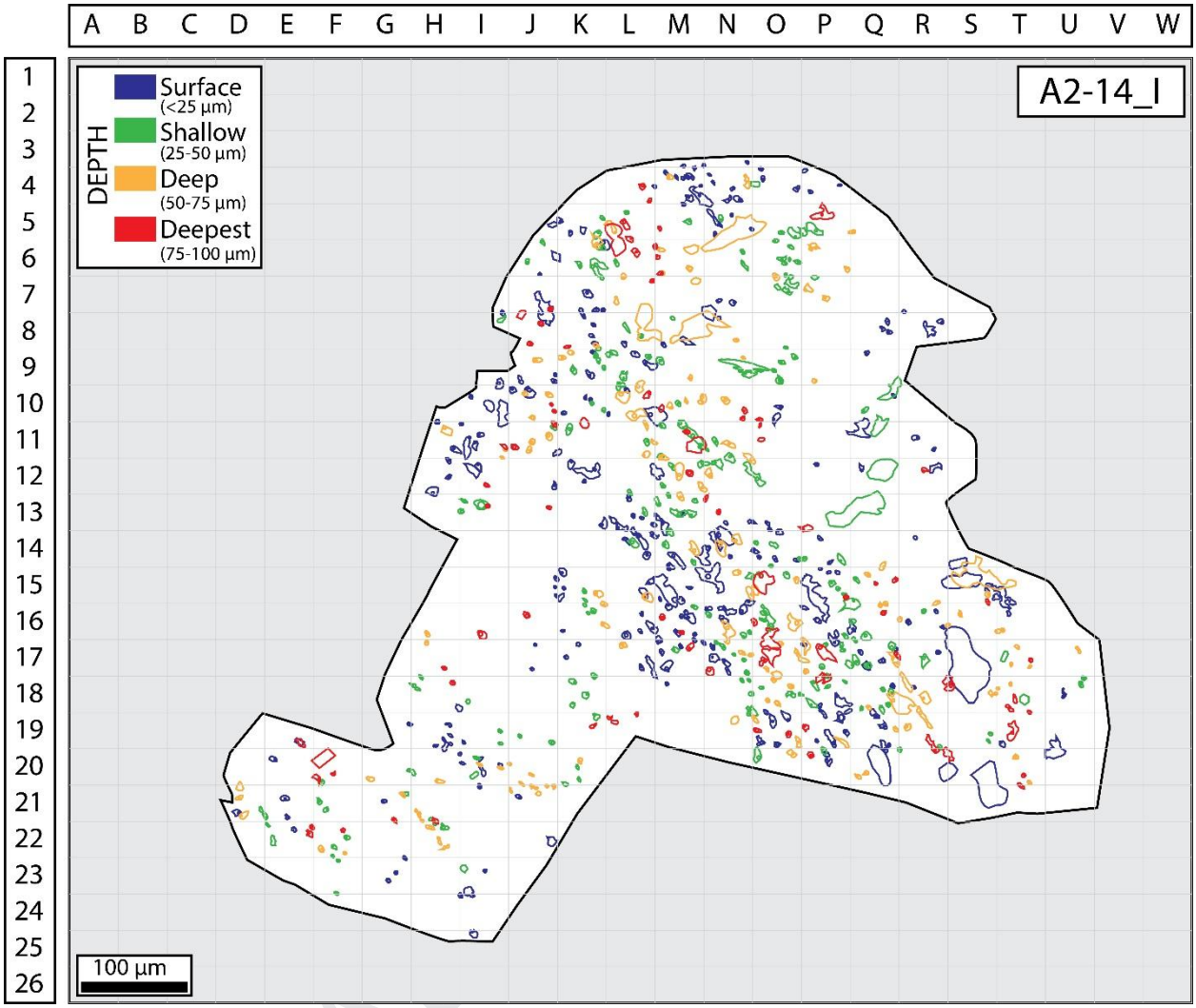

Fig. A1.9: Sample A2-14 (Area 5 Deposit, mineralised), Grain I

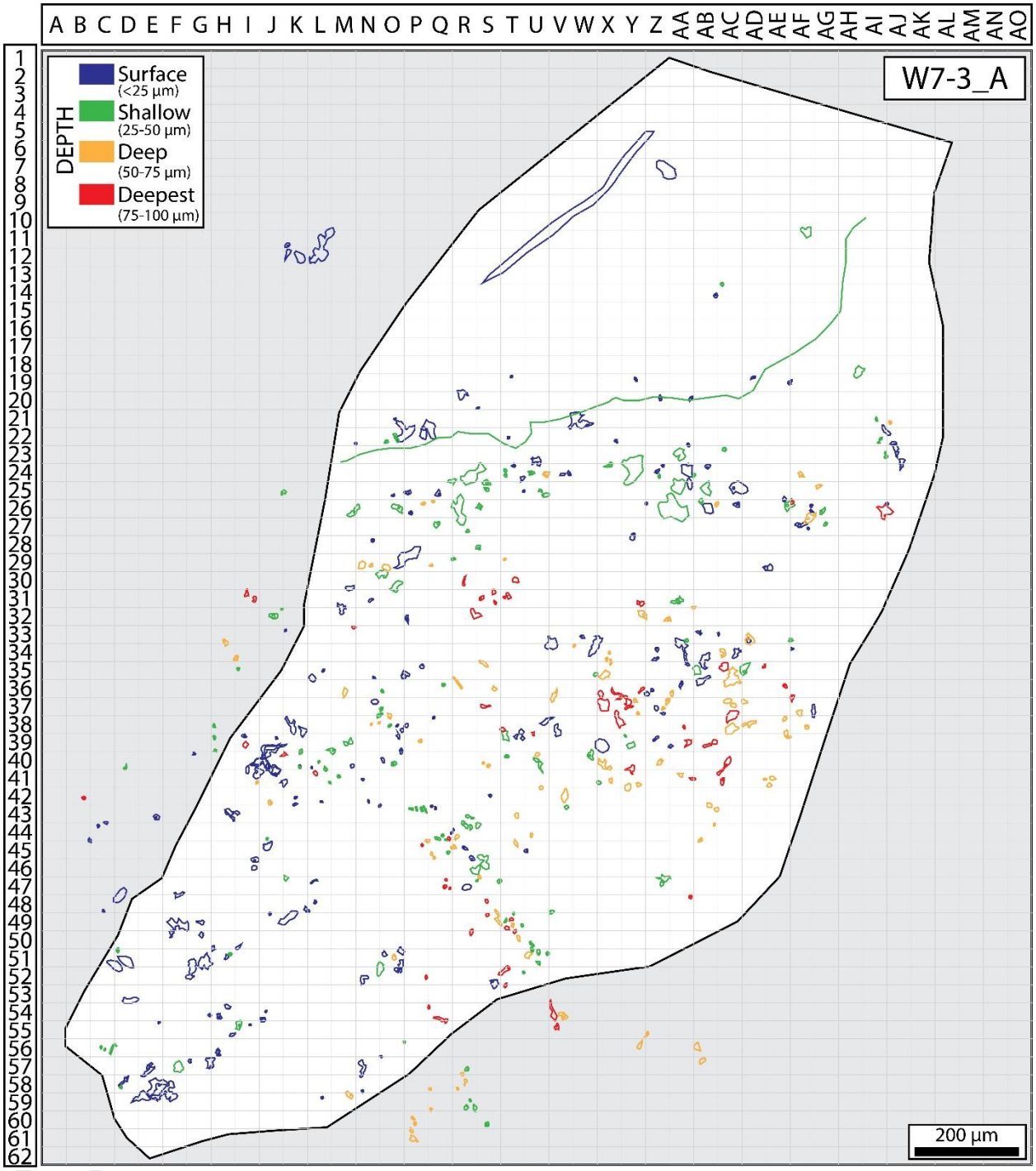

Fig. A1.10: Sample W7-3 (Wolverine Deposit, mineralised), Grain A

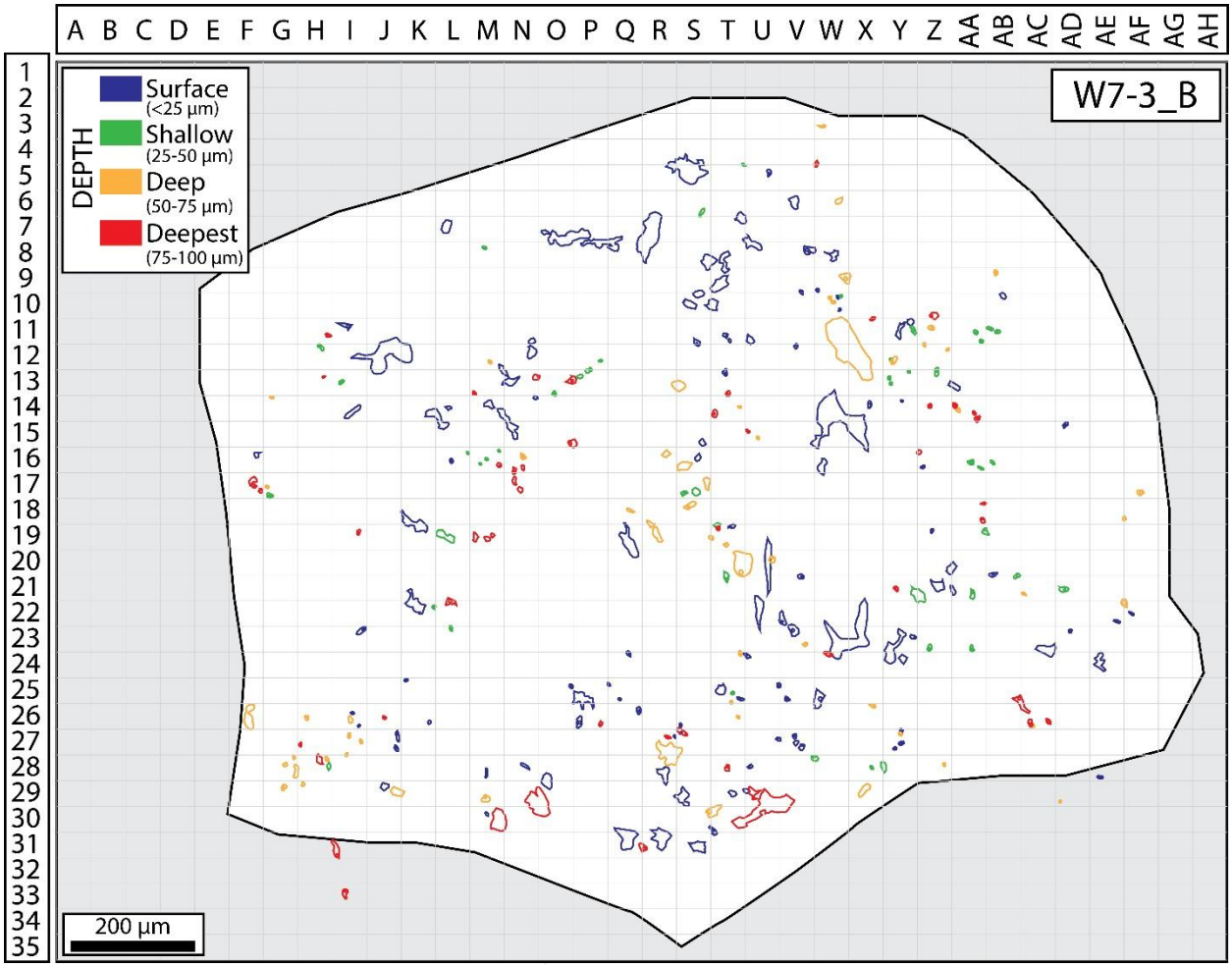

Fig. A1.11: Sample W7-3 (Wolverine Deposit, mineralised), Grain B

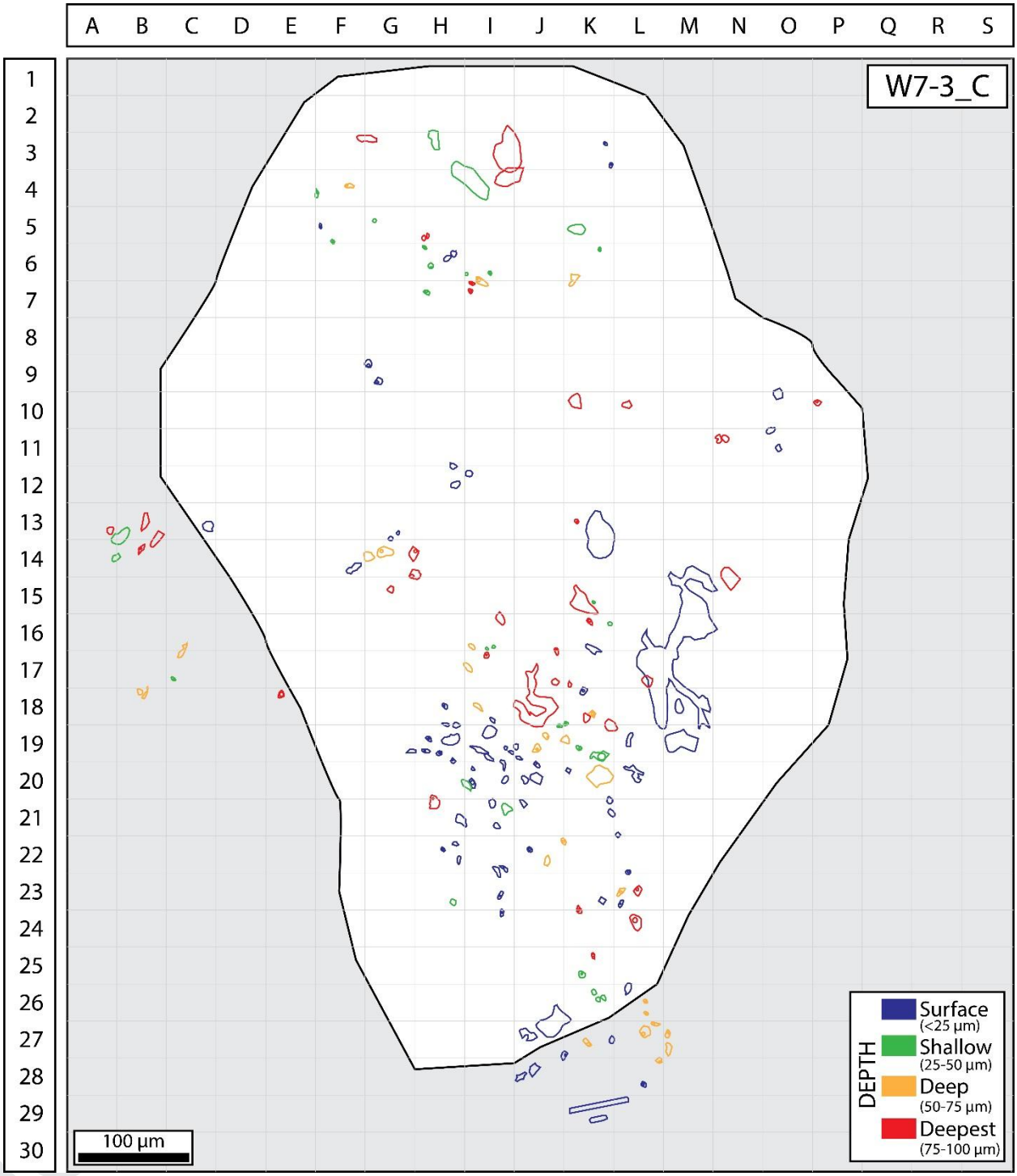

Fig. A1.12: Sample W7-3 (Wolverine Deposit, mineralised), Grain C

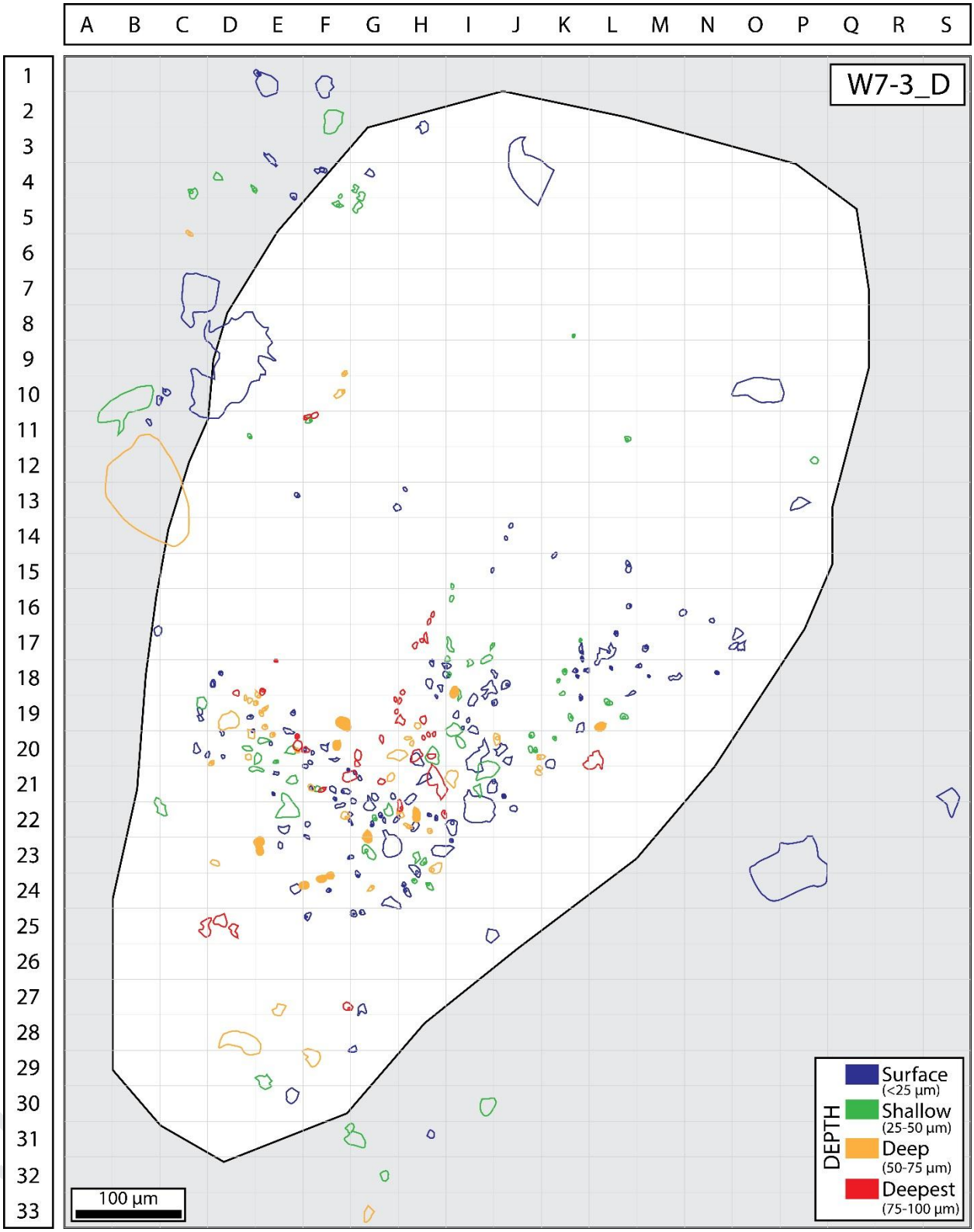

Fig. A1.13: Sample W7-3 (Wolverine Deposit, mineralised), Grain D

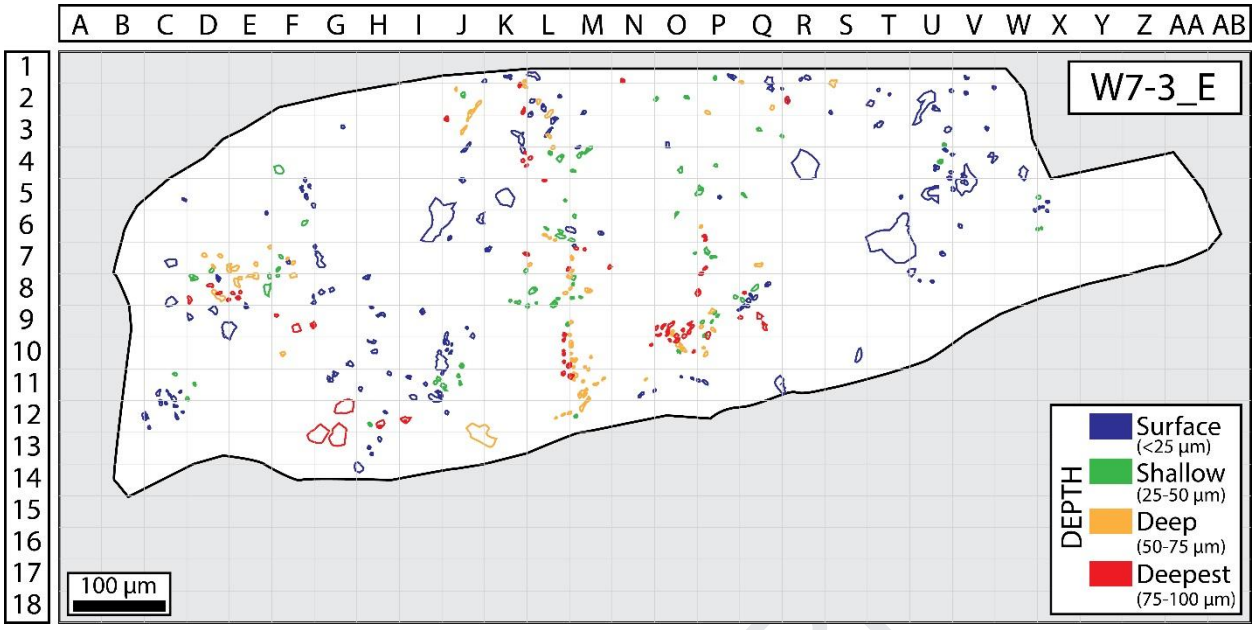

Fig. A1.14: Sample W7-3 (Wolverine Deposit, mineralised), Grain E

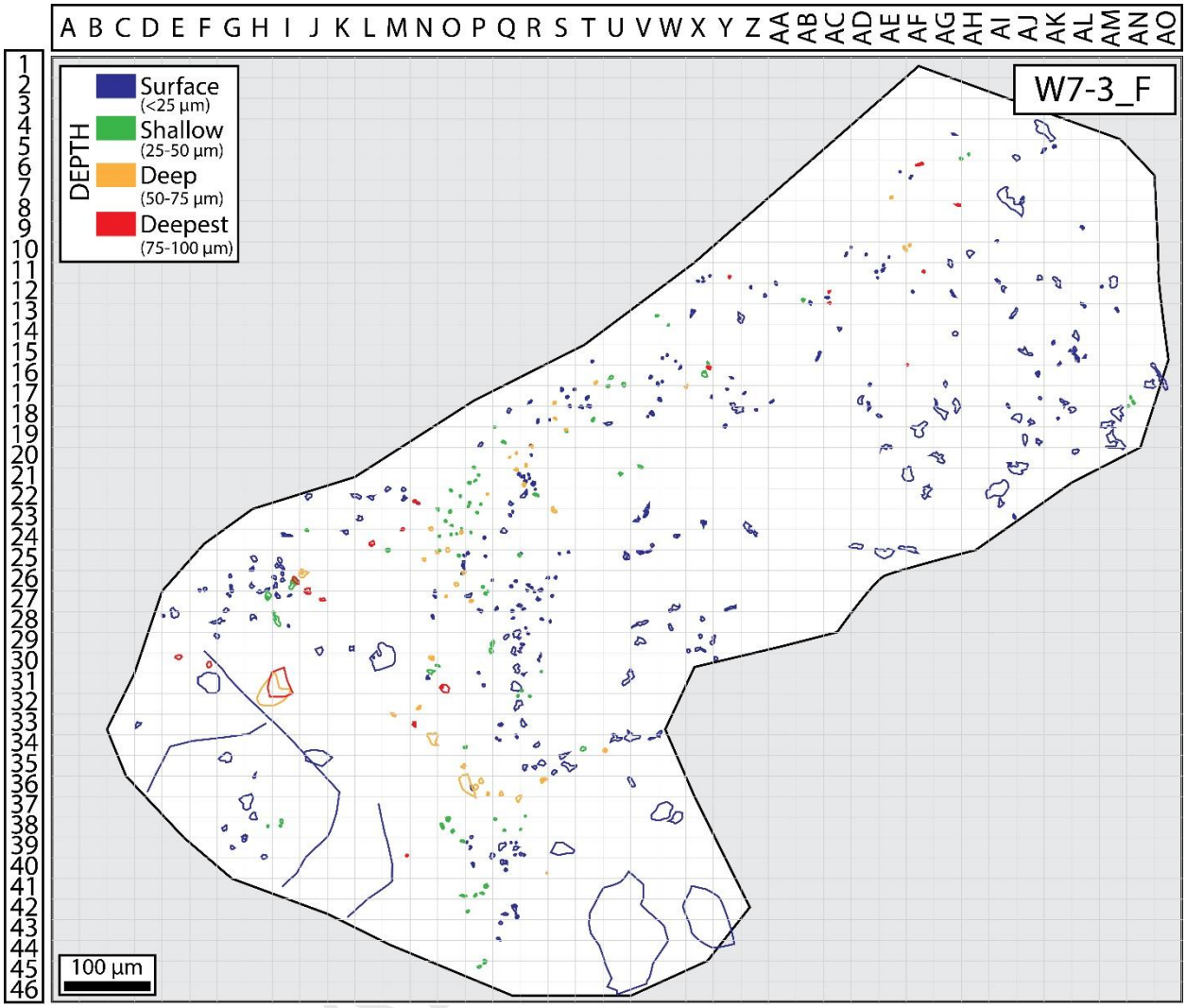

Fig. A1.15: Sample W7-3 (Wolverine Deposit, mineralised), Grain F

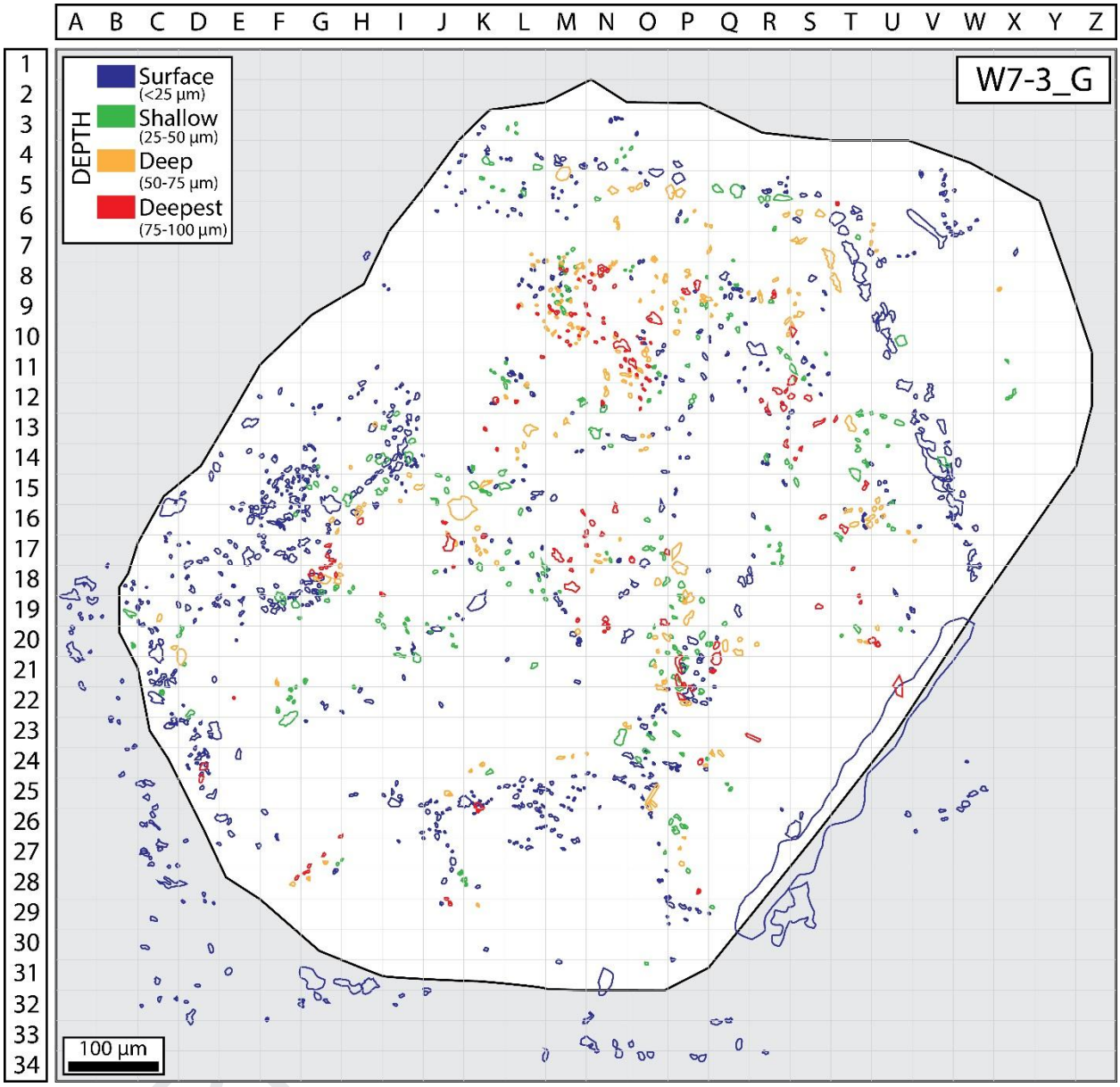

Fig. A1.16: Sample W7-3 (Wolverine Deposit, mineralised), Grain G

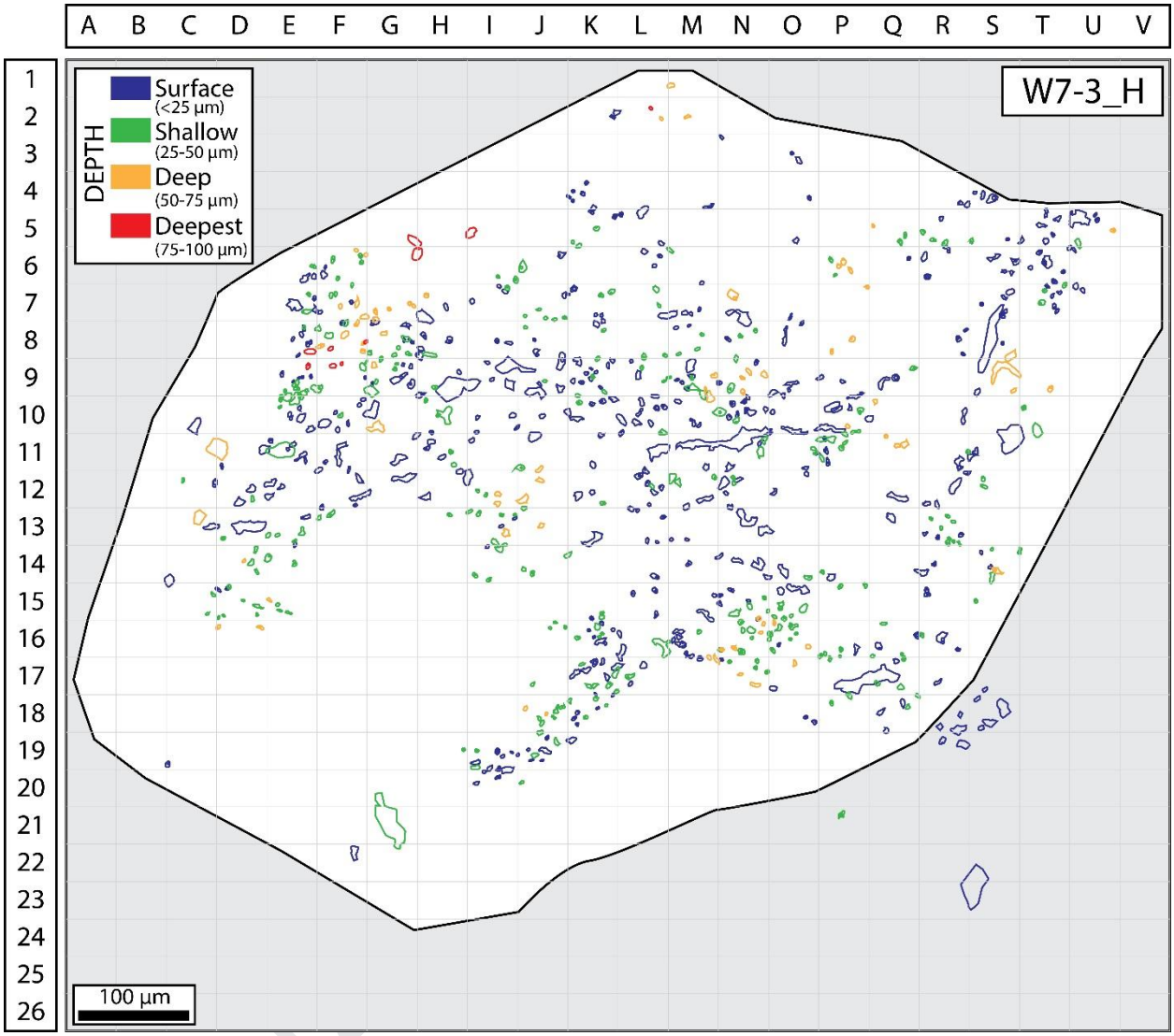

Fig. A1.17: Sample W7-3 (Wolverine Deposit, mineralised), Grain H

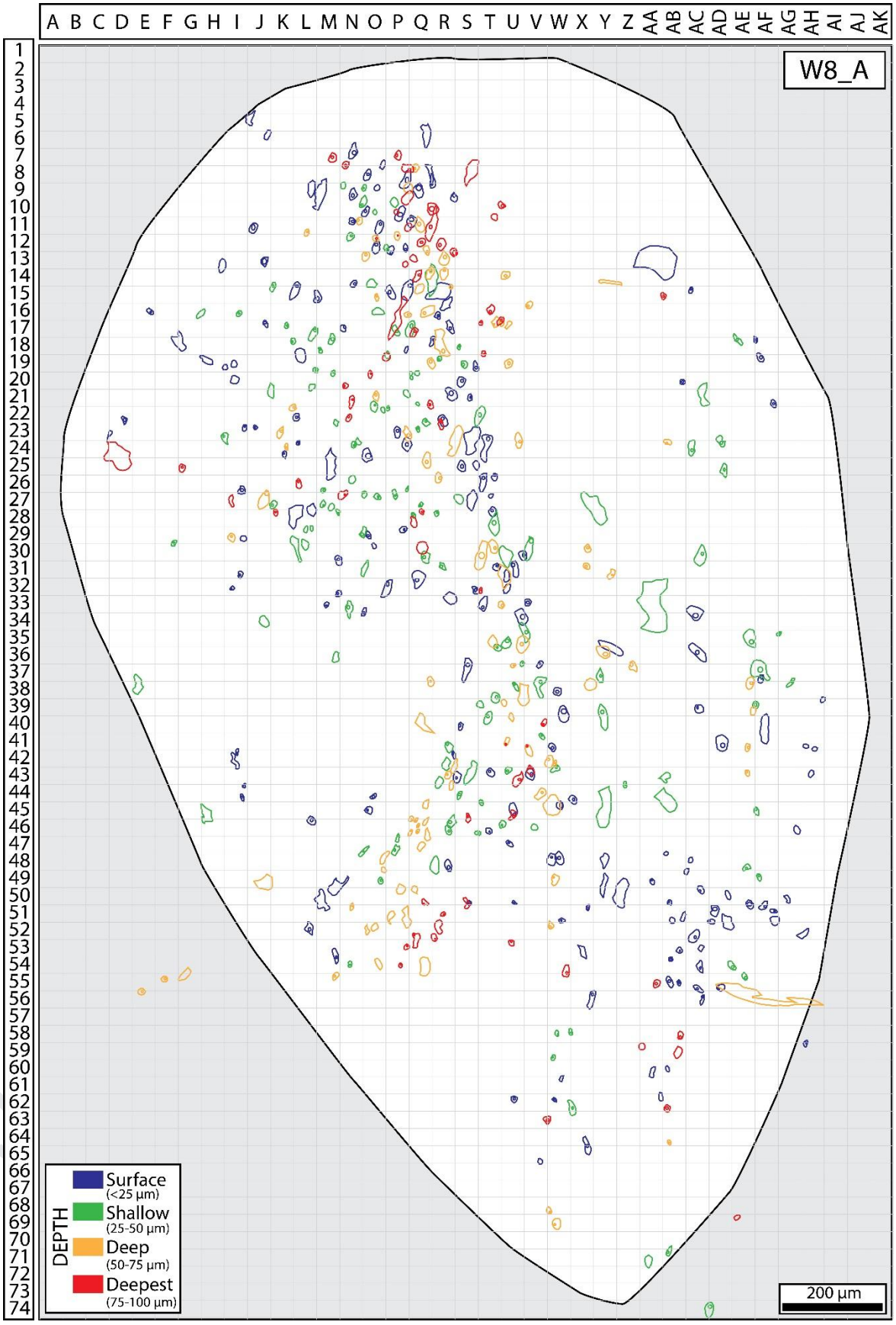

Fig. A1.18: Sample W8 (Wolverine Deposit, non-mineralised), Grain A

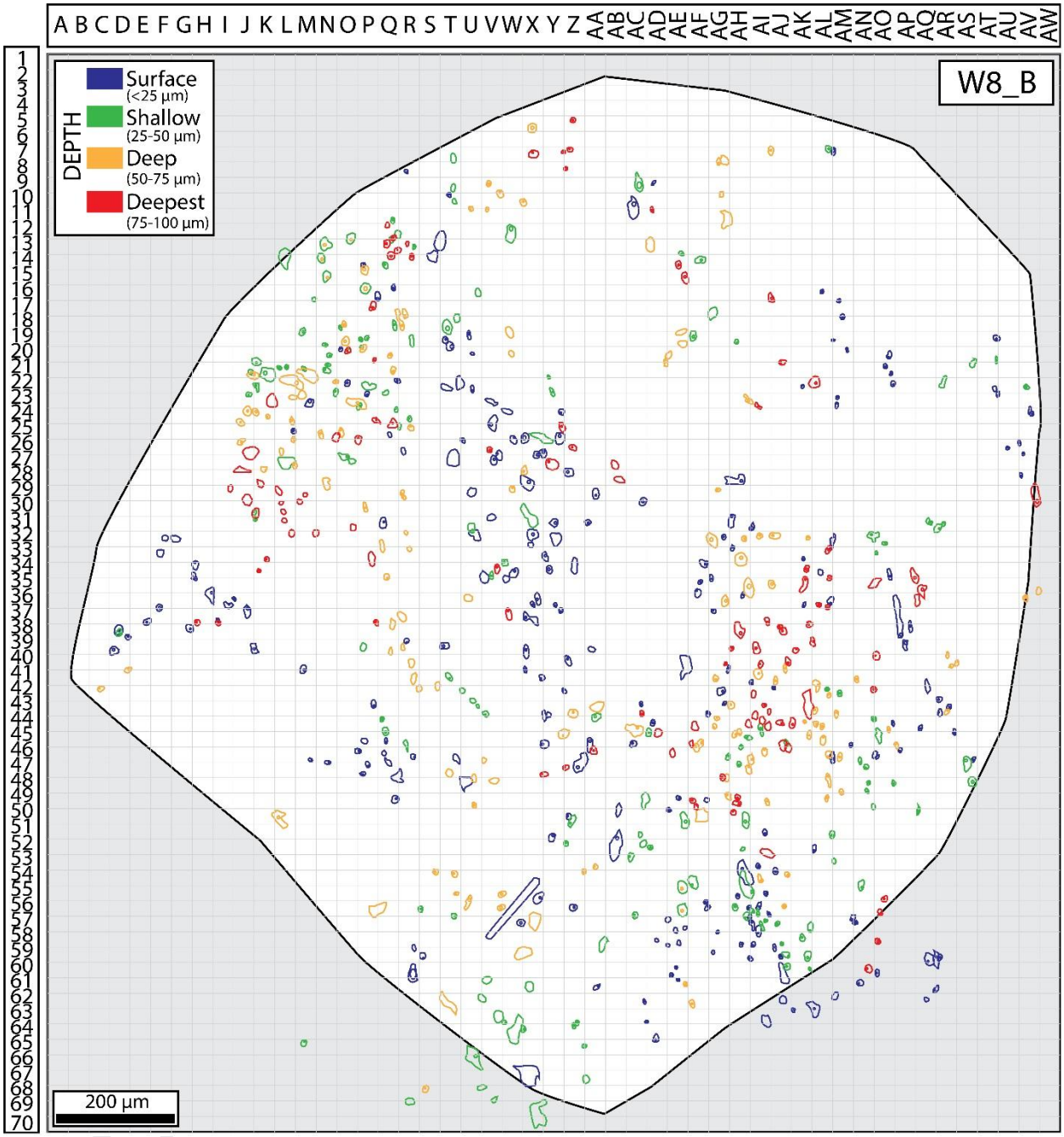

Fig. A1.19: Sample W8 (Wolverine Deposit, non-mineralised), Grain B

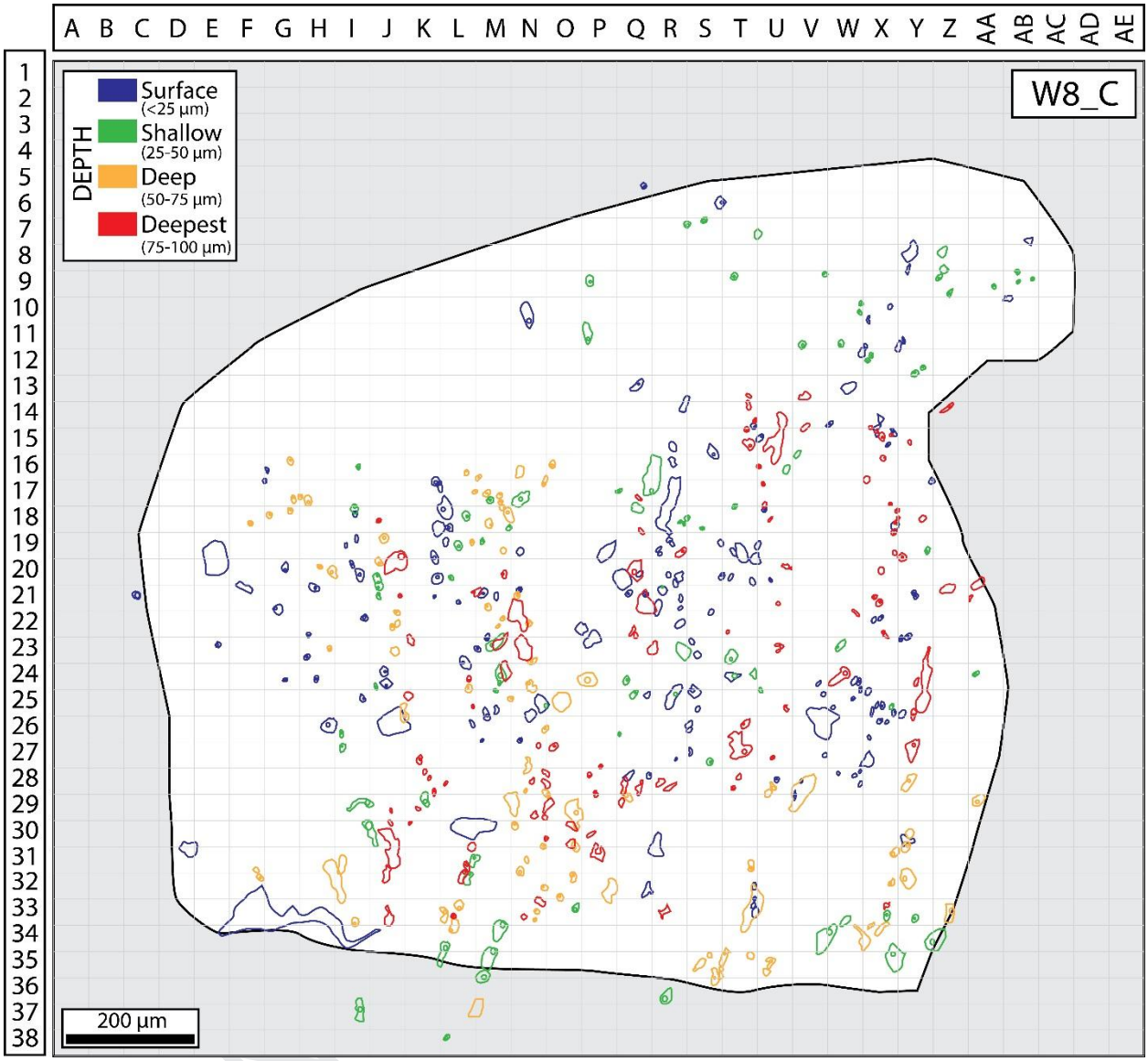

Fig. A1.20: Sample W8 (Wolverine Deposit, non-mineralised), Grain C

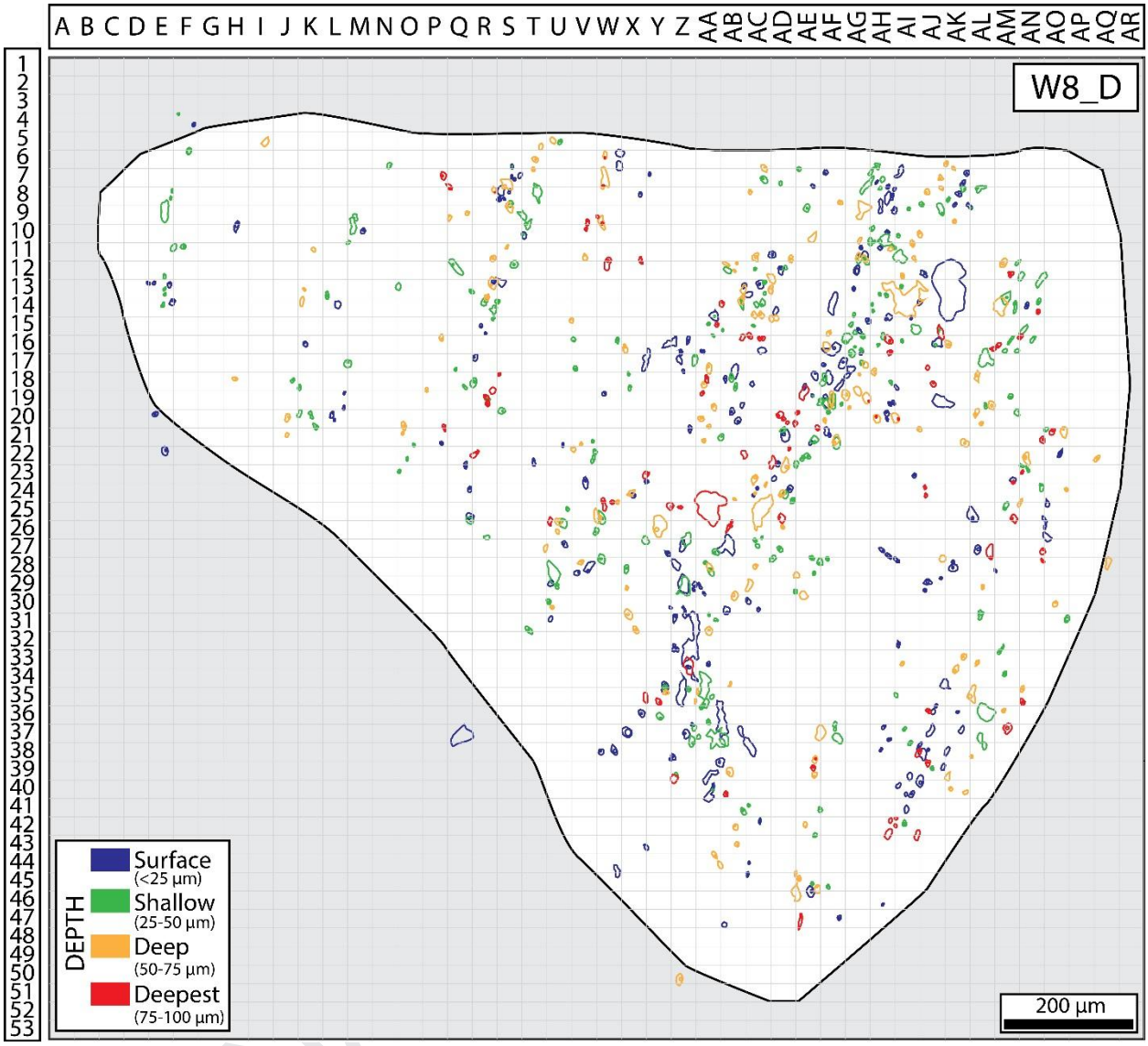

Fig. A1.21: Sample W8 (Wolverine Deposit, non-mineralised), Grain D

Appendix B: Composition of the standards for LA-ICP-MS analysis of fluid inclusions

Standard	Na (wt.%)	Si (wt.%)	P (wt.%)	Cl (wt.%)	K (wt.%)	Ca (wt.%)	Fe (wt.%)	Y (ppm)	Ce (ppm)	U (ppm)
T1G										
T1G-1	2.50	31.56	0.08	0.05	1.66	5.07	4.23	24.2	130.9	1.8
T1G-2	2.51	31.77	0.08	0.05	1.69	5.07	4.18	24.0	128.8	1.8
T1G-3	2.58	32.53	0.08	0.04	1.73	5.07	4.21	23.9	129.2	1.8
T1G-4	2.49	31.66	0.08	0.05	1.66	5.07	4.37	23.8	130.2	1.8
T1G-5	2.46	30.78	0.08	0.04	1.62	5.07	4.39	24.1	130.7	1.8
T1G-6	2.51	32.43	0.08	0.05	1.67	5.07	4.34	24.4	131.1	1.8
T1G-7	2.47	32.04	0.08	0.05	1.63	5.07	4.34	24.3	129.2	1.8
Average	2.50	31.83	0.08	0.05	1.66	5.07	4.29	24.1	130.0	1.8
SD	0.04	0.59	0.00	0.00	0.04	0.00	0.08	0.2	0.9	0.0

SD %	1.55	1.86	1.31	8.86	2.32	0.00	1.96	0.8	0.7	1.7
GSD										
GSD-1	2.86	28.42	0.10	0.05	2.55	5.15	8.26	41.0	41.6	41.3
GSD-2	2.84	28.46	0.10	0.05	2.56	5.15	8.27	40.5	41.5	41.4
GSD-3	2.85	27.96	0.09	0.05	2.54	5.15	8.23	40.8	41.7	42.1
GSD-4	2.83	28.32	0.10	0.05	2.49	5.15	8.62	40.9	41.9	41.9
GSD-5	2.88	28.62	0.10	0.04	2.54	5.15	8.62	41.0	41.8	42.1
GSD-6	2.81	29.33	0.10	0.05	2.46	5.15	8.64	41.6	41.9	42.4
GSD-7	2.74	28.36	0.10	0.05	2.40	5.15	8.45	41.5	41.7	42.1
Average	2.83	28.50	0.10	0.05	2.50	5.15	8.44	41.0	41.7	41.9
SD	0.05	0.42	0.00	0.00	0.06	0.00	0.19	0.4	0.2	0.4
SD %	1.65	1.47	1.48	7.52	2.40	0.00	2.23	0.9	0.4	1.0

Appendix C: Microthermometry data of primary fluid inclusions in different quartz grains

Sample/Grain	Number of FI	Type	T_{mi}	T_m	T_h	Salinity (wt. %)
Sample W8						
Grain A	49	Type I	-7 – -17.7	-0.1 – -5.2	171.7 – 338.8	0.2 – 8.1
Grain B	50	Type I	-7.1 – -14.4	-0.1 – -5.5	170 – 340	0.2 – 8.5
Grain C	65	Type I	-7 – -13	-0.1 – -4.5	179.1 – 341.1	0.2 – 7.2
Grain D	62	Type I	-6 – -14	-0.1 – -3.8	170 – 350	0.2 – 6.2
Total	226	Type I	-6 – -17.7	-0.1 – -5.5	170 – 350	0.2 – 8.5
Sample A2-14						
Grain A	10	Type I	-9.7 – -15.5	-1.1 – -1.8	139.8 – 250	1.9 – 3.1
Grain A	2	Type II	-15 – -16	-9.8 – -10.1	155.6 – 166.5	13.7 – 14
Grain A	6	Type III	-33 – -50.3	-17.8 – -24.8	102.7 – 180	17.8 – 24.8
Grain B	23	Type I	-4.4 – -16.6	-0.1 — -4.6	99.1 – 269.5	0.2 – 7.3
Grain B	12	Type III	-23.3 – -51.1	-0.8 – -25.2	120.7 – 201.7	0.8 – 25.2
Grain C	15	Type I	-7 – -17.1	-0.1 – -6.5	128.6 – 243.9	0.2 – 9.9
Grain C	1	Type III	-37.7	-7.6	201	7.6
Grain D	3	Type I	-6.1 – -16	-0.1 – -6.5	123 – 236.6	0.2 – 9.9
Grain E	40	Type I	-5.2 – -17.7	-0.1 – -4.5	155.4 – 268.1	0.2 – 7.2
Grain E	1	Type II	-17	-12.1	198.1	16.1
Grain E	3	Type III	-24.4 – -49.1	-0.5 – -24.3	159.8 – 211.5	0.5 – 24.3
Grain G	12	Type I	-6 – -17	-0.1 – -6.1	119.9 – 220	0.2 – 9.3
Grain G	2	Type II	-16.6 – -16.7	-12.1 – -12.9	156.9 – 220.2	16.1 – 16.8
Grain G	13	Type III	-25.5 – -50.5	-3.5 – -24.6	115.1 – 241.2	3.5 – 24.6
Grain H	9	Type I	-7.7 – -19	-0.4 – -6.2	149.9 – 241.1	0.7 – 9.5
Grain H	3	Type II	-16	-14.4	213.3 – 200.1	18.1
Grain H	11	Type III	-22.9 – -51.3	-0.5 – -25.8	112.7 – 164.5	0.5 – 25.8
Grain I	22	Type I	-7 – -16.6	-0.1 – -3.6	140.5 – 272.3	0.2 – 5.9
Grain I	1	Type II	-21	-9.3	222.2	13.2
Grain I	3	Type III	-23.1 – -49.5	-0.6 – -24.6	143.2 – 207.7	0.6 – 24.6
Total	134	Type I	-4.4 – -17.1	-0.1 – -6.5	99.1 – 272.3	0.2 – 9.9
Total	9	Type II	-15 – -21	-9.3 – -12.9	155.6 – 222.2	13.2 – 18.1
Total	49	Type III	-22.9 – -51.3	-0.5 – -25.8	102.7 – 241.2	0.5 – 25.8
Sample W7-3						
Grain A	16	Type I	-6 – -16.7	-0.1 – -6.4	135 – 257	0.2 – 9.7
Grain A	6	Type III	-26.6 – -39.5	-2.1 – -15.1	132.5 – 210	2.1 – 15.1
Grain B	9	Type I	-8 – -17.7	-0.1 – -4.5	141.9 – 228.7	0.2 – 7.2
Grain B	2	Type III	-38.8 – -48.7	-19.4 – -21.4	116.7 – 174.5	19.4 – 21.4
Grain D	9	Type I	-7 – -11.1	-0.1 – -2.1	125.6 – 250.1	0.2 – 3.5
Grain D	1	Type II	-13	-8.8	200	12.6
Grain D	2	Type III	-33.3 – -37.2	-10.9 – -12.5	151.4 – 184.4	10.9 – 12.5
Grain E	6	Type I	-7 – -16.5	-0.1 – -3.5	120.9 – 224.7	0.2 – 5.7
Grain E	1	Type III	-31.1	-10.1	211.1	10.1
Grain F	17	Type I	-7 – -16	-0.1 – -6.2	131.9 – 241.7	0.2 – 9.5
Grain F	2	Type III	-29.5 – -48.8	-8.9 – -20.8	148.3 – 191.3	8.9 – 20.8
Grain G	7	Type I	-7 – -9	-0.1 – -0.5	167.6 – 220	0.2 – 0.9
Grain G	4	Type III	-23.3 – -27.6	-1.1 – -2.2	165 – 193.3	1.1 – 2.2
Grain H	34	Type I	-5 – -16.7	-0.1 – -4.5	121.9 – 255.5	0.2 – 7.2
Grain H	7	Type III	-28.5 – -47.6	-1.9 – -19.1	157.7 – 225.5	1.9 – 19.1
Total	98	Type I	-5 – -17.7	-0.1 – -6.4	120.9 – 257	0.2 – 9.7
Total	1	Type II	-13	-8.8	200	12.6
Total	24	Type III	-23.3 – -48.8	-1.1 – -21.4	116.7 – 22.5	1.1 – 21.4

Notes: Type I: Low salinity H_2O-NaCl; Type II: Medium salinity H_2O-NaCl; Type III: High salinity H_2O-$CaCl_2$-NaCl. Due to the lack of a next-to-last solid phase, accurate calculation of the salinity of the type III fluid inclusions was not possible. Instead, T_m was used as a rough estimation of the salinity.

Appendix D: Fluid inclusion microthermometry dataset

Type	Composition	Deposit	Sample	Grain	FI No.	Bubble size	T_{mi}	T_m	T_h	Phases	Salinity	ρ (g/cm^3)
I	H_2O-NaCl	Wolverine	W8	A	AC34	S	-8	-0.1	217.7	L+V	0.2	0.84
I	H_2O-NaCl	Wolverine	W8	A	AC36	S	-8	-0.1	223.4	L+V	0.2	0.84
I	H_2O-NaCl	Wolverine	W8	A	AC39	S	-8	-0.1	205.5	L+V	0.2	0.86
I	H_2O-NaCl	Wolverine	W8	A	AD41	S	-7	-0.2	204.1	L+V	0.4	0.86
I	H_2O-NaCl	Wolverine	W8	A	AE35	S	-7	-0.5	210.3	L+V	0.9	0.86
I	H_2O-NaCl	Wolverine	W8	A	AF37	L	-10.5	-0.4	250.6	L+V	0.7	0.80
I	H_2O-NaCl	Wolverine	W8	A	AE39	S	-11.1	-0.7	238.1	L+V	1.2	0.82
I	H_2O-NaCl	Wolverine	W8	A	AF41	S	-10	-0.2	231.4	L+V	0.4	0.83

I	H_2O-NaCl	Wolverine	W8	A	AC30	S	-9	-0.1	202.7	L+V	0.2	0.86
I	H_2O-NaCl	Wolverine	W8	A	Y27	S	-10.5	-0.5	188.1	L+V	0.9	0.89
I	H_2O-NaCl	Wolverine	W8	A	AB24	S	-10.1	-0.7	210.3	L+V	1.2	0.86
I	H_2O-NaCl	Wolverine	W8	A	AC24	S	-10.1	-0.7	207.8	L+V	1.2	0.87
I	H_2O-NaCl	Wolverine	W8	A	AD24	S	-11	-0.9	190.3	L+V	1.6	0.89
I	H_2O-NaCl	Wolverine	W8	A	AD25	S	-11	-0.9	247.1	L+V	1.6	0.81
I	H_2O-NaCl	Wolverine	W8	A	AF19	S	-11	-0.3	283.5	L+V	0.5	0.74
I	H_2O-NaCl	Wolverine	W8	A	S20	S	-12	-0.8	282.7	L+V	1.4	0.75
I	H_2O-NaCl	Wolverine	W8	A	R21	S	-12	-0.8	290.1	L+V	1.4	0.74
I	H_2O-NaCl	Wolverine	W8	A	R22	S	-12	-1.1	200.4	L+V	1.9	0.88
I	H_2O-NaCl	Wolverine	W8	A	P23	S	-10	-0.7	216.2	L+V	1.2	0.85
I	H_2O-NaCl	Wolverine	W8	A	P24	S	-10	-0.7	236.6	L+V	1.2	0.83
I	H_2O-NaCl	Wolverine	W8	A	S25	S	-10	-0.9	301.1	L+V	1.6	0.72
I	H_2O-NaCl	Wolverine	W8	A	Q25	S	-16	-4.8	290.4	L+V	7.6	0.81
I	H_2O-NaCl	Wolverine	W8	A	R26	S	-16.1	-5.2	294.7	L+V	8.1	0.81
I	H_2O-NaCl	Wolverine	W8	A	U27	S	-9	-0.7	315.8	L+V	1.2	0.68
I	H_2O-NaCl	Wolverine	W8	A	M25	S	-14.4	-2.3	201.1	L+V	3.9	0.89
I	H_2O-NaCl	Wolverine	W8	A	O27	S	-12	-1.8	217.6	L+V	3.1	0.87
I	H_2O-NaCl	Wolverine	W8	A	M30	S	-12.5	-2.5	290.3	L+V	4.2	0.77
I	H_2O-NaCl	Wolverine	W8	A	Q30	S	-12.5	-2.8	290.7	L+V	4.6	0.77
I	H_2O-NaCl	Wolverine	W8	A	Q32	S	-12.5	-2.8	198.5	L+V	4.6	0.90
I	H_2O-NaCl	Wolverine	W8	A	R31	S	-14	-3.4	240.9	L+V	5.6	0.86
I	H_2O-NaCl	Wolverine	W8	A	N7	S	-10.1	-1.1	171.7	L+V	1.9	0.91
I	H_2O-NaCl	Wolverine	W8	A	O8	S	-10.1	-1.1	184.3	L+V	1.9	0.90
I	H_2O-NaCl	Wolverine	W8	A	O11	S	-7	-0.5	178	L+V	0.9	0.90
I	H_2O-NaCl	Wolverine	W8	A	O12	S	-7	-0.5	233.7	L+V	0.9	0.83
I	H_2O-NaCl	Wolverine	W8	A	P8	L	-7	-0.8	330.1	L+V	1.4	0.66
I	H_2O-NaCl	Wolverine	W8	A	Q9	L	-7	-0.8	325.2	L+V	1.4	0.67
I	H_2O-NaCl	Wolverine	W8	A	R10	S	-12.9	-2.9	338.8	L+V	4.8	0.69
I	H_2O-NaCl	Wolverine	W8	A	Q11	S	-12.9	-2.9	190.5	L+V	4.8	0.91
I	H_2O-NaCl	Wolverine	W8	A	R12	S	-17.7	-3.6	258.1	L+V	5.9	0.84
I	H_2O-NaCl	Wolverine	W8	A	R18	S	-15	-2.7	298.2	L+V	4.5	0.76
I	H_2O-NaCl	Wolverine	W8	A	R19	S	-15	-3.1	288.8	L+V	5.1	0.78
I	H_2O-NaCl	Wolverine	W8	A	Y36	S	-9	-0.7	217	L+V	1.2	0.85
I	H_2O-NaCl	Wolverine	W8	A	W38	S	-11.1	-1.2	221.5	L+V	2.1	0.85
I	H_2O-NaCl	Wolverine	W8	A	W39	S	-11.1	-1.3	203.7	L+V	2.2	0.88
I	H_2O-NaCl	Wolverine	W8	A	W41	S	-10	-0.7	257.7	L+V	1.2	0.79
I	H_2O-NaCl	Wolverine	W8	A	V43	S	-10	-0.9	248.2	L+V	1.6	0.81
I	H_2O-NaCl	Wolverine	W8	A	W45	S	-11	-1.3	205.8	L+V	2.2	0.88
I	H_2O-NaCl	Wolverine	W8	A	X44	S	-10	-0.3	214.3	L+V	0.5	0.85
I	H_2O-NaCl	Wolverine	W8	A	W48_1	S	-9	-0.1	189.1	L+V	0.2	0.88
I	H_2O-NaCl	Wolverine	W8	B	AA45	S	-9	-1.1	280.1	L+V	1.9	0.76
I	H_2O-NaCl	Wolverine	W8	B	X45	S	-11	-1.2	277	L+V	2.1	0.77
I	H_2O-NaCl	Wolverine	W8	B	AD44	S	-11.5	-1.6	260.4	L+V	2.7	0.80
I	H_2O-NaCl	Wolverine	W8	B	H36	S	-9.5	-0.3	180.9	L+V	0.5	0.89
I	H_2O-NaCl	Wolverine	W8	B	G38	S	-9.5	-0.7	235.4	L+V	1.2	0.83
I	H_2O-NaCl	Wolverine	W8	B	F36	L	-8	-0.1	201.1	L+V	0.2	0.87
I	H_2O-NaCl	Wolverine	W8	B	E37	S	-8	-0.5	205.5	L+V	0.9	0.87
I	H_2O-NaCl	Wolverine	W8	B	J37	S	-8.5	-0.1	230.1	L+V	0.2	0.83
I	H_2O-NaCl	Wolverine	W8	B	J39	S	-8.5	-0.9	200.7	L+V	1.6	0.88
I	H_2O-NaCl	Wolverine	W8	B	M41	S	-8.5	-0.8	209.1	L+V	1.4	0.87
I	H_2O-NaCl	Wolverine	W8	B	F32	S	-7.1	-0.3	195.3	L+V	0.5	0.88
I	H_2O-NaCl	Wolverine	W8	B	F33	S	-7.1	-0.3	188.7	L+V	0.5	0.88
I	H_2O-NaCl	Wolverine	W8	B	G32	S	-7.1	-0.3	190.8	L+V	0.5	0.88
I	H_2O-NaCl	Wolverine	W8	B	D38	S	-7.1	-0.6	210.7	L+V	1.1	0.86
I	H_2O-NaCl	Wolverine	W8	B	D39	S	-7.1	-0.6	207.3	L+V	1.1	0.87
I	H_2O-NaCl	Wolverine	W8	B	D40	S	-7.1	-0.9	193.3	L+V	1.6	0.89
I	H_2O-NaCl	Wolverine	W8	B	E41	S	-7.1	-0.9	190.1	L+V	1.6	0.89
I	H_2O-NaCl	Wolverine	W8	B	Y25_1	S	-14.4	-3.5	209.5	L+V	5.7	0.90
I	H_2O-NaCl	Wolverine	W8	B	Z26	S	-14.4	-4.9	244.7	L+V	7.7	0.87
I	H_2O-NaCl	Wolverine	W8	B	Y27	L	-14	-5.1	322.2	L+V	8.0	0.76
I	H_2O-NaCl	Wolverine	W8	B	V26	S	-14	-3.5	214.4	L+V	5.7	0.89
I	H_2O-NaCl	Wolverine	W8	B	Y24	S	-13	-5.5	280.9	L+V	8.5	0.83
I	H_2O-NaCl	Wolverine	W8	B	X25	S	-13	-4.5	254.7	L+V	7.2	0.85
I	H_2O-NaCl	Wolverine	W8	B	W29	S	-13.5	-4.3	290.3	L+V	6.9	0.80
I	H_2O-NaCl	Wolverine	W8	B	V31	S	-14	-5.2	250.9	L+V	8.1	0.87
I	H_2O-NaCl	Wolverine	W8	B	AA29	S	-13	-3.5	220.1	L+V	5.7	0.89

(Continued)

Type	Composition	Deposit	Sample	Grain	FI No.	Bubble size	T_{mi}	T_m	T_h	Phases	Salinity	ρ (g/cm^3)
I	H_2O-NaCl	Wolverine	W8	B	AA31	S	-13.5	-3.5	200.7	L+V	5.7	0.91
I	H_2O-NaCl	Wolverine	W8	B	AC30	S	-13	-3.8	214.8	L+V	6.2	0.90
I	H_2O-NaCl	Wolverine	W8	B	U32	S	-13	-2.2	270.8	L+V	3.7	0.80
I	H_2O-NaCl	Wolverine	W8	B	V35	S	-13	-2.8	330.1	L+V	4.6	0.70
I	H_2O-NaCl	Wolverine	W8	B	U29	S	-10	-1.6	291.3	L+V	2.7	0.75
I	H_2O-NaCl	Wolverine	W8	B	W34	S	-10.5	-1.8	170	L+V	3.1	0.92

I	H_2O-NaCl	Wolverine	W8	B	Y37	S	-10.5	-1.6	247.3	L+V	2.7	0.82
I	H_2O-NaCl	Wolverine	W8	B	Y36	S	-11	-1.7	240.1	L+V	2.9	0.84
I	H_2O-NaCl	Wolverine	W8	B	Y35	S	-11.3	-1.8	239.3	L+V	3.1	0.84
I	H_2O-NaCl	Wolverine	W8	B	Y34	S	-11.3	-1.9	240.1	L+V	3.2	0.84
I	H_2O-NaCl	Wolverine	W8	B	Y31	S	-11.4	-2.1	237.3	L+V	3.5	0.85
I	H_2O-NaCl	Wolverine	W8	B	AE40	S	-10.5	-1.4	240.1	L+V	2.4	0.83
I	H_2O-NaCl	Wolverine	W8	B	AF44	S	-10.2	-1.2	241	L+V	2.1	0.83
I	H_2O-NaCl	Wolverine	W8	B	AH31	S	-12.2	-1.8	197	L+V	3.1	0.89
I	H_2O-NaCl	Wolverine	W8	B	AI31	S	-12	-1.8	198.8	L+V	3.1	0.89
I	H_2O-NaCl	Wolverine	W8	B	AG32	S	-11.1	-1.3	217.7	L+V	2.2	0.86
I	H_2O-NaCl	Wolverine	W8	B	AL32	S	-10.1	-1.9	241.3	L+V	3.2	0.84
I	H_2O-NaCl	Wolverine	W8	B	AH35	L	-10	-1.1	259.9	L+V	1.9	0.80
I	H_2O-NaCl	Wolverine	W8	B	AG36	S	-10.2	-1.2	240.3	L+V	2.1	0.83
I	H_2O-NaCl	Wolverine	W8	B	AH38	S	-10	-1.5	248.1	L+V	2.6	0.82
I	H_2O-NaCl	Wolverine	W8	B	AJ35	S	-11	-0.9	237.7	L+V	1.6	0.83
I	H_2O-NaCl	Wolverine	W8	B	AK34	S	-12	-1.4	220.5	L+V	2.4	0.86
I	H_2O-NaCl	Wolverine	W8	B	AK35	S	-9	-0.8	231.1	L+V	1.4	0.84
I	H_2O-NaCl	Wolverine	W8	B	L14	L	-10	-2.1	340	L+V	3.5	0.67
I	H_2O-NaCl	Wolverine	W8	C	N10	S	-10.5	-1.5	187.7	L+V	2.6	0.90
I	H_2O-NaCl	Wolverine	W8	C	N8	S	-10.5	-2.2	205.7	L+V	3.7	0.89
I	H_2O-NaCl	Wolverine	W8	C	K13	S	-11	-1.5	198.7	L+V	2.6	0.89
I	H_2O-NaCl	Wolverine	W8	C	K14	S	-11.3	-1.8	182.2	L+V	3.1	0.91
I	H_2O-NaCl	Wolverine	W8	C	K15	S	-13	-3.4	179.1	L+V	5.6	0.93
I	H_2O-NaCl	Wolverine	W8	C	J11	S	-11.4	-1.2	201.3	L+V	2.1	0.88
I	H_2O-NaCl	Wolverine	W8	C	M11	S	-10.5	-0.7	199.3	L+V	1.2	0.88
I	H_2O-NaCl	Wolverine	W8	C	M8_1	S	-12	-2.5	210.3	L+V	4.2	0.89
I	H_2O-NaCl	Wolverine	W8	C	M8_2	S	-12	-2.5	200.3	L+V	4.2	0.90
I	H_2O-NaCl	Wolverine	W8	C	N9	S	-12	-2.8	191.1	L+V	4.6	0.91
I	H_2O-NaCl	Wolverine	W8	C	M7	S	-13	-4.5	183.2	L+V	7.2	0.94
I	H_2O-NaCl	Wolverine	W8	C	N5_1	S	-10.1	-2.2	202.2	L+V	3.7	0.89
I	H_2O-NaCl	Wolverine	W8	C	N5_2	S	-10	-2.5	203.8	L+V	4.2	0.89
I	H_2O-NaCl	Wolverine	W8	C	M6	S	-13	-3.1	180.3	L+V	5.1	0.93
I	H_2O-NaCl	Wolverine	W8	C	L7_1	S	-13	-3.3	179.7	L+V	5.4	0.93
I	H_2O-NaCl	Wolverine	W8	C	L7_2	S	-11	-2.3	181.1	L+V	3.9	0.92
I	H_2O-NaCl	Wolverine	W8	C	L6	L	-12	-0.3	311.5	L+V	0.5	0.68
I	H_2O-NaCl	Wolverine	W8	C	AA10	S	-9	-0.7	187.7	L+V	1.2	0.89
I	H_2O-NaCl	Wolverine	W8	C	AA9	S	-10	-0.9	201.3	L+V	1.6	0.88
I	H_2O-NaCl	Wolverine	W8	C	Z11	S	-7	-0.5	180	L+V	0.9	0.90
I	H_2O-NaCl	Wolverine	W8	C	Z7	L	-7	-0.4	193.3	L+V	0.7	0.88
I	H_2O-NaCl	Wolverine	W8	C	Z8	S	-8	-0.4	194.4	L+V	0.7	0.88
I	H_2O-NaCl	Wolverine	W8	C	Z9	S	-10.2	-0.2	201	L+V	0.4	0.87
I	H_2O-NaCl	Wolverine	W8	C	X5	L	-12	-2.6	341.1	L+V	4.3	0.68
I	H_2O-NaCl	Wolverine	W8	C	V3	S	-9	-0.3	191.1	L+V	0.5	0.88
I	H_2O-NaCl	Wolverine	W8	C	V5	S	-9	-0.3	180.6	L+V	0.5	0.89
I	H_2O-NaCl	Wolverine	W8	C	W6	S	-9	-1.3	186.6	L+V	2.2	0.90
I	H_2O-NaCl	Wolverine	W8	C	W7	S	-10	-1.3	213.9	L+V	2.2	0.87
I	H_2O-NaCl	Wolverine	W8	C	S6	S	-10.5	-1.5	190.9	L+V	2.6	0.90
I	H_2O-NaCl	Wolverine	W8	C	R6	S	-10.5	-1.5	199.6	L+V	2.6	0.89
I	H_2O-NaCl	Wolverine	W8	C	T9	S	-11	-1.1	188.7	L+V	1.9	0.89
I	H_2O-NaCl	Wolverine	W8	C	V9	S	-11.3	-1.1	207	L+V	1.9	0.87
I	H_2O-NaCl	Wolverine	W8	C	V11	S	-9	-1.7	225.5	L+V	2.9	0.86
I	H_2O-NaCl	Wolverine	W8	C	W11	S	-9	-1.7	218.8	L+V	2.9	0.86
I	H_2O-NaCl	Wolverine	W8	C	T14	S	-9	-1.5	231.3	L+V	2.6	0.84
I	H_2O-NaCl	Wolverine	W8	C	R16	L	-13	-2.1	300.7	L+V	3.5	0.74
I	H_2O-NaCl	Wolverine	W8	C	T20_1	S	-13	-2.4	273.3	L+V	4.0	0.80
I	H_2O-NaCl	Wolverine	W8	C	S19	S	-10.5	-1.4	187.7	L+V	2.4	0.90
I	H_2O-NaCl	Wolverine	W8	C	S20	S	-11	-1.4	182	L+V	2.4	0.91
I	H_2O-NaCl	Wolverine	W8	C	R23	S	-11.3	-0.5	221.4	L+V	0.9	0.84
I	H_2O-NaCl	Wolverine	W8	C	S23	S	-9	-0.4	253.4	L+V	0.7	0.79
I	H_2O-NaCl	Wolverine	W8	C	S24	S	-9	-0.4	248.7	L+V	0.7	0.80
I	H_2O-NaCl	Wolverine	W8	C	T23	S	-11	-2.2	196.6	L+V	3.7	0.90
I	H_2O-NaCl	Wolverine	W8	C	Y32	S	-10	-0.1	310	L+V	0.2	0.68
I	H_2O-NaCl	Wolverine	W8	C	X31	S	-10.5	-0.1	234.1	L+V	0.2	0.82
I	H_2O-NaCl	Wolverine	W8	C	Q24	S	-10.5	-0.8	312	L+V	1.4	0.69
I	H_2O-NaCl	Wolverine	W8	C	Q25	S	-11	-0.8	315	L+V	1.4	0.69
I	H_2O-NaCl	Wolverine	W8	C	P24	S	-11.3	-0.6	190	L+V	1.1	0.89
I	H_2O-NaCl	Wolverine	W8	C	N26	S	-9	-0.7	328.8	L+V	1.2	0.66
I	H_2O-NaCl	Wolverine	W8	C	L23	S	-9	-0.1	302.9	L+V	0.2	0.70
I	H_2O-NaCl	Wolverine	W8	C	L26	S	-9	-0.1	246	L+V	0.2	0.80

(Continued)

Type	Composition	Deposit	Sample	Grain	FI No.	Bubble size	T_{mi}	T_m	T_h	Phases	Salinity	ρ (g/cm^3)
I	H_2O-NaCl	Wolverine	W8	C	M26	S	-13	-0.1	198.7	L+V	0.2	0.87
I	H_2O-NaCl	Wolverine	W8	C	H26	S	-13	-1.7	196.2	L+V	2.9	0.89
I	H_2O-NaCl	Wolverine	W8	C	L18_1	S	-10	-1.3	341	L+V	2.2	0.65
I	H_2O-NaCl	Wolverine	W8	C	L18_2	S	-12	-1.3	325	L+V	2.2	0.68
I	H_2O-NaCl	Wolverine	W8	C	K19	S	-10	-0.2	185.5	L+V	0.4	0.89
I	H_2O-NaCl	Wolverine	W8	C	K20	S	-8	-0.2	181	L+V	0.4	0.89
I	H_2O-NaCl	Wolverine	W8	C	M21	S	-8	-0.5	275	L+V	0.9	0.76
I	H_2O-NaCl	Wolverine	W8	C	L16	S	-7	-0.1	192.9	L+V	0.2	0.88

I	H_2O-NaCl	Wolverine	W8	C	J20_1	S	-10	-1.3	180	L+V	2.2	0.91
I	H_2O-NaCl	Wolverine	W8	C	J20_2	S	-10.5	-2.5	246.6	L+V	4.2	0.84
I	H_2O-NaCl	Wolverine	W8	C	I20	S	-10.5	-2.6	195.3	L+V	4.3	0.90
I	H_2O-NaCl	Wolverine	W8	C	G20	S	-11	-2.6	196.1	L+V	4.3	0.90
I	H_2O-NaCl	Wolverine	W8	C	K29	S	-11.3	-1.5	230.7	L+V	2.6	0.85
I	H_2O-NaCl	Wolverine	W8	C	F12	S	-8	-0.1	194.4	L+V	0.2	0.88
I	H_2O-NaCl	Wolverine	W8	D	O13	S	-12	-2.1	202.7	L+V	3.5	0.89
I	H_2O-NaCl	Wolverine	W8	D	Q12	S	-14	-3.8	187.3	L+V	6.2	0.93
I	H_2O-NaCl	Wolverine	W8	D	R14_1	S	-7	-0.2	198	L+V	0.4	0.87
I	H_2O-NaCl	Wolverine	W8	D	R14_2	S	-7	-0.2	194.4	L+V	0.4	0.88
I	H_2O-NaCl	Wolverine	W8	D	S12	S	-6.5	-0.2	201.3	L+V	0.4	0.87
I	H_2O-NaCl	Wolverine	W8	D	P16	S	-6.5	-0.3	177.7	L+V	0.5	0.90
I	H_2O-NaCl	Wolverine	W8	D	S20	S	-6	-0.5	205.5	L+V	0.9	0.87
I	H_2O-NaCl	Wolverine	W8	D	O20	S	-10	-0.4	210.7	L+V	0.7	0.86
I	H_2O-NaCl	Wolverine	W8	D	J20	S	-10	-0.3	213.4	L+V	0.5	0.85
I	H_2O-NaCl	Wolverine	W8	D	R13_1	L	-10.5	-0.3	184	L+V	0.5	0.89
I	H_2O-NaCl	Wolverine	W8	D	R13_2	S	-10.5	-0.2	181	L+V	0.4	0.89
I	H_2O-NaCl	Wolverine	W8	D	R14_1	S	-11	-0.2	198	L+V	0.4	0.87
I	H_2O-NaCl	Wolverine	W8	D	R14_2	S	-11.8	-0.2	194.4	L+V	0.4	0.88
I	H_2O-NaCl	Wolverine	W8	D	P7	S	-9	-0.7	227.3	L+V	1.2	0.84
I	H_2O-NaCl	Wolverine	W8	D	Q8	S	-9	-0.7	218.3	L+V	1.2	0.85
I	H_2O-NaCl	Wolverine	W8	D	S7	L	-9	-2.3	240.4	L+V	3.9	0.84
I	H_2O-NaCl	Wolverine	W8	D	T10	L	-12	-0.8	197.7	L+V	1.4	0.88
I	H_2O-NaCl	Wolverine	W8	D	W9	S	-12.5	-0.7	210.2	L+V	1.2	0.86
I	H_2O-NaCl	Wolverine	W8	D	W12	S	-10	-1.1	225.5	L+V	1.9	0.85
I	H_2O-NaCl	Wolverine	W8	D	X12	S	-12	-0.9	183.7	L+V	1.6	0.90
I	H_2O-NaCl	Wolverine	W8	D	U27	S	-10	-0.9	203	L+V	1.6	0.87
I	H_2O-NaCl	Wolverine	W8	D	U28	S	-10.1	-1.8	250	L+V	3.1	0.82
I	H_2O-NaCl	Wolverine	W8	D	U29_1	S	-10.7	-1.1	244.1	L+V	1.9	0.82
I	H_2O-NaCl	Wolverine	W8	D	U29_2	S	-7	-1.1	210.7	L+V	1.9	0.87
I	H_2O-NaCl	Wolverine	W8	D	X28	S	-7	-0.8	198	L+V	1.4	0.88
I	H_2O-NaCl	Wolverine	W8	D	X29	S	-6.3	-0.8	201.1	L+V	1.4	0.88
I	H_2O-NaCl	Wolverine	W8	D	Q23	S	-6.3	-0.4	214.3	L+V	0.7	0.85
I	H_2O-NaCl	Wolverine	W8	D	Q24	S	-6	-0.4	219.9	L+V	0.7	0.85
I	H_2O-NaCl	Wolverine	W8	D	Q25	S	-10	-0.4	210.7	L+V	0.7	0.86
I	H_2O-NaCl	Wolverine	W8	D	T22	S	-10	-0.8	198	L+V	1.4	0.88
I	H_2O-NaCl	Wolverine	W8	D	V23	S	-9	-0.8	235.5	L+V	1.4	0.83
I	H_2O-NaCl	Wolverine	W8	D	AF38	L	-9	-1.4	350	L+V	2.4	0.63
I	H_2O-NaCl	Wolverine	W8	D	AK40	S	-13.1	-2.4	285.1	L+V	4.0	0.78
I	H_2O-NaCl	Wolverine	W8	D	AJ40	L	-13.2	-3.4	312	L+V	5.6	0.75
I	H_2O-NaCl	Wolverine	W8	D	AL27_2	S	-9	-1.2	267.2	L+V	2.1	0.79
I	H_2O-NaCl	Wolverine	W8	D	AK28	S	-11	-2.8	235.1	L+V	4.6	0.86
I	H_2O-NaCl	Wolverine	W8	D	AJ29_1	L	-13	-1.3	207.7	L+V	2.2	0.87
I	H_2O-NaCl	Wolverine	W8	D	AJ29_2	S	-12	-1.3	217.3	L+V	2.2	0.86
I	H_2O-NaCl	Wolverine	W8	D	AO21	S	-12.9	-1.9	340	L+V	3.2	0.66
I	H_2O-NaCl	Wolverine	W8	D	AP20	S	-6	-0.1	196.6	L+V	0.2	0.87
I	H_2O-NaCl	Wolverine	W8	D	AN21	S	-8.5	-0.4	176.8	L+V	0.7	0.90
I	H_2O-NaCl	Wolverine	W8	D	AN22	L	-10	-3.8	340	L+V	6.2	0.71
I	H_2O-NaCl	Wolverine	W8	D	AM12	L	-10.1	-1.1	188.8	L+V	1.9	0.89
I	H_2O-NaCl	Wolverine	W8	D	AI14	S	-10	-0.7	340	L+V	1.2	0.63
I	H_2O-NaCl	Wolverine	W8	D	AI15	L	-14	-1.3	277	L+V	2.2	0.77
I	H_2O-NaCl	Wolverine	W8	D	AJ16	L	-12	-2.3	311.3	L+V	3.9	0.73
I	H_2O-NaCl	Wolverine	W8	D	AG15	S	-9	-1.7	340	L+V	2.9	0.66
I	H_2O-NaCl	Wolverine	W8	D	AH16_2	S	-9	-1.3	193	L+V	2.2	0.89
I	H_2O-NaCl	Wolverine	W8	D	AG19_1	S	-13.1	-1.4	350	L+V	2.4	0.63
I	H_2O-NaCl	Wolverine	W8	D	AH20	S	-13	-1.1	210.2	L+V	1.9	0.87
I	H_2O-NaCl	Wolverine	W8	D	AI20	S	-9	-1.1	205.5	L+V	1.9	0.87
I	H_2O-NaCl	Wolverine	W8	D	AD20	S	-11	-1.8	225.6	L+V	3.1	0.86
I	H_2O-NaCl	Wolverine	W8	D	AF21	S	-13	-1.8	178.9	L+V	3.1	0.91
I	H_2O-NaCl	Wolverine	W8	D	AD29	S	-12	-0.2	170	L+V	0.4	0.90
I	H_2O-NaCl	Wolverine	W8	D	AA17	S	-11.1	-1.6	277.4	L+V	2.7	0.78
I	H_2O-NaCl	Wolverine	W8	D	AA19_1	S	-8	-0.7	281.1	L+V	1.2	0.75
I	H_2O-NaCl	Wolverine	W8	D	AA19_2	S	-8.5	-1.5	248	L+V	2.6	0.82
I	H_2O-NaCl	Wolverine	W8	D	Z17	S	-11	-1.6	267.7	L+V	2.7	0.79
I	H_2O-NaCl	Wolverine	W8	D	AB20_1	S	-10.1	-1.5	281	L+V	2.6	0.77
I	H_2O-NaCl	Wolverine	W8	D	AB20_2	S	-10	-1.5	278	L+V	2.6	0.77
I	H_2O-NaCl	Wolverine	W8	D	AB21	S	-12	-1.5	265	L+V	2.6	0.79
I	H_2O-NaCl	Wolverine	W8	D	Z21_2	S	-13	-0.8	335	L+V	1.4	0.65

(Continued)

Type	Composition	Deposit	Sample	Grain	FI No.	Bubble size	T_{mi}	T_m	T_h	Phases	Salinity	ρ (g/cm^3)
I	H_2O-NaCl	Area 5	A2-14	A	Q18	S	-10	-1.8	219.1	L+V	3.1	0.87
I	H_2O-NaCl	Area 5	A2-14	A	Q17	S	-11.7	-1.5	210.3	L+V	2.6	0.87
I	H_2O-NaCl	Area 5	A2-14	A	P17	S	-14.7	-1.3	199.7	L+V	2.2	0.88
I	H_2O-NaCl	Area 5	A2-14	A	R19	S	-15	-1.6	250	L+V	2.7	0.82
I	H_2O-NaCl	Area 5	A2-14	A	S19	S	-11.3	-1.3	219.1	L+V	2.2	0.86
I	H_2O-NaCl	Area 5	A2-14	A	R14	S	-9.7	-1.1	169.3	L+V	1.9	0.92
I	H_2O-NaCl	Area 5	A2-14	A	U15_1	S	-14.4	-1.6	174.1	L+V	2.7	0.92

I	H_2O-NaCl	Area 5	A2-14	A	V16	S	-15.5	-1.6	190.5	L+V	2.7	0.90
I	H_2O-NaCl	Area 5	A2-14	A	K32	S	-9.9	-1.3	139.8	L+V	2.2	0.95
I	H_2O-NaCl	Area 5	A2-14	A	M17	S	-10.1	-1.2	205.3	L+V	2.1	0.88
I	H_2O-NaCl	Area 5	A2-14	B	X14	L	-16.6	-2.4	230	L+V	4.0	0.86
I	H_2O-NaCl	Area 5	A2-14	B	W12	S	-16.6	-2.4	192.1	L+V	4.0	0.91
I	H_2O-NaCl	Area 5	A2-14	B	W11	S	-14.5	-1.5	164.5	L+V	2.6	0.92
I	H_2O-NaCl	Area 5	A2-14	B	U10	S	-14.4	-1.5	146.6	L+V	2.6	0.94
I	H_2O-NaCl	Area 5	A2-14	B	V11	S	-14.7	-1.5	115.5	L+V	2.6	0.97
I	H_2O-NaCl	Area 5	A2-14	B	Y13	S	-14.4	-2.8	250	L+V	4.6	0.84
I	H_2O-NaCl	Area 5	A2-14	B	AF11	L	-7.1	-0.3	205	L+V	0.5	0.86
I	H_2O-NaCl	Area 5	A2-14	B	W7_1	L	-9.3	-1.6	242.4	L+V	2.7	0.83
I	H_2O-NaCl	Area 5	A2-14	B	W7_2	S	-5.5	-0.3	99.1	L+V	0.5	0.97
I	H_2O-NaCl	Area 5	A2-14	B	Z10_2	S	-5.2	-0.3	128.3	L+V	0.5	0.94
I	H_2O-NaCl	Area 5	A2-14	B	AA8	S	-14.4	-4.6	185.4	L+V	7.3	0.94
I	H_2O-NaCl	Area 5	A2-14	B	AA10	S	-4.4	-0.1	185	L+V	0.2	0.89
I	H_2O-NaCl	Area 5	A2-14	B	Y9	L	-4.5	-0.1	247	L+V	0.2	0.80
I	H_2O-NaCl	Area 5	A2-14	B	U6	S	-4.8	-0.1	120.7	L+V	0.2	0.95
I	H_2O-NaCl	Area 5	A2-14	B	V8	S	-12.2	-1.7	152.4	L+V	2.9	0.94
I	H_2O-NaCl	Area 5	A2-14	B	U23	L	-6.6	-0.5	269.5	L+V	0.9	0.77
I	H_2O-NaCl	Area 5	A2-14	B	V22	S	-5.7	-0.3	250	L+V	0.5	0.80
I	H_2O-NaCl	Area 5	A2-14	B	U13	L	-8.1	-0.2	255	L+V	0.4	0.79
I	H_2O-NaCl	Area 5	A2-14	B	V15	L	-8.1	-0.2	250	L+V	0.4	0.80
I	H_2O-NaCl	Area 5	A2-14	B	U14	L	-8.1	-0.2	250	L+V	0.4	0.80
I	H_2O-NaCl	Area 5	A2-14	B	V12	S	-5.6	-0.1	250	L+V	0.2	0.79
I	H_2O-NaCl	Area 5	A2-14	B	Q8	S	-9.9	-0.1	222.2	L+V	0.2	0.84
I	H_2O-NaCl	Area 5	A2-14	B	O7	S	-11.4	-1.5	155.5	L+V	2.6	0.93
I	H_2O-NaCl	Area 5	A2-14	C	I7	S	-14.5	-4.1	171.4	L+V	6.6	0.95
I	H_2O-NaCl	Area 5	A2-14	C	H7	S	-15.5	-5.3	182.7	L+V	8.3	0.95
I	H_2O-NaCl	Area 5	A2-14	C	G14	L	-14.9	-4.4	208.3	L+V	7.0	0.91
I	H_2O-NaCl	Area 5	A2-14	C	I19	L	-14.1	-4.6	178.7	L+V	7.3	0.94
I	H_2O-NaCl	Area 5	A2-14	C	I17	S	-17	-4.6	220	L+V	7.3	0.90
I	H_2O-NaCl	Area 5	A2-14	C	J24	L	-7.1	-0.1	221.9	L+V	0.2	0.84
I	H_2O-NaCl	Area 5	A2-14	C	J22	S	-16.6	-2.9	151.9	L+V	4.8	0.95
I	H_2O-NaCl	Area 5	A2-14	C	P17	L	-10	-1.1	206.8	L+V	1.9	0.87
I	H_2O-NaCl	Area 5	A2-14	C	M19	S	-7	-0.1	243.9	L+V	0.2	0.80
I	H_2O-NaCl	Area 5	A2-14	C	G28	S	-16.6	-4.8	157.8	L+V	7.6	0.97
I	H_2O-NaCl	Area 5	A2-14	C	G17	L	-17.1	-5.8	239.1	L+V	8.9	0.89
I	H_2O-NaCl	Area 5	A2-14	C	E19	S	-17.1	-6.5	242.2	L+V	9.9	0.89
I	H_2O-NaCl	Area 5	A2-14	C	G20	S	-14.9	-2.4	128.6	L+V	4.0	0.97
I	H_2O-NaCl	Area 5	A2-14	C	H23	S	-9	-0.1	236.9	L+V	0.2	0.82
I	H_2O-NaCl	Area 5	A2-14	C	I24	S	-9	-0.1	236.9	L+V	0.2	0.82
I	H_2O-NaCl	Area 5	A2-14	D	T9_1	S	-16	-6.5	236.6	L+V	9.9	0.90
I	H_2O-NaCl	Area 5	A2-14	D	J33	S	-6.1	-0.1	123	L+V	0.2	0.95
I	H_2O-NaCl	Area 5	A2-14	D	K32	S	-6.2	-0.1	123	L+V	0.2	0.95
I	H_2O-NaCl	Area 5	A2-14	E	J13	S	-9.7	-0.6	231.8	L+V	1.1	0.83
I	H_2O-NaCl	Area 5	A2-14	E	J14	L	-9.7	-0.7	231.9	L+V	1.2	0.83
I	H_2O-NaCl	Area 5	A2-14	E	J15_1	S	-9.7	-0.7	250	L+V	1.2	0.80
I	H_2O-NaCl	Area 5	A2-14	E	J15_2	S	-6	-0.5	241.7	L+V	0.9	0.81
I	H_2O-NaCl	Area 5	A2-14	E	K13	L	-12.2	-1.2	250	L+V	2.1	0.81
I	H_2O-NaCl	Area 5	A2-14	E	K14	S	-6	-0.8	261.9	L+V	1.4	0.79
I	H_2O-NaCl	Area 5	A2-14	E	I14	S	-7	-0.2	220	L+V	0.4	0.84
I	H_2O-NaCl	Area 5	A2-14	E	I18	S	-7.1	-0.6	239.1	L+V	1.1	0.82
I	H_2O-NaCl	Area 5	A2-14	E	G19	S	-8.2	-0.1	179.8	L+V	0.2	0.89
I	H_2O-NaCl	Area 5	A2-14	E	G20	S	-8	-0.2	262.7	L+V	0.4	0.77
I	H_2O-NaCl	Area 5	A2-14	E	H24	L	-7.5	-0.5	250	L+V	0.9	0.80
I	H_2O-NaCl	Area 5	A2-14	E	I24	S	-5.2	-0.1	264.6	L+V	0.2	0.77
I	H_2O-NaCl	Area 5	A2-14	E	I25	S	-15	-4.5	166.6	L+V	7.2	0.95
I	H_2O-NaCl	Area 5	A2-14	E	L25_1	L	-8	-0.1	205.9	L+V	0.2	0.86
I	H_2O-NaCl	Area 5	A2-14	E	L25_2	S	-9	-0.7	264.6	L+V	1.2	0.78
I	H_2O-NaCl	Area 5	A2-14	E	L25_3	S	-11.1	-1.1	264.1	L+V	1.9	0.79
I	H_2O-NaCl	Area 5	A2-14	E	L23	L	-17.7	-2.5	245	L+V	4.2	0.84
I	H_2O-NaCl	Area 5	A2-14	E	K23	S	-14	-0.9	196.7	L+V	1.6	0.88
I	H_2O-NaCl	Area 5	A2-14	E	L24_1	S	-13.3	-0.8	232	L+V	1.4	0.83
I	H_2O-NaCl	Area 5	A2-14	E	L24_2	S	-12	-0.1	249.9	L+V	0.2	0.79
I	H_2O-NaCl	Area 5	A2-14	E	K25	S	-11.9	-0.8	230.8	L+V	1.4	0.84
I	H_2O-NaCl	Area 5	A2-14	E	M26	S	-14.4	-1.6	224.3	L+V	2.7	0.86
I	H_2O-NaCl	Area 5	A2-14	E	M27	S	-13	-1.2	268.1	L+V	2.1	0.78
I	H_2O-NaCl	Area 5	A2-14	E	L22	L	-13	-1.1	225	L+V	1.9	0.85

(Continued)

Type	Composition	Deposit	Sample	Grain	FI No.	Bubble size	T_{mi}	T_m	T_h	Phases	Salinity	ρ (g/cm^3)
I	H_2O-NaCl	Area 5	A2-14	E	K20	S	-9	-0.4	209.4	L+V	0.7	0.86
I	H_2O-NaCl	Area 5	A2-14	E	P27_1	S	-16.7	-3.5	241.1	L+V	5.7	0.86
I	H_2O-NaCl	Area 5	A2-14	E	Q27	S	-16	-3.1	169.9	L+V	5.1	0.94
I	H_2O-NaCl	Area 5	A2-14	E	Q26	S	-16	-3.1	172.2	L+V	5.1	0.93
I	H_2O-NaCl	Area 5	A2-14	E	S23	S	-7.7	-0.1	170.1	L+V	0.2	0.90
I	H_2O-NaCl	Area 5	A2-14	E	S20_1	S	-10	-0.2	247.3	L+V	0.4	0.80
I	H_2O-NaCl	Area 5	A2-14	E	S20_2	S	-10	-0.1	216.6	L+V	0.2	0.85

I	H_2O-NaCl	Area 5	A2-14	E	S20_3	S	-10	-0.1	234.1	L+V	0.2	0.82
I	H_2O-NaCl	Area 5	A2-14	E	R17	S	-10	-0.1	162.2	L+V	0.2	0.91
I	H_2O-NaCl	Area 5	A2-14	E	T16	S	-10	-0.1	255	L+V	0.2	0.79
I	H_2O-NaCl	Area 5	A2-14	E	R16	L	-12	-0.5	174.4	L+V	0.9	0.90
I	H_2O-NaCl	Area 5	A2-14	E	R15	S	-12	-0.5	174.5	L+V	0.9	0.90
I	H_2O-NaCl	Area 5	A2-14	E	S13_2	S	-17	-3.1	155.4	L+V	5.1	0.95
I	H_2O-NaCl	Area 5	A2-14	E	Q14_2	S	-11	-0.1	257.2	L+V	0.2	0.78
I	H_2O-NaCl	Area 5	A2-14	E	S11	S	-12	-0.6	182.5	L+V	1.1	0.90
I	H_2O-NaCl	Area 5	A2-14	E	O17	S	-11	-0.1	210	L+V	0.2	0.85
I	H_2O-NaCl	Area 5	A2-14	G	I11	S	-11	-0.1	158	L+V	0.2	0.92
I	H_2O-NaCl	Area 5	A2-14	G	L13	L	-11.3	-0.3	220	L+V	0.5	0.84
I	H_2O-NaCl	Area 5	A2-14	G	N10	L	-12.2	-1.9	149.6	L+V	3.2	0.94
I	H_2O-NaCl	Area 5	A2-14	G	K12	L	-17	-6.1	188.2	L+V	9.3	0.95
I	H_2O-NaCl	Area 5	A2-14	G	L12_1	S	-16.1	-6.1	133.6	L+V	9.3	1.00
I	H_2O-NaCl	Area 5	A2-14	G	O14	S	-15.9	-2.7	215	L+V	4.5	0.88
I	H_2O-NaCl	Area 5	A2-14	G	S20	L	-6	-0.6	215	L+V	1.1	0.85
I	H_2O-NaCl	Area 5	A2-14	G	R31_1	S	-10	-1.1	119.9	L+V	1.9	0.96
I	H_2O-NaCl	Area 5	A2-14	G	R31_2	S	-10	-1.1	148.7	L+V	1.9	0.94
I	H_2O-NaCl	Area 5	A2-14	G	P32_1	S	-13.3	-1.8	204.9	L+V	3.1	0.88
I	H_2O-NaCl	Area 5	A2-14	G	P32_2	S	-13.3	-1.8	205	L+V	3.1	0.88
I	H_2O-NaCl	Area 5	A2-14	G	P33	L	-8	-0.5	210.6	L+V	0.9	0.86
I	H_2O-NaCl	Area 5	A2-14	H	R13	S	-7.7	-0.5	215.2	L+V	0.9	0.85
I	H_2O-NaCl	Area 5	A2-14	H	Q6	S	-11	-1.5	213	L+V	2.6	0.87
I	H_2O-NaCl	Area 5	A2-14	H	M23	S	-9	-0.4	210	L+V	0.7	0.86
I	H_2O-NaCl	Area 5	A2-14	H	M22	S	-10	-0.6	198.6	L+V	1.1	0.88
I	H_2O-NaCl	Area 5	A2-14	H	N22	L	-10.1	-0.8	220	L+V	1.4	0.85
I	H_2O-NaCl	Area 5	A2-14	H	P22	S	-17.7	-6.2	241.1	L+V	9.5	0.89
I	H_2O-NaCl	Area 5	A2-14	H	S22_1	S	-13.3	-1.5	159.5	L+V	2.6	0.93
I	H_2O-NaCl	Area 5	A2-14	H	T24_2	S	-13.3	-1.5	149.9	L+V	2.6	0.94
I	H_2O-NaCl	Area 5	A2-14	H	V17	S	-19	-5.2	156.2	L+V	8.1	0.97
I	H_2O-NaCl	Area 5	A2-14	I	I16	L	-9	-0.3	214.6	L+V	0.5	0.85
I	H_2O-NaCl	Area 5	A2-14	I	J16	S	-9	-0.3	210	L+V	0.5	0.86
I	H_2O-NaCl	Area 5	A2-14	I	K18	S	-9	-0.2	152.7	L+V	0.4	0.92
I	H_2O-NaCl	Area 5	A2-14	I	L15	S	-12.2	-1.2	232.7	L+V	2.1	0.84
I	H_2O-NaCl	Area 5	A2-14	I	K15_2	S	-9	-0.8	171.5	L+V	1.4	0.91
I	H_2O-NaCl	Area 5	A2-14	I	L16_1	S	-9	-0.4	220	L+V	0.7	0.85
I	H_2O-NaCl	Area 5	A2-14	I	K13	S	-16.6	-3.6	157.4	L+V	5.9	0.95
I	H_2O-NaCl	Area 5	A2-14	I	N17	S	-10	-0.4	220	L+V	0.7	0.85
I	H_2O-NaCl	Area 5	A2-14	I	Q17	S	-12.5	-2.5	188.2	L+V	4.2	0.91
I	H_2O-NaCl	Area 5	A2-14	I	T20	S	-7	-0.3	258.6	L+V	0.5	0.78
I	H_2O-NaCl	Area 5	A2-14	I	L13	S	-7	-0.1	169.4	L+V	0.2	0.90
I	H_2O-NaCl	Area 5	A2-14	I	L11	S	-14.4	-2.5	140.5	L+V	4.2	0.96
I	H_2O-NaCl	Area 5	A2-14	I	I13	L	-8	-0.2	272.3	L+V	0.4	0.76
I	H_2O-NaCl	Area 5	A2-14	I	J11_1	S	-8	-0.2	202.4	L+V	0.4	0.87
I	H_2O-NaCl	Area 5	A2-14	I	J11_2	S	-8	-0.2	228.7	L+V	0.4	0.83
I	H_2O-NaCl	Area 5	A2-14	I	J11_3	S	-8	-0.2	216.2	L+V	0.4	0.85
I	H_2O-NaCl	Area 5	A2-14	I	J10	S	-7.5	-0.1	207.1	L+V	0.2	0.86
I	H_2O-NaCl	Area 5	A2-14	I	K9_1	S	-7.5	-0.1	173	L+V	0.2	0.90
I	H_2O-NaCl	Area 5	A2-14	I	O1	L	-8	-0.2	192.4	L+V	0.4	0.88
I	H_2O-NaCl	Area 5	A2-14	I	O2	L	-9.1	-0.3	218.1	L+V	0.5	0.85
I	H_2O-NaCl	Area 5	A2-14	I	P2	L	-10.1	-0.4	198.7	L+V	0.7	0.87
I	H_2O-NaCl	Area 5	A2-14	I	P1	S	-7.7	-0.1	209.9	L+V	0.2	0.85
II	H_2O-NaCl	Area 5	A2-14	A	X7	S	-15	-9.8	166.5	L+V	13.7	1.00
II	H_2O-NaCl	Area 5	A2-14	A	O29	S	-16	-10.1	155.6	L+V	14.0	1.01
II	H_2O-NaCl	Area 5	A2-14	E	N23	S	-17	-12.1	198.1	L+V	16.1	0.99
II	H_2O-NaCl	Area 5	A2-14	G	I8	S	-16.6	-12.1	220.2	L+V	16.1	0.97
II	H_2O-NaCl	Area 5	A2-14	G	J24_1	S	-16.7	-12.9	156.9	L+V	16.8	1.03
II	H_2O-NaCl	Area 5	A2-14	H	F11	S	-16	-14.4	200.1	L+V	18.1	1.01
II	H_2O-NaCl	Area 5	A2-14	H	G10	S	-16	-14.4	215.5	L+V	18.1	0.99
II	H_2O-NaCl	Area 5	A2-14	H	G11	S	-16	-14.4	213.3	L+V	18.1	0.99
II	H_2O-NaCl	Area 5	A2-14	I	Q16	S	-21	-9.3	222.2	L+V	13.2	0.94
III	H_2O-$CaCl_2$-NaCl	Area 5	A2-14	A	P9	S	-40	-17.8	180	L+V	19.6	1.05
III	H_2O-$CaCl_2$-NaCl	Area 5	A2-14	A	Q27	S	-50.1	-24.8	124.5	L+V	22.9	1.13
III	H_2O-$CaCl_2$-NaCl	Area 5	A2-14	A	N29	S	-50.3	-23.6	155	L+V	22.4	1.10
III	H_2O-$CaCl_2$-NaCl	Area 5	A2-14	A	W8	S	-37	-17.9	129.1	L+V	20.9	1.09
III	H_2O-$CaCl_2$-NaCl	Area 5	A2-14	A	W10	S	-33	-19.7	144	L+V	22.2	1.09
III	H_2O-$CaCl_2$-NaCl	Area 5	A2-14	A	O7	S	-35	-19.7	102.7	L+V	22.2	1.12
III	H_2O-$CaCl_2$-NaCl	Area 5	A2-14	B	W10	L	-48.7	-23.1	149.1	L+V	22.2	1.10

(Continued)

Type	Composition	Deposit	Sample	Grain	FI No.	Bubble size	T_{mi}	T_m	T_h	Phases	Salinity	ρ (g/cm^3)
III	H_2O-$CaCl_2$-NaCl	Area 5	A2-14	B	X11	S	-47.1	-23.2	171.5	L+V	22.2	1.08
III	H_2O-$CaCl_2$-NaCl	Area 5	A2-14	B	Y15	L	-45	-22.6	210.7	L+V	22.0	1.05
III	H_2O-$CaCl_2$-NaCl	Area 5	A2-14	B	Z15	L	-49.7	-24.1	146.6	L+V	22.6	1.11
III	H_2O-$CaCl_2$-NaCl	Area 5	A2-14	B	Y18	L	-51.1	-24.1	134.4	L+V	22.6	1.12
III	H_2O-$CaCl_2$-NaCl	Area 5	A2-14	B	X17	L	-50.6	-24.1	130.9	L+V	22.6	1.12
III	H_2O-$CaCl_2$-NaCl	Area 5	A2-14	B	Z10_1	S	-50	-25.2	181.1	L+V	23.1	1.09
III	H_2O-$CaCl_2$-NaCl	Area 5	A2-14	B	Z11	S	-47.7	-21.3	177.7	L+V	21.3	1.07

III	H_2O-$CaCl_2$-NaCl	Area 5	A2-14	B	AF19	L	-30.9	-2.7	187.8	L+V	5.1	0.91
III	H_2O-$CaCl_2$-NaCl	Area 5	A2-14	B	X20	S	-43.8	-21.1	145.5	L+V	21.3	1.09
III	H_2O-$CaCl_2$-NaCl	Area 5	A2-14	B	R8	S	-23.3	-0.8	168.8	L+V	1.4	0.91
III	H_2O-$CaCl_2$-NaCl	Area 5	A2-14	B	W6	S	-42	-20.8	120.7	L+V	22.9	1.11
III	H_2O-$CaCl_2$-NaCl	Area 5	A2-14	C	N17	S	-37.7	-7.6	201	L+V	11.8	0.95
III	H_2O-$CaCl_2$-NaCl	Area 5	A2-14	E	R18	S	-49.1	-24.3	177.7	L+V	22.7	1.08
III	H_2O-$CaCl_2$-NaCl	Area 5	A2-14	E	T12	S	-24.4	-0.5	159.8	L+V	0.9	0.92
III	H_2O-$CaCl_2$-NaCl	Area 5	A2-14	E	J25	S	-31	-16.1	211.5	L+V	19.5	1.01
III	H_2O-$CaCl_2$-NaCl	Area 5	A2-14	G	K14_1	S	-46.6	-24.2	125.2	L+V	22.7	1.13
III	H_2O-$CaCl_2$-NaCl	Area 5	A2-14	G	K14_2	S	-49.1	-23.2	120.5	L+V+S	22.2	1.12
III	H_2O-$CaCl_2$-NaCl	Area 5	A2-14	G	L12_2	L	-38.8	-6.9	241.2	L+V	11.0	0.90
III	H_2O-$CaCl_2$-NaCl	Area 5	A2-14	G	K13	S	-41.1	-14.8	128.2	L+V	17.8	1.07
III	H_2O-$CaCl_2$-NaCl	Area 5	A2-14	G	L20_1	L	-49.9	-24.5	174	L+V	22.8	1.09
III	H_2O-$CaCl_2$-NaCl	Area 5	A2-14	G	L20_2	S	-50.5	-24.6	115.1	L+V	22.8	1.13
III	H_2O-$CaCl_2$-NaCl	Area 5	A2-14	G	K22	S	-29.3	-9.2	185	L+V	13.3	0.98
III	H_2O-$CaCl_2$-NaCl	Area 5	A2-14	G	O12_1	S	-50.1	-24.1	178.5	L+V	22.6	1.08
III	H_2O-$CaCl_2$-NaCl	Area 5	A2-14	G	P21_2	S	-36.5	-11.6	124.2	L+V	15.5	1.05
III	H_2O-$CaCl_2$-NaCl	Area 5	A2-14	G	N25	S	-27.7	-7.2	210	L+V	11.2	0.94
III	H_2O-$CaCl_2$-NaCl	Area 5	A2-14	G	L41	S	-44.4	-21.2	158	L+V	21.3	1.08
III	H_2O-$CaCl_2$-NaCl	Area 5	A2-14	G	O34	S	-25.5	-3.5	130.9	L+V	6.2	0.98
III	H_2O-$CaCl_2$-NaCl	Area 5	A2-14	G	O33	S	-43.7	-20.8	134.6	L+V	21.1	1.10
III	H_2O-$CaCl_2$-NaCl	Area 5	A2-14	H	F13_2	S	-46.9	-22.5	142.4	L+V	21.9	1.10
III	H_2O-$CaCl_2$-NaCl	Area 5	A2-14	H	T15_1	L	-50.5	-24.7	135.3	L+V	22.9	1.12
III	H_2O-$CaCl_2$-NaCl	Area 5	A2-14	H	T15_2	L	-51.3	-25.8	119.5	L+V	23.3	1.14
III	H_2O-$CaCl_2$-NaCl	Area 5	A2-14	H	T15_3	S	-48.8	-25.1	153.6	L+V	23.1	1.11
III	H_2O-$CaCl_2$-NaCl	Area 5	A2-14	H	P17_3	S	-29.7	-2.5	144.9	L+V	4.8	0.95
III	H_2O-$CaCl_2$-NaCl	Area 5	A2-14	H	N19	S	-26.6	-0.6	123.7	L+V	1.2	0.95
III	H_2O-$CaCl_2$-NaCl	Area 5	A2-14	H	N13	S	-50	-25.2	150.1	L+V	23.1	1.11
III	H_2O-$CaCl_2$-NaCl	Area 5	A2-14	H	J26	S	-28.8	-3.2	149.9	L+V	5.8	0.96
III	H_2O-$CaCl_2$-NaCl	Area 5	A2-14	H	K26	S	-24.4	-2.5	112.7	L+V	4.5	0.98
III	H_2O-$CaCl_2$-NaCl	Area 5	A2-14	H	N21	L	-22.9	-0.5	155	L+V	0.7	0.92
III	H_2O-$CaCl_2$-NaCl	Area 5	A2-14	H	N15_1	S	-31	-18.2	164.5	L+V	21.1	1.06
III	H_2O-$CaCl_2$-NaCl	Area 5	A2-14	I	K16	S	-44.4	-23.5	143.2	L+V	22.4	1.11
III	H_2O-$CaCl_2$-NaCl	Area 5	A2-14	I	L16_2	L	-49.5	-24.6	207.7	L+V	22.8	1.06
III	H_2O-$CaCl_2$-NaCl	Area 5	A2-14	I	K7	S	-23.1	-0.6	173.1	L+V+S	1.0	0.91
I	H_2O-NaCl	Wolverine	W7-3	A	P20	L	-15.5	-3.4	210	L+V	5.6	0.90
I	H_2O-NaCl	Wolverine	W7-3	A	Q27	L	-16.7	-4.1	203.5	L+V	6.6	0.91
I	H_2O-NaCl	Wolverine	W7-3	A	S25_1	L	-11	-1.1	257	L+V	1.9	0.80
I	H_2O-NaCl	Wolverine	W7-3	A	S25_2	S	-16.6	-4.6	207.1	L+V	7.3	0.91
I	H_2O-NaCl	Wolverine	W7-3	A	U24	L	-16	-4.1	215	L+V	6.6	0.90
I	H_2O-NaCl	Wolverine	W7-3	A	T26	L	-6	-0.1	215	L+V	0.2	0.85
I	H_2O-NaCl	Wolverine	W7-3	A	Y23	L	-14.4	-2.8	220	L+V	4.6	0.88
I	H_2O-NaCl	Wolverine	W7-3	A	U45	S	-7	-0.3	135	L+V	0.5	0.94
I	H_2O-NaCl	Wolverine	W7-3	A	U51_1	S	-15	-5.6	144.5	L+V	8.7	0.98
I	H_2O-NaCl	Wolverine	W7-3	A	S47	S	-7	-0.8	224.3	L+V	1.4	0.84
I	H_2O-NaCl	Wolverine	W7-3	A	O35	L	-14.1	-6.4	210.7	L+V	9.7	0.93
I	H_2O-NaCl	Wolverine	W7-3	A	O37	L	-8	-0.1	175.7	L+V	0.2	0.90
I	H_2O-NaCl	Wolverine	W7-3	A	O39	L	-8	-0.1	180.1	L+V	0.2	0.89
I	H_2O-NaCl	Wolverine	W7-3	A	P62	L	-11.1	-1.3	210.1	L+V	2.2	0.87
I	H_2O-NaCl	Wolverine	W7-3	A	O63	S	-13.7	-6.1	194.4	L+V	9.3	0.94
I	H_2O-NaCl	Wolverine	W7-3	A	Y50	S	-8	-0.1	220.1	L+V	0.2	0.84
I	H_2O-NaCl	Wolverine	W7-3	B	W4	S	-8	-0.1	141.9	L+V	0.2	0.93
I	H_2O-NaCl	Wolverine	W7-3	B	M22_1	S	-8	-0.1	144.2	L+V	0.2	0.93
I	H_2O-NaCl	Wolverine	W7-3	B	M22_2	S	-8	-0.1	178.8	L+V	0.2	0.89
I	H_2O-NaCl	Wolverine	W7-3	B	M23	S	-8	-0.1	145.1	L+V	0.2	0.93
I	H_2O-NaCl	Wolverine	W7-3	B	P26_1	L	-17.7	-3.4	178.8	L+V	5.6	0.93
I	H_2O-NaCl	Wolverine	W7-3	B	P26_2	S	-8	-0.1	142.4	L+V	0.2	0.93
I	H_2O-NaCl	Wolverine	W7-3	B	P24	S	-13	-2.1	224.7	L+V	3.5	0.86
I	H_2O-NaCl	Wolverine	W7-3	B	T19	S	-13	-4.5	148.2	L+V	7.2	0.97
I	H_2O-NaCl	Wolverine	W7-3	B	O35	S	-13	-2.1	228.7	L+V	3.5	0.86
I	H_2O-NaCl	Wolverine	W7-3	D	J18	S	-11.1	-1.1	138.8	L+V	1.9	0.94
I	H_2O-NaCl	Wolverine	W7-3	D	I23	S	-7	-0.2	250.1	L+V	0.4	0.80
I	H_2O-NaCl	Wolverine	W7-3	D	H22_1	S	-7	-0.1	130.7	L+V	0.2	0.94
I	H_2O-NaCl	Wolverine	W7-3	D	H23_2	S	-7	-2.1	137.3	L+V	3.5	0.96
I	H_2O-NaCl	Wolverine	W7-3	D	H24_1	S	-8	-0.1	125.6	L+V	0.2	0.94
I	H_2O-NaCl	Wolverine	W7-3	D	H24_2	S	-8	-0.1	141.1	L+V	0.2	0.93
I	H_2O-NaCl	Wolverine	W7-3	D	G25_1	S	-8	-0.2	150.7	L+V	0.4	0.92
I	H_2O-NaCl	Wolverine	W7-3	D	E19	S	-8	-0.1	165.6	L+V	0.2	0.91

(Continued)

Type	Composition	Deposit	Sample	Grain	FI No.	Bubble size	T_{mi}	T_m	T_h	Phases	Salinity	ρ (g/cm^3)
I	H_2O-NaCl	Wolverine	W7-3	D	F19	S	-7	-0.1	142.2	L+V	0.2	0.93
I	H_2O-NaCl	Wolverine	W7-3	E	L8_1	L	-16.5	-3.5	224.7	L+V	5.7	0.88
I	H_2O-NaCl	Wolverine	W7-3	E	L9	S	-7	-0.1	180.6	L+V	0.2	0.89
I	H_2O-NaCl	Wolverine	W7-3	E	M4	L	-12.1	-1.2	146.8	L+V	2.1	0.94
I	H_2O-NaCl	Wolverine	W7-3	E	M6	S	-9	-0.1	152.2	L+V	0.2	0.92
I	H_2O-NaCl	Wolverine	W7-3	E	J10	S	-9	-0.2	120.9	L+V	0.4	0.95
I	H_2O-NaCl	Wolverine	W7-3	E	E8	S	-9	-0.1	212.7	L+V	0.2	0.85

I	H_2O-NaCl	Wolverine	W7-3	F	P41	L	-15.5	-4.4	221.9	L+V	7.0	0.89
I	H_2O-NaCl	Wolverine	W7-3	F	I27_2	S	-8.5	-0.2	131.9	L+V	0.4	0.94
I	H_2O-NaCl	Wolverine	W7-3	F	N23	S	-13	-5.5	160.8	L+V	8.5	0.97
I	H_2O-NaCl	Wolverine	W7-3	F	R18	L	-13.3	-1.8	215	L+V	3.1	0.87
I	H_2O-NaCl	Wolverine	W7-3	F	S17_1	L	-11	-1.5	210	L+V	2.6	0.87
I	H_2O-NaCl	Wolverine	W7-3	F	S17_2	L	-11	-1.1	220	L+V	1.9	0.85
I	H_2O-NaCl	Wolverine	W7-3	F	S17_3	L	-11	-1.2	215	L+V	2.1	0.86
I	H_2O-NaCl	Wolverine	W7-3	F	S17_4	L	-11	-1.7	215	L+V	2.9	0.87
I	H_2O-NaCl	Wolverine	W7-3	F	T17	L	-14.5	-2.1	210	L+V	3.5	0.88
I	H_2O-NaCl	Wolverine	W7-3	F	T16	L	-14.5	-2.7	215	L+V	4.5	0.88
I	H_2O-NaCl	Wolverine	W7-3	F	U16	L	-13.1	-6.2	157.5	L+V	9.5	0.98
I	H_2O-NaCl	Wolverine	W7-3	F	U17	L	-12.5	-2.5	210	L+V	4.2	0.89
I	H_2O-NaCl	Wolverine	W7-3	F	W15_1	S	-10	-0.5	204.8	L+V	0.9	0.87
I	H_2O-NaCl	Wolverine	W7-3	F	W15_2	S	-10	-0.5	241.7	L+V	0.9	0.81
I	H_2O-NaCl	Wolverine	W7-3	F	X16	S	-9	-0.2	225	L+V	0.4	0.84
I	H_2O-NaCl	Wolverine	W7-3	F	AC12	S	-16	-4.4	225.5	L+V	7.0	0.89
I	H_2O-NaCl	Wolverine	W7-3	F	AB12	L	-7	-0.1	170.7	L+V	0.2	0.90
I	H_2O-NaCl	Wolverine	W7-3	G	L21_1	L	-7	-0.1	185.7	L+V	0.2	0.89
I	H_2O-NaCl	Wolverine	W7-3	G	L21_2	S	-7	-0.2	180.3	L+V	0.4	0.89
I	H_2O-NaCl	Wolverine	W7-3	G	L21_3	S	-9	-0.5	175.1	L+V	0.9	0.90
I	H_2O-NaCl	Wolverine	W7-3	G	W23	S	-7	-0.1	205.5	L+V	0.2	0.86
I	H_2O-NaCl	Wolverine	W7-3	G	W24	S	-7	-0.1	190.7	L+V	0.2	0.88
I	H_2O-NaCl	Wolverine	W7-3	G	L1_2	L	-8	-0.2	220	L+V	0.4	0.84
I	H_2O-NaCl	Wolverine	W7-3	G	M1	S	-8	-0.3	167.6	L+V	0.5	0.91
I	H_2O-NaCl	Wolverine	W7-3	H	S5	S	-11.5	-1.3	228.7	L+V	2.2	0.85
I	H_2O-NaCl	Wolverine	W7-3	H	N4	S	-9.5	-0.8	178.1	L+V	1.4	0.90
I	H_2O-NaCl	Wolverine	W7-3	H	N9_1	S	-9.5	-0.5	220	L+V	0.9	0.85
I	H_2O-NaCl	Wolverine	W7-3	H	N9_2	S	-9.5	-0.5	255.5	L+V	0.9	0.79
I	H_2O-NaCl	Wolverine	W7-3	H	O10	L	-11.5	-1.5	250.5	L+V	2.6	0.82
I	H_2O-NaCl	Wolverine	W7-3	H	L10_1	S	-6	-0.4	152.2	L+V	0.7	0.92
I	H_2O-NaCl	Wolverine	W7-3	H	L10_2	S	-12.2	-1.5	148.9	L+V	2.6	0.94
I	H_2O-NaCl	Wolverine	W7-3	H	M9	S	-9.5	-0.2	138	L+V	0.4	0.94
I	H_2O-NaCl	Wolverine	W7-3	H	N8	S	-10	-1.1	225.1	L+V	1.9	0.85
I	H_2O-NaCl	Wolverine	W7-3	H	M8_1	S	-10.1	-2.1	226.6	L+V	3.5	0.86
I	H_2O-NaCl	Wolverine	W7-3	H	N10_1	S	-10.1	-2.1	254.3	L+V	3.5	0.82
I	H_2O-NaCl	Wolverine	W7-3	H	N10_2	S	-10.1	-2.3	249.1	L+V	3.9	0.83
I	H_2O-NaCl	Wolverine	W7-3	H	I19_1	S	-9	-0.8	193.7	L+V	1.4	0.88
I	H_2O-NaCl	Wolverine	W7-3	H	I19_2	S	-15.6	-3.1	195.5	L+V	5.1	0.91
I	H_2O-NaCl	Wolverine	W7-3	H	H19	S	-15.6	-3.5	147.7	L+V	5.7	0.96
I	H_2O-NaCl	Wolverine	W7-3	H	I13_1	S	-5	-0.3	140.9	L+V	0.5	0.93
I	H_2O-NaCl	Wolverine	W7-3	H	I13_2	S	-5.5	-0.2	155.5	L+V	0.4	0.92
I	H_2O-NaCl	Wolverine	W7-3	H	K7	S	-5.5	-0.4	162.6	L+V	0.7	0.91
I	H_2O-NaCl	Wolverine	W7-3	H	L5	L	-14.4	-3.7	245.1	L+V	6.0	0.86
I	H_2O-NaCl	Wolverine	W7-3	H	L6	S	-8	-0.5	237	L+V	0.9	0.82
I	H_2O-NaCl	Wolverine	W7-3	H	K4_1	S	-16.7	-4.5	200.5	L+V	7.2	0.92
I	H_2O-NaCl	Wolverine	W7-3	H	K4_2	S	-7	-0.5	235.1	L+V	0.9	0.82
I	H_2O-NaCl	Wolverine	W7-3	H	K4_3	S	-7	-0.8	220	L+V	1.4	0.85
I	H_2O-NaCl	Wolverine	W7-3	H	K4_4	S	-7	-0.4	136.8	L+V	0.7	0.94
I	H_2O-NaCl	Wolverine	W7-3	H	J6_2	S	-15.5	-2.9	149.3	L+V	4.8	0.95
I	H_2O-NaCl	Wolverine	W7-3	H	I6_1	S	-14.3	-1.8	121.9	L+V	3.1	0.97
I	H_2O-NaCl	Wolverine	W7-3	H	I6_2	S	-14.4	-2.5	215.2	L+V	4.2	0.88
I	H_2O-NaCl	Wolverine	W7-3	H	I7	S	-13	-3.5	250.5	L+V	5.7	0.85
I	H_2O-NaCl	Wolverine	W7-3	H	G8	S	-6	-0.1	211.3	L+V	0.2	0.85
I	H_2O-NaCl	Wolverine	W7-3	H	G9	S	-16.6	-3.1	215.5	L+V	5.1	0.89
I	H_2O-NaCl	Wolverine	W7-3	H	J14_1	S	-9	-1.1	220.2	L+V	1.9	0.85
I	H_2O-NaCl	Wolverine	W7-3	H	J14_2	L	-9	-1.2	245.5	L+V+S	2.1	0.82
I	H_2O-NaCl	Wolverine	W7-3	H	H25	L	-9	-0.1	228.8	L+V	0.2	0.83
I	H_2O-NaCl	Wolverine	W7-3	H	K9_1	L	-8	-0.5	158.9	L+V	0.9	0.92
I	H_2O-NaCl	Wolverine	W7-3	H	K9_2	L	-15	-4.1	245.7	L+V	6.6	0.86
II	H_2O-NaCl	Wolverine	W7-3	D	J19	S	-13	-8.8	200	L+V	12.6	0.96
III	H_2O-$CaCl_2$-NaCl	Wolverine	W7-3	A	P22	L	-26.6	-2.1	210	L+V	3.9	0.88
III	H_2O-$CaCl_2$-NaCl	Wolverine	W7-3	A	P25	L	-30.1	-7.5	198	L+V	11.5	0.95
III	H_2O-$CaCl_2$-NaCl	Wolverine	W7-3	A	Z24	S	-35.5	-6.1	171.9	L+V	10	0.97
III	H_2O-$CaCl_2$-NaCl	Wolverine	W7-3	A	V45	S	-39.5	-15.1	160.7	L+V	18	1.05
III	H_2O-$CaCl_2$-NaCl	Wolverine	W7-3	A	V54	L	-33.3	-6.3	198.8	L+V	10.2	0.94
III	H_2O-$CaCl_2$-NaCl	Wolverine	W7-3	A	U51_3	S	-29.7	-3.5	132.5	L+V	6.3	0.97
III	H_2O-$CaCl_2$-NaCl	Wolverine	W7-3	B	V11	S	-48.7	-21.4	116.7	L+V	21.4	1.12
III	H_2O-$CaCl_2$-NaCl	Wolverine	W7-3	B	M19	S	-38.8	-19.4	174.5	L+V	20.5	1.06

(Continued)

Type	Composition	Deposit	Sample	Grain	FI No.	Bubble size	T_{mi}	T_m	T_h	Phases	Salinity	ρ (g/cm^3)
III	H_2O-$CaCl_2$-NaCl	Wolverine	W7-3	D	H23_1	S	-33.3	-12.5	151.4	L+V	16.2	1.04
III	H_2O-$CaCl_2$-NaCl	Wolverine	W7-3	D	F21_1	S	-37.2	-10.9	184.4	L+V	14.9	1.00
III	H_2O-$CaCl_2$-NaCl	Wolverine	W7-3	E	M8	S	-31.1	-10.1	211.1	L+V	14.2	0.96
III	H_2O-$CaCl_2$-NaCl	Wolverine	W7-3	F	P25	S	-29.5	-8.9	191.3	L+V	13	0.97
III	H_2O-$CaCl_2$-NaCl	Wolverine	W7-3	F	L24	S	-48.8	-20.8	148.3	L+V	21.1	1.09
III	H_2O-$CaCl_2$-NaCl	Wolverine	W7-3	G	M20_1	S	-25.3	-2.2	170.7	L+V	4	0.93
III	H_2O-$CaCl_2$-NaCl	Wolverine	W7-3	G	M20_2	S	-27.6	-2.2	168.8	L+V	4.2	0.93

III	H_2O-$CaCl_2$-NaCl	Wolverine	W7-3	G	M20_3	S	-26.6	-2.2	165	L+V	4.1	0.93
III	H_2O-$CaCl_2$-NaCl	Wolverine	W7-3	G	L1_1	L	-23.3	-1.1	193.3	L+V+S	1.9	0.89
III	H_2O-$CaCl_2$-NaCl	Wolverine	W7-3	H	M8_2	S	-29.9	-4.5	218.6	L+V	7.8	0.90
III	H_2O-$CaCl_2$-NaCl	Wolverine	W7-3	H	L12	S	-28.5	-1.9	207.7	L+V	3.7	0.88
III	H_2O-$CaCl_2$-NaCl	Wolverine	W7-3	H	I19_3	L	-30	-2.9	225.5	L+V	5.4	0.87
III	H_2O-$CaCl_2$-NaCl	Wolverine	W7-3	H	L15	S	-47.6	-19.1	168.8	L+V	20.2	1.06
III	H_2O-$CaCl_2$-NaCl	Wolverine	W7-3	H	I11	S	-40	-15.7	157.7	L+V	18.3	1.05
III	H_2O-$CaCl_2$-NaCl	Wolverine	W7-3	H	I10_1	S	-41.1	-14.1	165.1	L+V	17.3	1.04
III	H_2O-$CaCl_2$-NaCl	Wolverine	W7-3	H	I10_2	S	-38.3	-13.7	170.7	L+V	17	1.03

Notes: Type I: Low salinity H_2O-NaCl; Type II: medium salinity H_2O-NaCl; Type III: High salinity H_2O-$CaCl_2$-NaCl. "FI No." column provides coordinates of the measured fluid inclusions documented in Appendix A.

Figure captions

Fig. 1: (A) Distribution of the HREE mineralisation in the NAHREY mineral field; (B) simplified geological map of the Tanami Region; (C) Simplified geological map of the Browns Range area; (D) Major rock units in the Tanami Region; (E) Sample locality and local geology along the structure that hosts the Wolverine orebody.

Fig. 2: Field photos from Wolverine; (A) Breccia outcrop along the structure; (B) Orebody outcrop; (C) Multiple generations of quartz (milky-coloured and ore-bearing transparent). Qtz = quartz; Xnt = xenotime.

Fig. 3: Mineral assemblage associated with the HREE mineralisation and metasedimentary rocks. (A) Pre-ore coarse-grained muscovite (CG Mus) and a syn-ore assembly of fine-grained muscovite (FG Mus) and xenotime (Xnt); (B) Hydrothermal quartz (Qtz) + xenotime vein with coarse-grained (1 mm) xenotime; (C) Dissemination of xenotime and atoll-like florencite (Flr) in a hydrothermal quartz vein.

Fig. 4: Photographs of the hydrothermal quartz samples selected for fluid inclusion studies. (A) Mineralised sample A2-14 from Area 5 deposit; (B) Mineralised sample W7-3 from Wolverine deposit; (C) Barren sample W8 from Wolverine deposit; (D) Cathodoluminescence image of a mineralised quartz vein showing oscillatory zoned quartz with ore minerals distributed throughout; (E) Assembly of primary fluid inclusions from sample W7-3; (F) Distribution of individual isolated fluid inclusions from sample A2-14; (G) Distribution of primary fluid inclusions from sample W8. Note that the fluid inclusions are at different depths. Qtz = quartz; Xnt = xenotime; Flr = florencite.

Fig. 5: Representative laser Raman spectra of fluid inclusions. (A) Spectrum for liquid phase of type I fluid inclusion (low-salinity H_2O-NaCl); (B) Spectrum for vapour phase of type I fluid inclusion; (C) Spectrum for liquid phase of type III fluid inclusion (low- to high-salinity H_2O-$CaCl_2$-NaCl); (D) Spectrum for vapour phase of type III fluid inclusion; (E) Spectrum for solid (florencite) phase of type III fluid inclusion; (F) Spectrum for ore-related florencite. Note that the solid phase in the type III fluid inclusion and florencite ore have comparable vibrational regions.

Fig. 6: Histogram of the final ice melting temperatures (T_m) of the fluid inclusion types in the mineralised and barren samples.

Fig. 7: Histogram of the homogenization temperatures (T_h) of the fluid inclusion types in the mineralised and barren samples.

Fig. 8: (A) T_m-T_{mi} and (B) T_m-T_h relationships of the three fluid inclusion types in the mineralised and barren samples.

Fig. 9: Composition (in wt.%) of the three fluid inclusion types in the ternary H_2O-$CaCl_2$-NaCl diagram (after Hurai et al., 2015). Note that the NaCl/(NaCl+$CaCl_2$) mass fraction could not be determined for low- and medium-salinity type III fluid inclusions. The maximum NaCl/(NaCl+$CaCl_2$) mass fraction for the high salinity type III fluid inclusions can be determined from the intersection of the −25 °C ice-melting isotherm with the hydrohalite liquidus.

Fig. 10: Na versus K (in wt.%) plot for the three types of fluid inclusions.

Fig. 11: Oxygen isotope composition of the ore-related and barren quartz separates and the metasedimentary/sedimentary rocks of the BRM and the Birrindudu Group sandstones. Note that the ore-related quartz separates are characterised by $\delta^{18}O_{fluid}$ largely in the range defined by the BRM and the Birrindudu Group sandstones. The $\delta^{18}O_{fluid}$ bars include 2σ uncertainties. Qtz = quartz; BG = Birrindudu Group; BRM = Browns Range Metamorphics; WV = Wolverine.

Table 1: Location details and fluid inclusion types within the studied samples from the Browns Range

Sample	Drillhole	Deposit	Easting	Northing	Depth	FIs Type	Ore
W8	-	Wolverine	494124	7914636	Surface	I	Barren
A2-14	BRAD0002	Area 5	492231	7909976	135m	I, II, III	Mineralise
W7-3	BRWD0007	Wolverine	493695	7914741	41m	I, II, III	Mineralise

Coordinate system: UTM zone 52S.

Table 2: Microthermometric data, salinity and density of the fluid inclusion types from the Browns Range

Type	Composition	Host	Phase	T_{mi} (°C)	T_m (°C)	T_h (°C)	Salinity (wt.% NaCl)	Density (g/cm^3)
Mineralised								
Type I	H_2O-NaCl	Quartz	L-V±S	-4.4 – -19	-0.1 – -6.5	99 – 272	0.2 – 9.9	0.76 – 1.0
Type II	H_2O-NaCl	Quartz	L-V	-13 – -21	-8.8 – -14.4	156 – 222	12.6 – 18.1	0.94 – 1.0
Type III	H_2O-$CaCl_2$-NaCl	Quartz	L-V±S	-22.9 – -51.3	-0.5 – -25.8	103 – 241	0.5 – 25.8	0.87 – 1.1
Barren								
Type I	H_2O-NaCl	Quartz	L-V	-4.4 – -19	-0.1 – -6.5	170 – 350	0.2 – 8.5	0.63 – 0.94

Note: Due to the lack of a next-to-last solid phase, accurate calculation of the salinity of the type III fluid inclusions was not possible. Instead, T_m was used to approximate the salinity.

Table 3: Elemental composition of the primary fluid inclusions

Samples	Type	FI No	T_m	T_h	Na	P	Cl	K	Ca	Fe	Y	Ce	U	Na/K (mass)
A2-14 (ore-related)	I	E_K13	-1.2	250	0.79	<0.7	<6.5	0.1	<3.0	<0.20	<1.6	<1.8	<1.1	5.6
W8 (Barren)	I	C_N10	-1.5	187.7	0.79	<0.8	<8.0	0.1	<3.5	<0.20	<1.6	<1.8	<1.1	5.4
A2-14 (ore-related)	I	B_Y13	-2.8	250	1.97	<0.2	<1.6	0.3	<0.7	<0.04	<0.4	<0.4	<0.3	5.4
A2-14 (ore-related)	II	A_O29	-10.1	155.6	3.93	<6.3	<6.4	0.9	<2.8	<1.5	<21.7	<17.6	<11.0	4.4
A2-14 (ore-related)	III	B_AF19	-2.7	187.8	1.97	<3.4	<3.5	0.4	<1.5	<0.9	<11.6	<9.4	<5.9	4.9
W7-3 (ore-related)	III	A_Z24	-6.1	171.9	3.93	<0.2	5.1	0.6	<0.9	<0.05	<0.7	<0.5	<0.3	6.6
W7-3 (ore-related)	III	A_V54	-6.3	198.8	3.93	<0.4	6.4	1.0	<1.8	0.10	<1.2	<1.0	<0.6	4.1
A2-14 (ore-related)	III	G_L12-2	-6.9	241.2	4.33	<0.1	3.5	0.7	1.2	<0.03	<0.4	<0.3	<0.2	6.0
A2-14 (ore-related)	III	G_L12-2	-6.9	241.2	4.33	<0.2	3.5	0.8	0.9	0.20	<0.5	0.9	<0.3	5.1
A2-14 (ore-related)	III	G_N25	-7.2	210	4.33	<0.0	4.8	0.8	0.8	<0.03	<0.2	<0.1	0.2	5.7
W7-3 (ore-related)	III	A_P25	-7.5	198	4.33	<0.2	3.2	0.8	<0.9	0.10	1.0	<0.5	<0.3	5.1
A2-14 (ore-related)	III	C_N17	-7.6	201	4.72	<0.1	4.4	0.7	0.6	0.05	<0.3	<0.2	<0.1	6.8
A2-14 (ore-related)	III	G_K22	-9.2	185	5.11	<0.1	2.4	0.9	1.4	0.05	<0.2	0.8	<0.1	6.0
W7-3 (ore-related)	III	H_L15	-19.1	168.8	6.61	<2.1	2.1	1.4	<9.5	0.59	<5.5	<4.5	<2.8	4.6
A2-14 (ore-related)	III	G_L20-1	-24.5	174	6.45	<0.6	2.2	1.1	<2.6	<0.14	<1.9	1.7	120	5.7

Notes: Type I: Low-salinity H_2O-NaCl; Type II: Medium-salinity H_2O-NaCl; Type III: Low- to high-salinity H_2O-$CaCl_2$-NaCl. All major elements are in wt.%. Yttrium, Ce and U are in ppm.

Table 4: Oxygen isotope composition of quartz and xenotime separates and whole-rock samples of metasedimentary rocks

Location	Deposit/prospect	Sample No.	Longitude	Latitude	Drill core	Depth (m)	Type	$\delta^{18}O_{qtz}$	$\delta^{18}O_{xnt}$	$\delta^{18}O_{fluid}$	$2\sigma\ \delta^{18}O_{fluid}$
Ore-related quartz and xenotime											
Boulder Ridge	Prospect	BR1	545197	7827868	-	Outcrop	Ore-related	15.0		6.1	0.9
Dazzler	Prospect	D3	490384	7902004	-	Outcrop	Ore-related	14.8		5.9	0.9
Iceman	Prospect	I1	490746	7901660	-	Outcrop	Ore-related	14.8		5.9	0.9
Cyclops	Deposit	C2	489782	7904619	-	Outcrop	Ore-related	12.6		3.7	0.6
Wolverine	Deposit	W5-2	493508	7915069	BRWT0332W5	487.6	Ore-related	15.8		6.9	1.0
Wolverine	Deposit	W5-4	493508	7915069	BRWT0332W5	503.1	Ore-related	11.3		2.4	0.4
Wolverine	Deposit	W5-7	493508	7915069	BRWT0332W5	505.5	Ore-related	17.2	7.3	8.3	1.2
Wolverine	Deposit	W7-2	493696	7914741	BRWD0007	36.5	Ore-related	14.6	6.8	5.7	0.9

Wolverine	Deposit	W7-3	493696	7914741	BRWD0007	41.6	Ore-related	14.7	6.3	5.8	0.9
Wolverine	Deposit	W14	n.a.	n.a.	n.a.	n.a.	Ore-related	15.3	7.3	6.4	1.0
Wolverine	Deposit	W16-3	493599	7914773	BRWD0016	88.7	Ore-related	19.2		11.4	1.7
Wolverine	Deposit	W324-3	493541	7914984	BRWT0324	384.8	Ore-related	20.3		6.1	0.9
Wolverine ore hosting structure											
Wolverine	Deposit	W1	493723	7914708	-	Outcrop	Ore-related	20.2		11.3	1.7
Wolverine	Deposit	W4	493796	7914690	-	Outcrop	Ore-related	16.2		7.3	1.1
Wolverine	Deposit	W5	493850	7914682	-	Outcrop	Ore-related	15.2		6.3	0.9
Wolverine	Deposit	W9	493852	7914677	-	Outcrop	Ore-related	16.1		7.2	1.1
Wolverine	Deposit	W10	493872	7914660	-	Outcrop	Ore-related	13.9		5	0.8
Wolverine	Deposit	W13	493967	7914637	-	Outcrop	Ore-related	17.8		8.9	1.3
Wolverine	Deposit	W8	494125	7914636	-	Outcrop	Barren	10.3		5	0.7
BRM											
Wolverine	Deposit	W16-1	493599	7914773	BRWD0016	47.8	Detrital Qtz	10.7		1.8	0.3
Gambit	Deposit	G4-8	493210	7913635	BRGD0004	70.8	Detrital Qtz	12.7		3.8	0.6
Gambit	Deposit	G5-1	493098	7913652	BRGD0005	11.2	Detrital Qtz	13.3		4.4	0.7
Wolverine	Deposit	W7-1	493696	7914741	BRWD0007	22.1	Detrital Qtz	12.4		3.5	0.5
Wolverine	Deposit	W5-1	493508	7915069	BRWT0332W5	441.2	Whole-rock	12.5		3.6	0.5
Wolverine	Deposit	W5-10	493508	7915069	BRWT0332W5	529	Whole-rock	13.0		4.1	0.6
Wolverine	Deposit	W5-12	493508	7915069	BRWT0332W5	545	Whole-rock	14.1		5.2	0.8
Wolverine	Deposit	W5-13	493508	7915069	BRWT0332W5	550.7	Whole-rock	12.9		4	0.6
Wolverine	Deposit	W16-4	493599	7914773	BRWD0016	103.5	Whole-rock	12.4		3.5	0.5
Birrindudu Group sandstones											
Cyclops	Prospect	C1	489642	7904606	-	Outcrop	Whole-rock	16.9		8	1.2

Notes: The $\delta^{18}O_{fluid}$ values were calculated based on $\delta^{18}O_{qtz}$ and T_h = 250 °C using equation of Clayton et al. (1972), with the exception of sample W8 (barren sample), whose $\delta^{18}O_{fluid}$ value was measured based on T_h = 350 °C. Qtz = quartz, Xnt = xenotime, BRM = Browns Range Metamorphics. Uncertainty (2σ) is 0.15‰ of the $\delta^{18}O_{fluid}$ value calculated based on the long-term average difference in $\delta^{18}O$ values of the internal standards (see Analytical Methods).

Highlights

Hydrothermal xenotime ores in Tanami Region occur along faults and unconformities

Ore-related quartz contains low-salinity meteoric water and high-salinity fluids

Ores formed due to mixing of REE-bearing basement- and P-bearing basin-derived fluids

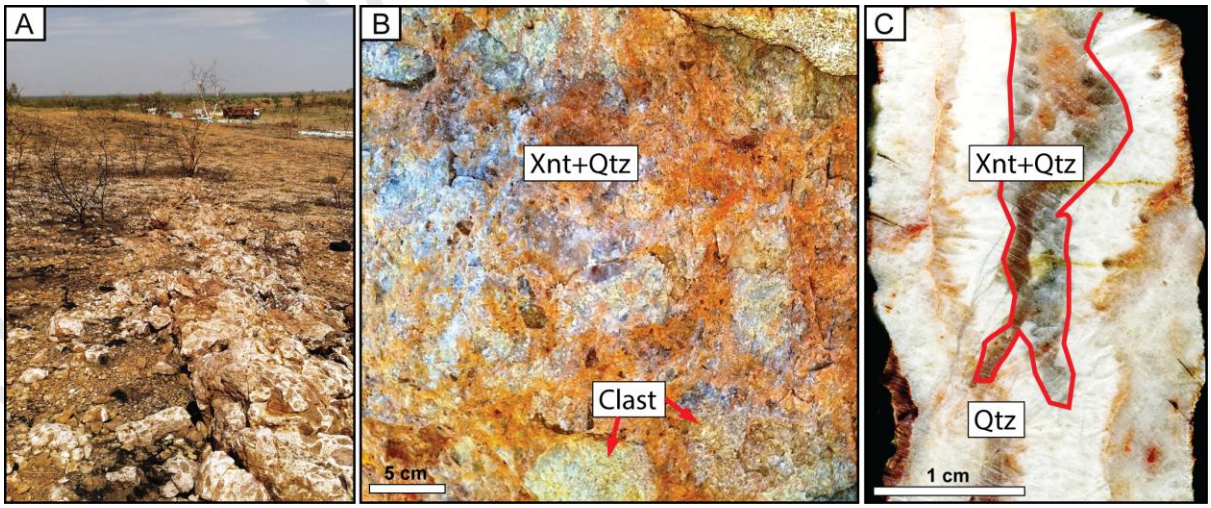

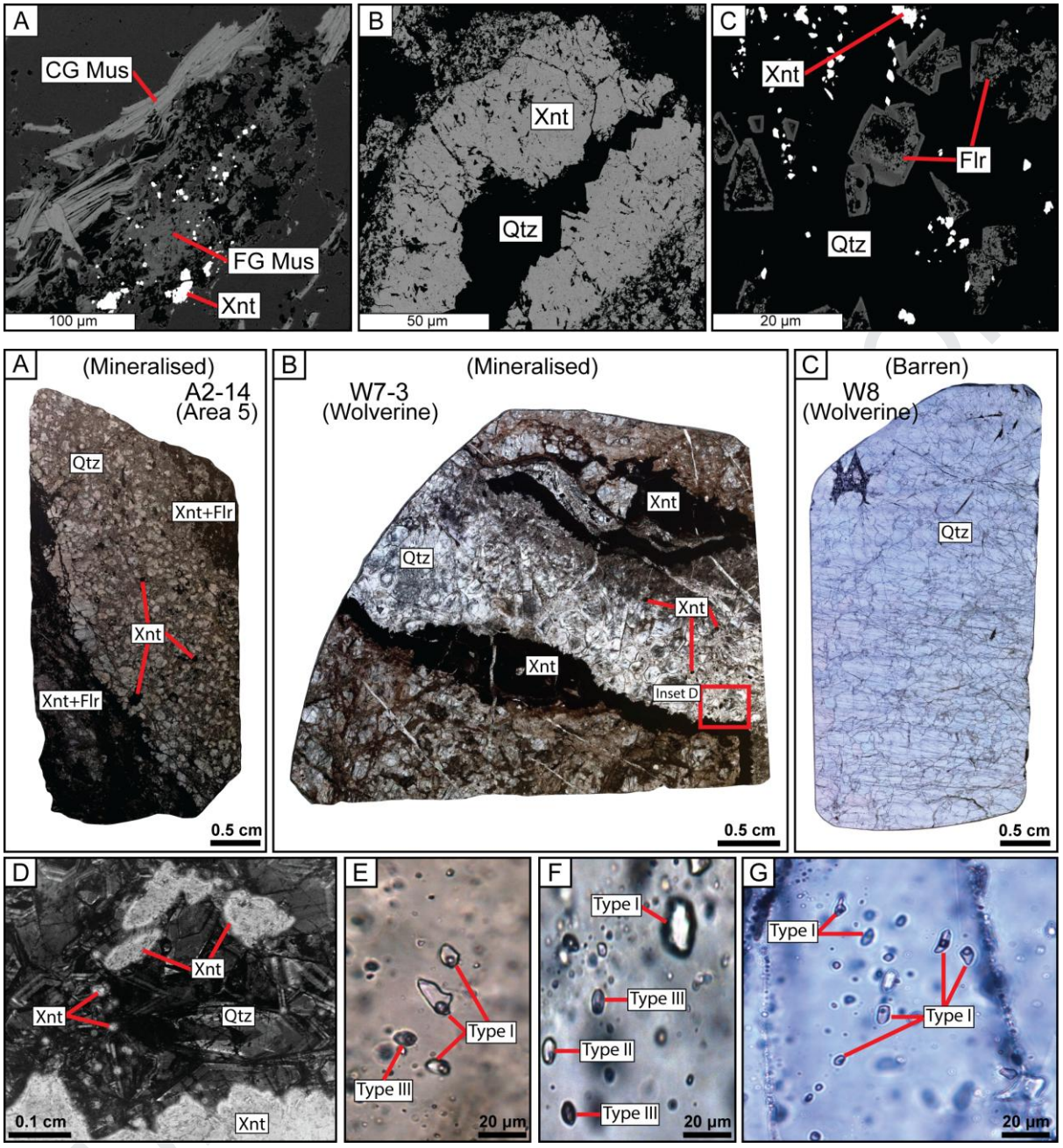
A
CG Mus
FG Mus
Xnt
100 µm
B
Xnt
Qtz
50 µm
C
Xnt
Flr
Qtz
20 µm
A
(Mineralised)
A2-14
(Area 5)
Qtz
Xnt+Flr
Xnt
Xnt+Flr
0.5 cm
B
(Mineralised)
W7-3
(Wolverine)
Xnt
Qtz
Xnt
Xnt
Inset D
0.5 cm
C
(Barren)
W8
(Wolverine)
Qtz
0.5 cm
D
Xnt
Xnt
Qtz
0.1 cm
Xnt
E
Type I
Type III
20 µm
F
Type I
Type III
Type II
Type III
20 µm
G
Type I
Type I
20 µm